Numerical Phase-Field Models On Surfaces And Applications

by
Yerbol Palzhanov

A dissertation submitted to the Department of Mathematics,

College of Natural Sciences and Mathematics

in partial fulfillment of the requirements for the degree of

Doctor of Philosophy
in Mathematics

Chair of Committee: Maxim Olshanskii

Committee Member: Annalisa Quaini

Committee Member: Alexander Mamonov

Committee Member: Sheereen Majd

University of Houston
May 2024

ACKNOWLEDGEMENTS

I would like to express my appreciation to my academic advisors, Dr. Maxim Olshanskii and Dr. Annalisa Quaini, for their continuous support and guidance.

ABSTRACT

This dissertation focuses on three research topics: (i) the study of the scalar auxiliary variable (SAV) method for the surface Cahn-Hilliard equations, (ii) the development of a numerical method for the Navier-Stokes-Cahn-Hilliard (NSCH) equations on surfaces, and (iii) applications of the NSCH model in biomembranes.

The SAV formulation of the Cahn-Hilliard equations is combined with an adaptive time stepping and a geometrically unfitted trace finite element method (TraceFEM). The stability is proven to hold in an appropriate sense for both first- and second-order in time variants of the method. The performance of our SAV method is illustrated through a series of numerical experiments, including a systematic comparison with a stabilized semi-explicit method.

A thermodynamically consistent phase-field model is introduced for a two-phase flow of incompressible viscous fluids. The model allows for a non-linear dependence of fluid density on the phase-field order parameter. Driven by applications in biomembrane studies, the model is formulated for tangential flows of fluids constrained to a surface and consists of the Navier–Stokes–Cahn–Hilliard type equations. A fully discrete time-stepping scheme with the following properties is presented: (i) the scheme decouples the fluid and phase-field equation solvers at each time step, (ii) the resulting two algebraic systems are linear, and (iii) the numerical solution satisfies the same stability bound as the solution of the original system under some restrictions on the discretization parameters. Numerical examples are provided to demonstrate the stability, accuracy, and overall efficiency of the approach.

Finally, the NSCH model is employed for the quantitative validation of domain coarsening, fluidity, and fusogenicity of multi-component vesicles.

This dissertation incorporates sections from the following articles, with the consent of collaborating authors, and adhering to publisher policies: Palzhanov, Zhiliakov, Quaini, and Olshanskii (2021) [88]; Olshanskii, Palzhanov, and Quaini (2023) [78]; Wang, Palzhanov, Quaini, Olshanskii, and Majd (2022) [111]; Wang, Palzhanov, Dang, Quaini, Olshanskii, and Majd (2023) [110].

TABLE OF CONTENTS

LIST OF TABLES

LIST OF FIGURES

1 Introduction

Phase-field modeling is a mathematical and computational approach used to study and numerically simulate the evolution of the multi-phase systems. The evolution of such systems is often characterized by abrupt phase transitions. This poses a challenge for analysis and simulations due to discontinuities or singularities in the solution to the corresponding mathematical problem. Phase-field modeling addresses this challenge by introducing a smooth and continuous order parameter that varies seamlessly across the domain. This order parameter enables the representation of different phases without the development of sharp interfaces. The convenience offered by having smooth order parameter, in addition to the possibility of rigorous mathematical analysis, has made phase-field methods highly successful in modeling multi-phase problems. The evolution of the phase-field variables is usually driven by the gradient flow of a total free energy functional. However, constructing efficient, robust, and energy-stable numerical schemes for gradient flow problems is not a trivial task. If one is not careful in designing a numerical scheme that preserves the energy dissipation mechanism inherent in gradient flows, an extremely small time step might be required to dissipate energy, resulting in an inefficient scheme. For a comprehensive review of numerical schemes for gradient flows, we refer to [96]. One effective numerical technique for a broad range of gradient flows is the scalar auxiliary variable (SAV) method [95], which enables the construction of efficient and accurate time discretization schemes. Since its introduction in [95], the SAV method has been developed and applied to various problems, including epitaxial thin film growth models [19], models for single- and multi-component Bose-Einstein condensates [120], and the square phase field crystal model [108].

SAV methods for the Cahn–Hilliard equation have been extensively studied in volumetric domains. Convergence and error analysis for a first-order semi-discrete SAV scheme are conducted in [94]. An unconditionally energy-stable and second-order accurate SAV algorithm is presented in [17]. Error estimates for first and second-order fully discretized SAV schemes, utilizing a mixed finite element discretization for the spatial variables, are derived in [18]. An improvement over the

standard SAV method is represented by a class of extrapolated and linearized SAV methods based on Runge–Kutta time integration [5]. These methods can achieve arbitrarily high-order accuracy for the time discretization of the Cahn–Hilliard problem. To the best of our knowledge, it is the first time that the SAV method is applied to the *surface* Cahn–Hilliard problem. Other surface problems are treated in [102, 103].

In early versions of the SAV method [95, 96], numerical efficiency for the Cahn–Hilliard equations is achieved through the computationally cheap invertibility of the discrete biharmonic operator in simple geometric settings discretized by, e.g., a tensor product finite difference method. For the equations posed on surfaces, such fast solvers are not available in general.

In this work, for the first time, SAV methods are combined with a geometrically *unfitted* finite element method for the numerical solution of the Cahn-Hilliard problem posed on a surface. The approach builds on earlier work on a unfitted FEM for elliptic PDEs posed on surfaces [84] called TraceFEM. Unlike some other geometrically unfitted methods for surface PDEs, TraceFEM employs sharp surface representation. The surface can be defined implicitly and no knowledge of the surface parametrization is required. This method allows to solve for a scalar quantity or a vector field on a surface, for which a parametrization or triangulation is not required. In [102, 103] instead, the authors have opted for a fitted finite element method, combined with a exponential-type SAV scheme. We consider both first-order and second-order backward differentiation formula schemes and prove their energy stability. Additionally, we present a time-adaptive version of the second-order scheme, drawing inspiration from [33]. Implementation details are provided for all the proposed schemes.

Furthermore, we investigate the coupling of the Cahn-Hilliard equations with the Navier-Stokes equations. The classical diffuse-interface description of a binary incompressible fluid with density-matched components is known as *Model H* [47], constituting the Navier–Stokes–Cahn–Hilliard (NSCH) system. Several generalizations to the case of variable density components have been presented in the literature [2, 4, 11, 21, 22, 34, 35, 73, 98]. It is important to note that some

of these models relax the incompressibility constraint to quasi-compressibility, and not all models satisfy Galilean invariance, local mass conservation, or thermodynamic consistency. In this work, we specifically focus on the generalization of Model H, initially presented in [2]. This model demonstrates thermodynamic consistency when the density of the mixture depends linearly on the phase-field variable (concentration or volume/surface fraction). We introduce an extension of the model presented in [2], ensuring thermodynamic consistency for a general monotone relation between density and the phase-field variable.

Motivated by applications in biomembranes, we apply this new model to simulate the dynamics of two-phase flows on closed smooth surfaces of arbitrary shapes. While computational studies extensively explore multi-component fluid flows in planar and volumetric domains (see, e.g., [40, 71, 77, 114, 118] and references therein), the research of the NSCH systems on manifolds is somewhat limited. This lack of studies arises due to the inherent challenges in numerically solving equations on general surfaces, involving the discretization of tangential differential operators and the approximate recovery of potentially complex shapes. In [76], the authors tackle these challenges by introducing a stream function formulation, decoupling the surface Navier–Stokes problem from the surface Cahn-Hilliard problem, and employing a parametric finite element approach. Using an alternative approach, Yang and Kim [113] experimented with a finite difference method on staggered marker-and-cell meshes for the NSCH system posed on surface embedded in the mesh.

We continue studying the TraceFEM for the simulation of two-phase incompressible flow on surfaces using our generalization of Model H. TraceFEM has been extended to the surface Stokes problem in [79, 81] and the surface Cahn–Hilliard problem in [115]. Additionally, ongoing work is being conducted on TraceFEM for equations on evolving surfaces [85, 80].

While the numerical analysis of diffuse-interface models for two-phase fluids with *matching densities* can rely significantly on established analyses for the incompressible Navier–Stokes equations and the Cahn–Hilliard equations alone [29, 56, 43], designing energy-stable, efficient, and consistent discretizations for diffuse-interface models involving *non-matching densities* turns out to be more challenging.

The present study contributes to the field with a first order in time, linear, and decoupled FE scheme for our generalization of the model from [2]. One advantage of the proposed scheme is that it neither modifies the momentum equation nor alters the advection velocity. We prove that the scheme is stable under a mild time-step restriction. Moreover, the analysis tracks the dependence of the estimates on ϵ, the critical model parameter that defines the width of the transition region between phases. The fact that the model is posed on arbitrary-shaped closed smooth surfaces and the use of an unfitted finite element method for spatial discretization add some further technical difficulties to the analysis. However, apart from these extra technical details, the general line of arguments can be simplified to a Euclidian setting or extended to other spatial discretization techniques.

Finally, we explore some applications of the proposed NSCH model in multicomponent lipid vesicles. Biological membranes exhibit heterogeneity, a crucial aspect influencing their functionality. The phenomenon of domain formation in membranes has been leveraged to create innovative materials with diverse surfaces. When applied to drug delivery, these heterogeneous membrane materials have demonstrated distinct advantages over their homogeneous counterparts [8, 91]. However, the efficient design of such heterogeneous membrane-based materials necessitates computer-aided modeling capable of predicting lipid domain formation and dynamics on a given membrane composition reliably and quantitatively. To enhance the accuracy of predictions, considering membrane viscosity differences between liquid ordered and disordered phases, we employ the Navier–Stokes–Cahn–Hilliard model coupled with innovative numerical methods. To validate the model, we compare its numerical results with experimental results on Giant Unilamellar Vesicles (GUVs) featuring ternary membrane compositions. Also, we study the fusogenicity of cationic liposomes in relation to their surface distribution of cationic lipids and utilizes membrane phase separation to control this surface distribution. It is found that concentrating the cationic lipids into small surface patches on liposomes, through phase-separation, can enhance liposome's fusogenicity. Further concentrating these lipids into smaller patches on the surface of liposomes led to an increased level of fusogenicity. These experimental findings are supported by numerical simulations

using the NSCH model.

The rest of the dissertation is organized as follows:

Chapter 2. We give some necessary basics of tangential calculus on smooth surfaces embedded in $\mathbb{R}^3$.

Chapter 3. We introduce our phase field models on surfaces: the Cahn-Hilliard model and the Navier-Stokes-Cahn-Hilliard model. Details of these models, along with their energy dissipation properties, are presented, as shown in [88, 115].

Chapter 4. We develop a numerical method using a scalar auxiliary variable for the Cahn-Hilliard equations and prove its numerical stability. Also, we examine the time adaptive algorithm for this method. Concerning the NSCH model, we describe a decoupled finite element method and provide its analysis [88, 78].

Chapter 5. We present a numerical assessment of the numerical methods and models developed in the thesis. For the CH model, we report results on convergence, phase separation simulation, and engage in a discussion on time adaptivity. Reports on the NSCH model include convergence test and simulations of the Kelvin–Helmholtz and Rayleigh–Taylor instabilities [88, 78].

Chapter 6. The developed models and methods are applied to simulate phase separation and domain formation in multicomponent lipid bi-layers. We compare the numerical results to experimental findings on giant unilamellar vesicles (GUV) obtained through fluorescence microscopy imaging. Additionally, we employ our model to investigate the electrostatic interaction between small unilamellar vesicles (SUV) and GUVs [111, 110].

Chapter 7. In conclusion, we offer some final remarks on the introduced phase-field models on surfaces, reflecting on their significance, potential applications, and avenues for future research.

2 Tangential calculus on manifolds

In this chapter we introduce some basics of tangential calculus for manifolds. Consider $\Gamma \subset \mathbb{R}^n, n \geqslant 3$, a $(n-1)$-dimensional closed, smooth, simply connected manifold. Our main interest is the case $n = 3$, that is why we will proceed with this case, but most of the concepts and the analysis applies for general n. Concerning the smoothness conditions for Γ, we note that it will sufficient to assume that the surface Γ has C^3 smoothness. In the remainder, we always assume that this holds. For a more in-depth exploration of this topic, see [51].

2.1 The tangential operators

The outward pointing normal vector on Γ is denoted by $\mathbf{n} = \mathbf{n}(\mathbf{x}, t)$, and

$$\mathbf{P} = \mathbf{P}(\mathbf{x}) \coloneqq \mathbf{I} - \mathbf{n}(\mathbf{x})\mathbf{n}(\mathbf{x})^T$$

for $\mathbf{x} \in \Gamma$ is the orthogonal projection onto the tangent plane.

In a neighborhood $\mathcal{O}(\Gamma)$ of Γ, the closest point projection $\mathbf{p} : \mathcal{O}(\Gamma) \to \Gamma$ is well defined. For a scalar function $p : \Gamma \to \mathbb{R}$ or a vector function $\mathbf{u} : \Gamma \to \mathbb{R}^3$, we define $p^e = p \circ \mathbf{p} : \mathcal{O}(\Gamma) \to \mathbb{R}$, $\mathbf{u}^e = \mathbf{u} \circ \mathbf{p} : \mathcal{O}(\Gamma) \to \mathbb{R}^3$, extensions of p and $\mathbf{u}$ from Γ to its neighborhood $\mathcal{O}(\Gamma)$ along the normal directions. On Γ, it holds $\nabla p^e = \mathbf{P}\nabla p^e$ and $\nabla \mathbf{u}^e = \nabla \mathbf{u}^e \mathbf{P}$, with $\nabla \mathbf{u} := (\nabla u_1 \ \nabla u_2 \ \nabla u_3)^T \in \mathbb{R}^{3\times 3}$ for vector functions $\mathbf{u}$. The surface gradient and covariant derivatives on Γ are then defined as $\nabla_\Gamma p = \mathbf{P}\nabla p^e$ and $\nabla_\Gamma \mathbf{u} := \mathbf{P}\nabla \mathbf{u}^e \mathbf{P}$. Note that the definitions of surface gradient and covariant derivatives are independent of a particular smooth extension of p and $\mathbf{u}$ off Γ. The reason why we consider normal extensions is because they are convenient for the error analysis.

For scalar functions f, g and vector functions $\mathbf{u}, \mathbf{v} : \Gamma \to \mathbb{R}^n$ we have the following product rules:

$$\nabla_\Gamma(fg) = g\nabla_\Gamma f + f\nabla_\Gamma g \tag{2.1}$$

$$\nabla_\Gamma(\mathbf{u}\cdot\mathbf{v}) = \mathbf{v}^T\nabla_\Gamma\mathbf{u} + \mathbf{u}^T\nabla_\Gamma\mathbf{v}, \quad \text{if } \mathbf{P}\mathbf{u} = \mathbf{u},\ \mathbf{P}\mathbf{v} = \mathbf{v}, \tag{2.2}$$

$$\nabla_\Gamma(f\mathbf{u}) = f\nabla_\Gamma\mathbf{u} + \mathbf{P}\mathbf{u}\nabla_\Gamma f. \tag{2.3}$$

The surface divergence operators for a vector $\mathbf{g} : \Gamma \to \mathbb{R}^3$ and a tensor $\mathbf{A} : \Gamma \to \mathbb{R}^{3\times 3}$ are defined as:

$$\mathrm{div}_\Gamma\mathbf{v} := \mathrm{tr}(\nabla_\Gamma\mathbf{v}) = \mathrm{tr}(\mathbf{P}(\nabla\mathbf{v})\mathbf{P}) = \mathrm{tr}(\mathbf{P}(\nabla\mathbf{v}))) = \mathrm{tr}((\nabla\mathbf{v})\mathbf{P}), \tag{2.4}$$

$$\mathrm{div}_\Gamma\mathbf{A} := \left(\mathrm{div}_\Gamma(\mathbf{e}_1^T\mathbf{A}),\ \mathrm{div}_\Gamma(\mathbf{e}_2^T\mathbf{A}),\ \mathrm{div}_\Gamma(\mathbf{e}_3^T\mathbf{A})\right)^T. \tag{2.5}$$

with $\mathbf{e}_i$ the ith standard basis vector in $\mathbb{R}^3$.

For a closed smooth surface Γ, the integration by parts identity needed to devise weak formulations reads:

$$\int_\Gamma v\mathrm{div}_\Gamma\mathbf{f}\,ds = -\int_\Gamma \mathbf{f}\cdot\nabla_\Gamma v\,ds + \int_\Gamma \kappa v\mathbf{f}\cdot\mathbf{n}\,ds, \quad \text{for } \mathbf{f}\in H^1(\Gamma)^3,\ v\in H^1(\Gamma), \tag{2.6}$$

here κ is the sum of principle curvatures; see, e.g. [38, Appendix A].

3 Mathematical models

3.1 The Cahn–Hilliard model posed on surfaces

On Γ we consider a heterogeneous mixture of two species with mass concentrations $c_i = m_i/m$, $i = 1, 2$, where m_i are the masses of the components and m is the total mass. Since $m = m_1 + m_2$, we have $c_1 + c_2 = 1$. Let c_1 be the representative concentration c, i.e., $c = c_1$. Concentration $c \in [0, 1]$ is a conserved quantity, moreover let ρ be the constant total density of the system $\rho = m/S$, where S is the surface area of Γ. Phase separation in this two component system can be modelled by the Cahn–Hilliard equation [16, 15].

In order to describe the evolution of the concentration profile $c(\mathbf{x}, t)$, we consider the conservation law:

$$\rho \frac{\partial c}{\partial t} + \operatorname{div}_\Gamma \mathbf{j} = 0 \quad \text{on } \Gamma \times (0, T], \tag{3.1}$$

where ρ is the density of the system and $\mathbf{j}$ is a diffusion flux. The flux $\mathbf{j}$ is defined according to Fick's law, which is empirical:

$$\mathbf{j} = -M \nabla_\Gamma \mu \quad \text{on } \Gamma, \quad \mu = \frac{\delta f}{\delta c}, \tag{3.2}$$

where M is the so-called mobility coefficient (see [60]) and μ is the chemical potential, which is defined as the functional derivative of the total specific free energy f with respect to the concentration c. Thus, we introduce the total specific free energy:

$$f(c) = f_0(c) + \frac{1}{2}\epsilon^2 |\nabla_\Gamma c|^2. \tag{3.3}$$

where $f_0(c)$ is the free energy per unit surface, while the second term in (3.3) represents the interfacial free energy based on the concentration gradient. We recall that in order to have phase

separation, f_0 must be a non-convex function of c. A fundamental fact of the chemical thermodynamics is that even when phase separation has occurred, there is a limited miscibility between the components. In model (3.1)–(3.3), the interface between the two components is a layer of size ϵ where thermodynamically unstable mixtures are stabilized by a gradient term in the energy. Further details concerning the thermodynamics of partially miscible mixtures can be found, for example, in [60].

By combining eq. (3.1), (3.2), and (3.3), we obtain the surface Cahn–Hilliard equation:

$$\rho\frac{\partial c}{\partial t} - \operatorname{div}_\Gamma\left(M\nabla_\Gamma\left(f_0' - \epsilon^2\Delta_\Gamma c\right)\right) = 0 \quad \text{on } \Gamma. \tag{3.4}$$

Eq. (3.4) is a fourth-order equation, so casting it in a weak form would result in the presence of second-order spatial derivatives. From the numerical point of view, it is beneficial to avoid higher order spatial derivatives. Hence, it is common to rewrite eq. (3.4) in mixed form, i.e., as two coupled second-order equations:

$$\rho\frac{\partial c}{\partial t} - \operatorname{div}_\Gamma\left(M\nabla_\Gamma\mu\right) = 0 \quad \text{on } \Gamma, \tag{3.5}$$

$$\mu = f_0' - \epsilon^2\Delta_\Gamma c \quad \text{on } \Gamma. \tag{3.6}$$

System (3.5)–(3.6) needs to be supplemented with the definitions of mobility M and free energy per unit surface f_0. A possible choice for M is given by

$$M = M(c) = c(1-c). \tag{3.7}$$

This mobility is referred to as a degenerate mobility, since it is not strictly positive. We note that in many of the existing analytic studies, as well as numerical simulations, mobility is assumed to be constant. At the same time, concentration dependent mobility was already considered by Cahn [15] and (3.7) is also a popular choice for numerical studies. Although it is known that the dependence between the mobility on the concentration difference produces important changes

during the coarsening process, only a few authors consider more complex mobility functions; see, e.g., [119]. In the absence of studies on the appropriate mobility function for lateral phase separation in biological membranes, here we choose to use (3.7). Again, a common choice for f_0 is given by

$$f_0(c) = \frac{\xi}{4} c^2 (1-c)^2, \tag{3.8}$$

where ξ defines the barrier height, i.e., the local maximum at $c = 1/2$ [27]. We set $\xi = 1$ in all of our simulations. With mobility as in (3.7) and specific free energy as in (3.8), problem (3.5)–(3.6) is a coupled system of nonlinear PDEs posed on Γ.

The Cahn–Hilliard equations define gradient flows of the energy functional $E(u) = \int_\Gamma f(u)\, ds$ in $H^{-1}(\Gamma)$ (a dual space to $H^1(\Gamma)$). More precisely, the following energy minimization property holds:

$$\frac{d}{dt} E(c) = -\int_\Gamma |M(c) \nabla_\Gamma (\epsilon^2 \Delta_\Gamma c + f'(c))|^2 \, ds < 0. \tag{3.9}$$

3.2 The Navier–Stokes–Cahn–Hilliard model posed on surfaces

For Navier-Stokes-Cahn-Hilliard model, the definition of c is modified as follows: On an arbitrary-shaped closed, smooth, and stationary surface Γ we consider a heterogeneous mixture of two species with surface fractions $c_i = S_i/S$, $i = 1, 2$, where S_i are the surface area occupied by the components and S is the surface area of Γ. Since $S = S_1 + S_2$, we have $c_1 + c_2 = 1$. Let c_1 be the representative surface fraction, i.e., $c = c_1$. Moreover, let m_i be the mass of component i and m is the total mass. Notice that density of the mixture can be expressed as $\rho = \frac{m}{S} = \frac{m_1}{S_1}\frac{S_1}{S} + \frac{m_2}{S_2}\frac{S_2}{S}$. Thus,

$$\rho = \rho(c) = \rho_1 c + \rho_2 (1-c), \tag{3.10}$$

where densities $\rho_1, \rho_2 > 0$ are given constants. Similarly, for the dynamic viscosity of the mixture we can write

$$\eta = \eta(c) = \eta_1 c + \eta_2(1-c), \tag{3.11}$$

where $\eta_1 > 0$ and $\eta_2 > 0$ are the constant dynamic viscosities of the two species.

On Γ, we consider the surface rate-of-strain tensor [41] given by

$$E_s(\mathbf{u}) \coloneqq \frac{1}{2}(\nabla_\Gamma \mathbf{u} + (\nabla_\Gamma \mathbf{u})^T). \tag{3.12}$$

The classical phase-field model to describe the flow of two immiscible, incompressible, and Newtonian fluids is the so-called *Model H* [47]. One of the fundamental assumptions for Model H is that the densities of both components are matching. Several extensions have been proposed to account for the case of non-matching densities; see Chapter 1. Here, we restrict our attention to a thermodynamically consistent generalization of Model H first presented in [2]. For surface based quantities the model reads:

$$\rho \partial_t \mathbf{u} + \rho(\nabla_\Gamma \mathbf{u})\mathbf{u} - \mathbf{P}\,\mathrm{div}_\Gamma(2\eta E_s(\mathbf{u})) + \nabla_\Gamma p = -\sigma_\gamma c \nabla_\Gamma \mu + M \frac{d\rho}{dc}(\nabla_\Gamma \mathbf{u})\nabla_\Gamma \mu + \mathbf{f}, \tag{3.13}$$

$$\mathrm{div}_\Gamma \mathbf{u} = 0, \tag{3.14}$$

$$\partial_t c + \mathrm{div}_\Gamma(c\mathbf{u}) - \mathrm{div}_\Gamma(M \nabla_\Gamma \mu) = 0, \tag{3.15}$$

$$\mu = \frac{1}{\epsilon} f_0' - \epsilon \Delta_\Gamma c, \tag{3.16}$$

on $\Gamma \times (0, T]$, where T is the end of a time interval of interest. Here, $\mathbf{u}$ is the surface averaged tangential velocity $\mathbf{u} = c\mathbf{u}_1 + (1-c)\mathbf{u}_2$, density is given by (3.10) and viscosity by (3.11), σ_γ is line tension and μ is the chemical potential defined in (3.16). A force vector $\mathbf{f}$, with $\mathbf{f} \cdot \mathbf{n} = 0$, is given. We note that system (3.13)–(3.16) is fully tangential, since surface Γ is stationary. For a comprehensive discussion of the related the Navier–Stokes and the Cahn–Hilliard equations on surfaces we refer, for example, to [51, 26, 24].

Problem (3.13)–(3.16) has only one additional term with respect to Model H: the middle term at the right-hand side in eq. (3.13). Notice that this term vanishes in the case of matching densities since $\frac{d\rho}{dc} = (\rho_1 - \rho_2)$. However, the term is crucial for thermodynamic consistency when the densities do not match and it can be interpreted as additional momentum flux due to diffusion of the components driven by the gradient of the chemical potential.

In practice, we are interested in more general relations than (3.10) between ρ and c, since depending on the choice of $f_0(c)$ (and because of numerical errors while computing) the order parameter may not be constrained in $[0, 1]$ and so ρ and η based on (3.10) may take physically meaningless (even negative) values. Since we do not see how to show the thermodynamic consistency of (3.13)–(3.16) for non-linear $\rho(c)$, we propose a further modification. Without the loss of generality let $\rho_1 \geq \rho_2$. For a general dependence of ρ on c, it is reasonable to assume that ρ is a smooth monotonic function of c, i.e., $\frac{d\rho}{dc} \geq 0$ (for $\rho_1 \geq \rho_2$), and so we can set

$$\frac{d\rho}{dc} = \theta^2. \tag{3.17}$$

Then, we replace (3.13) with

$$\rho\partial_t \mathbf{u} + \rho(\nabla_\Gamma \mathbf{u})\mathbf{u} - \mathbf{P}\,\mathrm{div}_\Gamma(2\eta E_s(\mathbf{u})) + \nabla_\Gamma p = -\sigma_\gamma c\nabla_\Gamma \mu + M\theta(\nabla_\Gamma(\theta\mathbf{u})\,)\nabla_\Gamma \mu + \mathbf{f}. \tag{3.18}$$

The updated model (3.18),(3.14)–(3.16) obviously coincides with (3.13)–(3.16) for $\rho(c)$ from (3.10), but exhibits thermodynamic consistency for a general monotone ρ–c relation as we show below. The consistency is preserved if M is a non-negative function of c rather than a constant coefficient. Thermodynamic consistent extensions of (3.13)–(3.16) for a generic smooth $\rho(c)$ (no monotonicity assumption) were also considered in [1, 3] for the purpose of well-posedness analysis. Those extensions introduce yet more term(s) in the momentum equation, so for computational needs and numerical analysis purpose we opt for (3.18).

From now on, we will focus on problem (3.18), (3.14)–(3.16). This is the Navier–Stokes–Cahn–Hilliard (NSCH) system that needs to be supplemented with the definitions of mobility M and

free energy per unit area f_0. Following many of the existing analytic studies, as well as numerical studies, we assume the mobility to be a strictly positive constant (i.e., independent of c). As for f_0, we continue to use (3.8).

For the numerical method, we need a weak (integral) formulation. We define the spaces

$$\mathbf{V}_T \coloneqq \{\, \mathbf{u} \in H^1(\Gamma)^3 \mid \mathbf{u} \cdot \mathbf{n} = 0 \,\}, \quad E \coloneqq \{\, \mathbf{u} \in \mathbf{V}_T \mid E_s(\mathbf{u}) = \mathbf{0} \,\}. \tag{3.19}$$

We define the Hilbert space $\mathbf{V}_T^0$ as an orthogonal complement of E in $\mathbf{V}_T$ (hence $\mathbf{V}_T^0 \sim \mathbf{V}_T/E$), and recall the surface Korn's inequality [51]:

$$\|\mathbf{u}\|_{H^1(\Gamma)} \leq C_K \|E_s(\mathbf{u})\|, \quad \forall\, \mathbf{u} \in \mathbf{V}_T^0. \tag{3.20}$$

In (3.20) and later, we use short notation $\|\cdot\|$ for the L^2-norm on Γ. Finally, we define $L_0^2(\Gamma) \coloneqq \{\, p \in L^2(\Gamma) \mid \int_\Gamma p \, ds = 0 \,\}$. To devise the weak formulation, one multiplies eq. (3.18) by $\mathbf{v} \in \mathbf{V}_T$, eq. (3.14) by $q \in L^2(\Gamma)$, eq. (3.15) by $v \in H^1(\Gamma)$, and eq. (3.16) by $g \in H^1(\Gamma)$ and integrates all the equations over Γ. For eq. (3.18) and (3.15), one employs the integration by parts identity (2.6). Identity (2.6) is applied to the second term in (3.15) (i.e., $\mathbf{g} = c\mathbf{u}$), which leads to no contribution from the curvature term since $\mathbf{u}$ is tangential, and to the third term in (3.15) (i.e., $\mathbf{g} = M\nabla_\Gamma \mu$), which makes the curvature term vanish as well. For a similar reason (component-wise), the curvature term vanishes also when identity (2.6) is applied to the diffusion term in (3.18).

The weak (integral) formulation of the surface NSCH problem (3.18), (3.14)–(3.16) reads: Find

$(\mathbf{u}, p, c, \mu) \in \mathbf{V}_T \times L^2_0(\Gamma) \times H^1(\Gamma) \times H^1(\Gamma)$ such that

$$\int_\Gamma \left(\rho \partial_t \mathbf{u} \cdot \mathbf{v} + \rho(\nabla_\Gamma \mathbf{u})\mathbf{u} \cdot \mathbf{v} + 2\eta E_s(\mathbf{u}) : E_s(\mathbf{v})\right) ds - \int_\Gamma p \, \mathrm{div}_\Gamma \mathbf{v} \, ds = -\int_\Gamma \sigma_\gamma c \nabla_\Gamma \mu \cdot \mathbf{v} \, ds$$
$$+ \int_\Gamma M(\nabla_\Gamma(\theta \mathbf{u}))(\nabla_\Gamma \mu) \cdot (\theta \mathbf{v}) \, ds + \int_\Gamma \mathbf{f} \cdot \mathbf{v} \, ds, \tag{3.21}$$

$$\int_\Gamma q \, \mathrm{div}_\Gamma \mathbf{u} \, ds = 0, \tag{3.22}$$

$$\int_\Gamma \partial_t c \, v \, ds - \int_\Gamma c\mathbf{u} \cdot \nabla_\Gamma v \, ds + \int_\Gamma M \nabla_\Gamma \mu \cdot \nabla_\Gamma v \, ds = 0, \tag{3.23}$$

$$\int_\Gamma \mu \, g \, ds = \int_\Gamma \frac{1}{\epsilon} f_0'(c) \, g \, ds + \int_\Gamma \epsilon \nabla_\Gamma c \cdot \nabla_\Gamma g \, ds, \tag{3.24}$$

for all $(\mathbf{v}, q, v, g) \in \mathbf{V}_T \times L^2(\Gamma) \times H^1(\Gamma) \times H^1(\Gamma)$.

Lemma 3.1. The following energy equality holds for a smooth solution to (3.21)–(3.24):

$$\frac{d}{dt} \int_\Gamma \left(\frac{\rho}{2} |\mathbf{u}|^2 + \sigma_\gamma \left(\frac{1}{\epsilon} f_0 + \frac{\epsilon}{2} |\nabla_\Gamma c|^2 \right) \right) ds + \int_\Gamma 2\eta |E_s(\mathbf{u})|^2 ds + \int_\Gamma \sigma_\gamma M |\nabla_\Gamma \mu|^2 ds = \int_\Gamma \mathbf{f} \cdot \mathbf{u} \, ds. \tag{3.25}$$

In other words, model (3.18), (3.14)–(3.16) is thermodynamically consistent, i.e., the system is dissipative for $\mathbf{f} = \mathbf{0}$.

Proof. We test (3.21) with $\mathbf{v} = \mathbf{u}$, (3.22) with $q = p$, (3.23) with $v = \mu$, and use (3.16). The first two terms in eq. (3.21) tested with $\mathbf{v} = \mathbf{u}$ can be handled as follows:

$$\begin{aligned} \int_\Gamma \left(\rho \partial_t \mathbf{u} \cdot \mathbf{u} + \rho(\nabla_\Gamma \mathbf{u})\mathbf{u} \cdot \mathbf{u}\right) ds &= \int_\Gamma \left(\frac{\rho}{2} \partial_t |\mathbf{u}|^2 - \frac{1}{2} \mathrm{div}_\Gamma(\rho \mathbf{u}) |\mathbf{u}|^2 \right) ds \\ &= \int_\Gamma \left(\frac{1}{2} \partial_t (\rho |\mathbf{u}|^2) - \frac{1}{2} \left(\partial_t \rho + \mathrm{div}_\Gamma(\rho \mathbf{u}) \right) |\mathbf{u}|^2 \right) ds. \end{aligned}$$

Using a generic $\rho = \rho(c)$, (3.17), and (3.14) we get

$$\partial_t \rho + \mathrm{div}_\Gamma(\rho \mathbf{u}) = \frac{d\rho}{dc} \left(\partial_t c + \mathrm{div}_\Gamma(c\mathbf{u}) \right) = \theta^2 \left(\partial_t c + \mathrm{div}_\Gamma(c\mathbf{u}) \right).$$

With the help of (3.15), this yields

$$\int_\Gamma \left(\partial_t \rho + \operatorname{div}_\Gamma(\rho \mathbf{u})\right) |\mathbf{u}|^2 ds = -\int_\Gamma M(\nabla_\Gamma \mu) \cdot (\nabla_\Gamma |\theta \mathbf{u}|^2) ds$$
$$= -2 \int_\Gamma M(\nabla_\Gamma(\theta \mathbf{u}))(\nabla_\Gamma \mu) \cdot (\theta \mathbf{u}) ds,$$

which will cancel with the second term at the right-hand side in eq. (3.21) tested with $\mathbf{v} = \mathbf{u}$. Thus, from eq. (3.21) tested with $\mathbf{v} = \mathbf{u}$, we obtain the following equality:

$$\frac{1}{2}\frac{d}{dt}\int_\Gamma \rho |\mathbf{u}|^2 ds + \int_\Gamma 2\eta |E_s(\mathbf{u})|^2 ds = -\int_\Gamma \sigma_\gamma c \nabla_\Gamma \mu \cdot \mathbf{u}\, ds + \int_\Gamma \mathbf{f} \cdot \mathbf{u}\, ds, \tag{3.26}$$

where we have also used eq. (3.22) tested with $q = p$. From eq. (3.23) tested with $v = \mu$ and multiplied by σ_γ, we get:

$$\int_\Gamma \sigma_\gamma (\mathbf{u} \cdot \nabla_\Gamma c)\, \mu\, ds = -\int_\Gamma \sigma_\gamma (\mathbf{u} \cdot \nabla_\Gamma \mu)\, c\, ds = -\int_\Gamma \sigma_\gamma \partial_t c\, \mu\, ds - \int_\Gamma \sigma_\gamma M |\nabla_\Gamma \mu|^2 ds. \tag{3.27}$$

The first term on the right-hand side can be handled using (3.16) as follows:

$$\int_\Gamma \partial_t c\, \mu\, ds = \int_\Gamma \partial_t c \left(\frac{1}{\epsilon} f_0' - \epsilon \Delta_\Gamma c\right) ds = \frac{d}{dt}\int_\Gamma \left(\frac{1}{\epsilon} f_0 + \frac{\epsilon}{2} |\nabla_\Gamma c|^2\right) ds.$$

Plugging this into (3.27) and then using what we get in (3.26), we obtain the energy balance (3.25). □

4 Numerical methods

In this chapter, we introduce the numerical methods employed to address our computational challenges. For the Cahn-Hilliard equations (3.5) – (3.6), we present two distinct solving approaches. The first method incorporates an additional stabilization term, extensively examined in [115], and is applied to tackle the Cahn-Hilliard component of the decoupled NSCH problem. The second method introduces a scalar auxiliary variable, it is a compelling alternative to the stabilized method.

4.1 Stabilized method for the Cahn–Hilliard model

For the numerical method presented in this chapter, we need a variational formulation of surface problem (3.5)-(3.6). To devise it, we multiply (3.5) by $v \in H^1(\Gamma)$ and (3.6) by $q \in H^1(\Gamma)$, integrate over Γ and employ the integration by parts identity (2.6). This leads to the formulation: Find $(c, \mu) \in H^1(\Gamma) \times H^1(\Gamma)$ such that

$$\int_\Gamma \rho \frac{\partial c}{\partial t}\, v \, ds + \int_\Gamma M \nabla_\Gamma \mu \, \nabla_\Gamma v \, ds = 0, \tag{4.1}$$

$$\int_\Gamma \mu \, q \, ds - \int_\Gamma f_0'(c) \, q \, ds - \int_\Gamma \epsilon^2 \nabla_\Gamma c \, \nabla_\Gamma q \, ds = 0, \tag{4.2}$$

for all $(v, q) \in H^1(\Gamma) \times H^1(\Gamma)$.

4.1.1 Space discretization

For the space discretization of the surface Cahn–Hilliard problem, as well as Navier–Stokes–Cahn–Hilliard system, we apply the trace finite element method (TraceFEM) [83, 115, 88]. This is an unfitted method that allows to solve for scalar or vector fields on surface Γ without the need for a parametrization or triangulation of Γ itself. As typical for unfitted methods, TraceFEM relies on a triangulation of a bulk computational domain Ω ($\Gamma \subset \Omega$ holds) into shape regular tetrahedra "blind" to the position of Γ. Surface Γ is defined implicitly as the zero level set of a sufficiently smooth (at least Lipschitz continuous) function ϕ, i.e., $\Gamma = \{\mathbf{x} \in \Omega : \phi(\mathbf{x}) = 0\}$, such that

$|\nabla\phi| \geq c_0 > 0$ in a 3D neighborhood of the surface.

Let $\mathcal{T}_h$ be the collection of all tetrahedra, such that $\overline{\Omega} = \cup_{T\in\mathcal{T}_h}\overline{T}$. Typically, we refine the grid $\mathcal{T}_h$ near Γ. The subset of tetrahedra that have a *nonzero intersection* with Γ is denoted by $\mathcal{T}_h^\Gamma$. The domain formed by all tetrahedra in $\mathcal{T}_h^\Gamma$ is denoted by Ω_h^Γ. On $\mathcal{T}_h^\Gamma$ we use a standard finite element space of continuous functions that are piecewise-polynomials of degree 1. Obviously, other choices of finite elements are possible (see, e.g., [36]). This bulk (volumetric) finite element space is denoted by V_h:

$$V_h = \{v \in C(\Omega_h^\Gamma) \,:\, v \in P_1(T) \text{ for any } T \in \mathcal{T}_h^\Gamma\}.$$

Finally, to define geometric quantities and for the purpose of numerical integration, we approximate Γ with a "discrete" surface Γ_h, which is defined as the zero level set of a P_1 Lagrangian interpolant ϕ_h for level set function ϕ on the given mesh. The $(\cdot,\cdot)$ inner product and $\|\cdot\|$ norm further denotes the $L^2(\Gamma_h)$ inner product and norm. The approximate normal vector field $\mathbf{n}_h = \nabla\phi_h/|\nabla\phi_h|$ is piecewise smooth on Γ_h. The orthogonal projection into tangential space is given by $\mathbf{P}_h(\mathbf{x}) = \mathbf{I} - \mathbf{n}_h(\mathbf{x})\mathbf{n}_h^T(\mathbf{x})$ for almost all $\mathbf{x} \in \Gamma_h$. For $v \in V_h$, the surface gradient on Γ_h is easy to compute from the bulk gradient $\nabla_{\Gamma_h} v = \mathbf{P}_h \nabla v$.

4.1.2 Semi-implicit stabilized TraceFEM for the Cahn–Hilliard model

For time-stepping we apply a semi-implicit stabilized schemes from [97, 115]. At time instance $t^k = k\Delta t$, with time step $\Delta t = \frac{T}{N}$, c^k denotes the approximation of the concentration $c(t^k, \mathbf{x})$; similar notation is used for other quantities of interest. Further, we need second order approximations of first and second time derivatives [97, 115]:

$$[c]_t^k = \frac{3c^k - 4c^{k-1} + c^{k-2}}{2\Delta t}, \quad [c]_{tt}^k = \frac{c^{k+1} - 2c^k + c^{k-1}}{|\Delta t|^2}, \tag{4.3}$$

and linear extrapolation for f_0' at time t^k: $\widetilde{f_0'}(c)^k = 2f_0'(c^{k-1}) - f_0'(c^{k-2})$. Same notations for differences and extrapolation will be used with other variables.

The finite element discretizations are based on the weak formulation of the surface Cahn–Hilliard

problem (4.1)–(4.2). The semi-implicit stabilized TraceFEM for the Cahn–Hilliard equations reads: Given $c_h^{k-1}, c_h^{k-2} \in V_h$ and $\mu_h^{k-1}, \mu_h^{k-2} \in V_h$, find $c_h^k, \mu^k \in V_h$ solving

$$\begin{aligned}\int_{\Gamma_h} \rho\,[c_h]_t^k\, v_h\, ds + \int_{\Gamma_h} M(\widetilde{c}^k)\nabla_{\Gamma_h}\mu_h^k \cdot \nabla_{\Gamma_h} v_h\, ds + \underbrace{h\int_{\Omega_h^\Gamma} (\mathbf{n}_h\cdot\nabla\mu_h^k)(\mathbf{n}_h\cdot\nabla v_h)\, dx}_{J_1} \\ + \int_{\Gamma_h}\left(\mu_h^k - \underbrace{\beta_s|\Delta t|^2\,[c_h]_{tt}^{k-1}}_{J_2} - \widetilde{f}_0'(c_h)^k\right) q_h\, ds - \int_{\Gamma_h}\epsilon^2\nabla_\Gamma c_h^k\,\nabla_\Gamma q_h\, ds \\ \underbrace{-\epsilon^2 h\int_{\Omega_h^\Gamma}(\mathbf{n}_h\cdot\nabla c_h^k)(\mathbf{n}_h\cdot\nabla q_h)\, dx}_{J_3} = 0\end{aligned} \tag{4.4}$$

for all $v_h \in V_h$ and $q_h \in V_h$, $k = 2, 3, \ldots, N$. For $k = 1$, an obvious first order modification is used and we set $\beta_s = 1$.

In the equation (4.4), three stabilization terms are introduced. J_1 and J_3 are included to deal with possible small cuts of tetrahedra from $\mathcal{T}_h^\Gamma$ by the surface [36]. The terms are consistent up to geometric errors related to the approximation of Γ by Γ_h and $\mathbf{n}$ by $\mathbf{n}_h$ in the following sense: any smooth solution c of equations (4.4) can be always extended off the surface along (quasi)-normal directions so that $\mathbf{n}\cdot\nabla c = 0$ in Ω_h^Γ. The stabilization term J_2 with an user defined parameter β_s is included to relax the stability restriction for the time step Δt. It introduces the consistency error of second order in time. This stabilization term is an important ingredient of the formulation (4.4), and with SAV method presented next we seek remove it.

4.2 A scalar auxiliary variable FEM for the Cahn–Hilliard equations

Straightforward calculations show that for constant mobility M, the Cahn–Hilliard problem defines gradient flows of the energy functional

$$E(c) = \int_\Gamma f(c)\, ds = \int_\Gamma \frac{1}{2}\epsilon^2|\nabla_\Gamma c|^2\, ds + E_1(c), \quad \text{with } E_1(c) = \int_\Gamma f_0(c)\, ds, \tag{4.5}$$

in $H^{-1}(\Gamma)$ (a dual space to $H^1(\Gamma)$). For the degenerate mobility, the Cahn–Hilliard problem is known to define gradient flows in a weighted-Wasserstein metric [70]. Incorporating various definitions of mobility $M(c)$ into the Cahn-Hilliard equations can exert a notable impact on the dynamic behavior of c, even without altering the energy landscape. Thanks to gradient structure mentioned above, the following energy dissipation property holds:

$$\frac{d}{dt}E(c) < 0. \tag{4.6}$$

A time discretization scheme for problem (3.5),(3.6) is said to be energy stable if it satisfies a discrete energy dissipation law, i.e., it needs to adhere to fundamental property (4.6). In this paper, we construct an energy stable scheme for (3.5),(3.6) using the scalar auxiliary variable (SAV) approach. See [96] for a review of SAV methods for a general class of gradient flow problems. As the name suggests, this method introduces a scalar auxiliary variable

$$r(t) = \sqrt{E_1(c(t)) + C}, \tag{4.7}$$

where a constant $C \geq 0$ can be added to ensure that $r(t)$ is well defined. Without loss of generality, for the rest of the paper we will assume that $E_1(c) > 0$, i.e., $C = 0$. Then, the system (3.5),(3.6) can be rewritten as follows:

$$\rho\frac{\partial c}{\partial t} = \operatorname{div}_\Gamma\left(M(c)\nabla_\Gamma\mu\right) \qquad \text{on } \Gamma \times (0,T], \tag{4.8}$$

$$\mu = \frac{r(t)}{\sqrt{E_1(c)}}f_0' - \epsilon^2\Delta_\Gamma c \qquad \text{on } \Gamma \times (0,T], \tag{4.9}$$

$$\frac{dr}{dt} = \frac{1}{2\sqrt{E_1(c)}}\int_\Gamma f_0'(c)\frac{\partial c}{\partial t}ds \qquad \text{on } \Gamma \times (0,T]. \tag{4.10}$$

System (4.8)-(4.10) represents the starting point for the construction of our energy stable SAV scheme.

For the numerical method, we need a variational formulation of surface problem (4.8)-(4.10). We

will write the weak formulation similar to (4.1)–(4.2), which then reads: Find $(c, \mu) \in H^1(\Gamma) \times H^1(\Gamma)$ such that

$$\int_\Gamma \rho \frac{\partial c}{\partial t}\, v\, ds = -\int_\Gamma M(c) \nabla_\Gamma \mu\, \nabla_\Gamma v\, ds, \tag{4.11}$$

$$\int_\Gamma \mu\, q\, ds = \int_\Gamma \frac{r(t)}{\sqrt{E_1(c)}} f_0'(c)\, q\, ds + \int_\Gamma \epsilon^2 \nabla_\Gamma c\, \nabla_\Gamma q\, ds, \tag{4.12}$$

for all $(v, q) \in H^1(\Gamma) \times H^1(\Gamma)$, while (4.10) remains unchanged.

The majority of the papers available in the literature on SAV methods for the Cahn-Hilliard problem employs constant mobility. Nevertheless, degenerate mobility has been considered in many practical applications (see, e.g., [115]) and is non-trivial to handle numerically (see, e.g., [39] for recent advances). The only paper that proposes a SAV approach for the Cahn–Hilliard equation with degenerate mobility is [49].

4.2.1 Space and time discretization

For spatial discretization, we will use the same approach as in the previous stabilized method. Then, the variational problem (4.10)–(4.12) discretized in space by TraceFEM and in time by the implicit Euler (also called BDF1) scheme reads: Given c_0 and the associated $E_1(c_0)$ and r_0 (4.7), for $n \geq 0$ at time step t^{n+1} find $(c_h^{n+1}, \mu_h^{n+1}, r_h^{n+1}) \in V_h \times V_h \times \mathbb{R}$ such that

$$\rho(c_h^{n+1} - c_h^n, v_h) = -\Delta t (M(c^n) \nabla_{\Gamma_h} \mu_h^{n+1}, \nabla_{\Gamma_h} v_h) - h \Delta t \int_{\Omega_h^\Gamma} (\mathbf{n}_h \cdot \nabla \mu_h^{n+1})(\mathbf{n}_h \cdot \nabla v_h) dx, \tag{4.13}$$

$$(\mu_h^{n+1}, q_h) = \frac{r_h^{n+1}}{\sqrt{E_1(c_h^n)}} (f_0'(c_h^n), q_h) + \epsilon^2 (\nabla_{\Gamma_h} c_h^{n+1}, \nabla_{\Gamma_h} q_h) + h^{-1} \epsilon^2 \int_{\Omega_h^\Gamma} (\mathbf{n}_h \cdot \nabla c_h^{n+1})(\mathbf{n}_h \cdot \nabla q_h) dx, \tag{4.14}$$

$$r_h^{n+1} - r_h^n = \frac{1}{2\sqrt{E_1(c_h^n)}} (f_0'(c_h^n), c_h^{n+1} - c_h^n) \tag{4.15}$$

for all $(v_h, q_h) \in V_h \times V_h$. Again, the volumetric terms in (4.13)–(4.14) are included to stabilize the resulting algebraic systems [14, 36]. Notice that the nonlinear terms in (4.13)–(4.15) have been

linearized with a first order extrapolation. We will call this approach SAV-BDF1.

Theorem 4.1. Let

$$\tilde{E}_h^{n+1} = \frac{\epsilon^2}{2}\left\|\nabla_{\Gamma_h} c_h^{n+1}\right\|^2 + \left|r_h^{n+1}\right|^2 + h\epsilon^2\left\|\mathbf{n}_h \cdot \nabla c_h^{n+1}\right\|^2_{L^2(\Omega_h^\Gamma)}. \tag{4.16}$$

be the modified discrete energy. Scheme (4.13)–(4.15) admits the following energy balance

$$\begin{aligned}\left(\tilde{E}_h^{n+1} - \tilde{E}_h^n\right) + \frac{\epsilon^2}{2}\left\|\nabla_{\Gamma_h} c_h^{n+1} - \nabla_{\Gamma_h} c_h^{n-1}\right\|^2 + \left|r_h^{n+1} - r_h^n\right|^2 + \frac{h\epsilon^2}{2}\left\|\mathbf{n}_h \cdot \nabla(c_h^{n+1} - c_h^n)\right\|^2_{L^2(\Omega_h^\Gamma)} \\ = -\frac{\Delta t}{\rho}(M(\widetilde{c}^n)\nabla_{\Gamma_h}\mu_h^{n+1}, \nabla_{\Gamma_h}\mu_h^{n+1}) - \frac{h\Delta t}{\rho}\left\|\mathbf{n}_h \cdot \nabla\mu_h^{n+1}\right\|^2_{L^2(\Omega_h^\Gamma)}.\end{aligned} \tag{4.17}$$

In particular, this implies that the scheme (4.13)–(4.15) is energy stable in the sense that $\tilde{E}_h^{n+1} \leq \tilde{E}_h^n$, which is the discrete analogue of (4.6), for all $n = 0, 1, 2, \ldots$.

Proof. Combine the equations obtained from taking $v_h = \mu_h^{n+1}/\rho$ in (4.13) and $q_h = (c_h^{n+1} - c_h^n)$ in (4.14) to get

$$\begin{aligned}\frac{r_h^{n+1}}{\sqrt{E_1(c_h^n)}}(f_0'(c_h^n), c_h^{n+1} - c_h^n) + \epsilon^2(\nabla_{\Gamma_h} c_h^{n+1}, \nabla_{\Gamma_h}(c_h^{n+1} - c_h^n)) \\ + h^{-1}\epsilon^2\int_{\Omega_h^\Gamma}(\mathbf{n}_h \cdot \nabla c_h^{n+1})(\mathbf{n}_h \cdot \nabla(c_h^{n+1} - c_h^n))dx \\ = -\frac{\Delta t}{\rho}(M(\widetilde{c}^n)\nabla_{\Gamma_h}\mu_h^{n+1}, \nabla_{\Gamma_h}\mu_h^{n+1}) - \frac{h\Delta t}{\rho}\left\|\mathbf{n}_h \cdot \nabla\mu_h^{n+1}\right\|^2_{L^2(\Omega_h^\Gamma)}.\end{aligned} \tag{4.18}$$

By plugging (4.15) multiplied by $2r_h^{n+1}$ into (4.18), we obtain:

$$\begin{aligned}2r_h^{n+1}(r_h^{n+1} - r_h^n) + \epsilon^2(\nabla_{\Gamma_h} c_h^{n+1}, \nabla_{\Gamma_h}(c_h^{n+1} - c_h^n)) + h^{-1}\epsilon^2\int_{\Omega_h^\Gamma}(\mathbf{n}_h \cdot \nabla c_h^{n+1})(\mathbf{n}_h \cdot \nabla(c_h^{n+1} - c_h^n))dx \\ = -\frac{\Delta t}{\rho}(M(\widetilde{c}^n)\nabla_{\Gamma_h}\mu_h^{n+1}, \nabla_{\Gamma_h}\mu_h^{n+1}) - \frac{h\Delta t}{\rho}\left\|\mathbf{n}_h \cdot \nabla\mu_h^{n+1}\right\|^2_{L^2(\Omega_h^\Gamma)}.\end{aligned} \tag{4.19}$$

Using the identity

$$2\left(a^{k+1}, a^{k+1} - a^k\right) = \left|a^{k+1}\right|^2 - \left|a^k\right|^2 + \left(a^{k+1} - a^k\right)^2$$

in (4.19) leads to (4.17). □

We see that introducing the auxiliary variable r allows for an unconditionally stable scheme with the explicit treatment of the non-linear term. The same conclusion will be true for the second order scheme introduced next.

For a second order scheme in time, we adopt Backward Differentiation Formula of order 2 (BDF2). A second order approximation of a first time derivative and a linear extrapolation of second order at time t^n:

$$\frac{\partial c}{\partial t} \approx \frac{3c^n - 4c^{n-1} + c^{n-2}}{2\Delta t}, \quad \tilde{c}^n = 2c^{n-1} - c^{n-2}, \tag{4.20}$$

respectively. Then, the space and time discrete version of problem (4.10)-(4.12) reads: Given c_0 and the associated $E_1(c_0)$ and r_0 (4.7), find $(c_h^1, \mu_h^1, r_h^1) \in V_h \times V_h \times \mathbb{R}$ such that (4.13)-(4.15) hold and for $n \geq 1$ at time step t^{n+1} find $(c_h^{n+1}, \mu_h^{n+1}, r_h^{n+1}) \in V_h \times V_h \times \mathbb{R}$ such that

$$\frac{\rho}{2\Delta t}\left(3c_h^{n+1} - 4c_h^n + c_h^{n-1}, v_h\right) = -(M(\tilde{c}_h^n)\nabla_{\Gamma_h}\mu_h^{n+1}, \nabla_{\Gamma_h} v_h) - h\int_{\Omega_h^\Gamma} (\mathbf{n}_h \cdot \nabla \mu_h^{n+1})(\mathbf{n}_h \cdot \nabla v_h) dx, \tag{4.21}$$

$$(\mu_h^{n+1}, q_h) = \frac{r_h^{n+1}}{\sqrt{E_1(\tilde{c}_h^n)}}(f_0'(\tilde{c}_h^n), q_h) + \epsilon^2(\nabla_{\Gamma_h} c_h^{n+1}, \nabla_{\Gamma_h} q_h) + h^{-1}\epsilon^2 \int_{\Omega_h^\Gamma} (\mathbf{n}_h \cdot \nabla c_h^{n+1})(\mathbf{n}_h \cdot \nabla q_h) dx, \tag{4.22}$$

$$3r_h^{n+1} - 4r_h^n + r_h^{n-1} = \frac{1}{2\sqrt{E_1(\tilde{c}_h^n)}}(f_0'(\tilde{c}_h^n), 3c_h^{n+1} - 4c_h^n + c_h^{n-1}), \tag{4.23}$$

for all $(v_h, q_h) \in V_h \times V_h$. We will call this approach SAV-BDF2.

Theorem 4.2. Let

$$\begin{aligned}\tilde{E}_h^{n+1} =& \frac{\epsilon^2}{2}\left\|\nabla_{\Gamma_h} c_h^{n+1}\right\|^2 + \frac{\epsilon^2}{2}\left\|2\nabla_{\Gamma_h} c_h^{n+1} - \nabla_{\Gamma_h} c_h^n\right\|^2 + \left|r_h^{n+1}\right|^2 + \left|2r_h^{n+1} - r_h^n\right|^2 \\ &+ \frac{h\epsilon^2}{2}\left\|\mathbf{n}_h \cdot \nabla c_h^{n+1}\right\|^2_{L^2(\Omega_h^\Gamma)} + \frac{h^{-1}\epsilon^2}{2}\left\|(\mathbf{n}_h \cdot \nabla(2c_h^{n+1} - c_h^n)\right\|^2_{L^2(\Omega_h^\Gamma)}\end{aligned} \tag{4.24}$$

be the modified discrete energy. Scheme (4.13)–(4.15) admits the following energy balance

$$\begin{aligned}
&\left(\tilde{E}_h^{n+1}-\tilde{E}_h^n\right)+\frac{\epsilon^2}{2}\left\|\nabla_{\Gamma_h}c_h^{n+1}-2\nabla_{\Gamma_h}c_h^n+\nabla_{\Gamma_h}c_h^{n-1}\right\|^2+\left|r_h^{n+1}-2r_h^n+r_h^{n-1}\right|^2\\
&\quad+\frac{h\epsilon^2}{2}\left\|\mathbf{n}_h\cdot\nabla(c_h^{n+1}-2c_h^n+c_h^{n-1})\right\|^2_{L^2(\Omega_h^\Gamma)}=-\frac{2\Delta t}{\rho}(M(\widetilde{c}^n)\nabla_{\Gamma_h}\mu_h^{n+1},\nabla_{\Gamma_h}\mu_h^{n+1})\\
&\quad-\frac{2h\Delta t}{\rho}\left\|\mathbf{n}_h\cdot\nabla\mu_h^{n+1}\right\|^2_{L^2(\Omega_h^\Gamma)}.
\end{aligned}\tag{4.25}$$

In particular, this implies that the scheme (4.13)–(4.15) is energy stable in the sense that $\tilde{E}_h^{n+1}\leq\tilde{E}_h^n$, which is the discrete analogue of (4.6), for all $n=0,1,2,\ldots$.

Proof. Combine the equations obtained from taking $v_h=2\Delta t\mu_h^{n+1}/\rho$ in (4.21), $q_h=(3c_h^{n+1}-4c_h^n+c_h^{n-1})$ in (4.22) to get

$$\begin{aligned}
&\frac{r_h^{n+1}}{\sqrt{E_1(\tilde{c}_h^n)}}(f_0'(\tilde{c}_h^n),3c_h^{n+1}-4c_h^n+c_h^{n-1})+\epsilon^2(\nabla_{\Gamma_h}c_h^{n+1},\nabla_{\Gamma_h}(3c_h^{n+1}-4c_h^n+c_h^{n-1}))\\
&\quad+h^{-1}\epsilon^2\int_{\Omega_h^\Gamma}(\mathbf{n}_h\cdot\nabla c_h^{n+1})(\mathbf{n}_h\cdot\nabla(3c_h^{n+1}-4c_h^n+c_h^{n-1}))dx=-\frac{2\Delta t}{\rho}(M(\widetilde{c}^n)\nabla_{\Gamma_h}\mu_h^{n+1},\nabla_{\Gamma_h}\mu_h^{n+1})\\
&\quad-\frac{2h\Delta t}{\rho}\left\|\mathbf{n}_h\cdot\nabla\mu_h^{n+1}\right\|^2_{L^2(\Omega_h^\Gamma)}.
\end{aligned}\tag{4.26}$$

By plugging (4.23) multiplied by $2r_h^{n+1}$ into (4.26), we obtain

$$\begin{aligned}
&2r_h^{n+1}(3r_h^{n+1}-4r_h^n+r_h^{n-1})+\epsilon^2(\nabla_{\Gamma_h}c_h^{n+1},\nabla_{\Gamma_h}(3c_h^{n+1}-4c_h^n+c_h^{n-1}))\\
&\quad+h^{-1}\epsilon^2\int_{\Omega_h^\Gamma}(\mathbf{n}_h\cdot\nabla c_h^{n+1})(\mathbf{n}_h\cdot\nabla(3c_h^{n+1}-4c_h^n+c_h^{n-1}))dx=-\frac{2\Delta t}{\rho}(M(\widetilde{c}^n)\nabla_{\Gamma_h}\mu_h^{n+1},\nabla_{\Gamma_h}\mu_h^{n+1})\\
&\quad-\frac{2h\Delta t}{\rho}\int_{\Omega_h^\Gamma}(\mathbf{n}_h\cdot\nabla\mu_h^{n+1})(\mathbf{n}_h\cdot\nabla\mu_h^{n+1})dx.
\end{aligned}$$

Let us make use of the identity

$$\begin{aligned}
2\left(a^{k+1},3a^{k+1}-4a^k+a^{k-1}\right)&=\left|a^{k+1}\right|^2+\left|2a^{k+1}-a^k\right|^2+\left|a^{k+1}-2a^k+a^{k-1}\right|^2\\
&\quad-\left|a^k\right|^2-\left|2a^k-a^{k-1}\right|^2
\end{aligned}\tag{4.27}$$

to get:

$$
\begin{aligned}
&\left|r_h^{n+1}\right|^2 + \left|2r_h^{n+1} - r_h^n\right|^2 + \left|r_h^{n+1} - 2r_h^n + r_h^{n-1}\right|^2 - \left|r_h^n\right|^2 - \left|2r_h^n - r_h^{n-1}\right|^2 + \frac{\epsilon^2}{2}\left\|\nabla_{\Gamma_h} c_h^{n+1}\right\|^2 \\
&+ \frac{\epsilon^2}{2}\left\|2\nabla_{\Gamma_h} c_h^{n+1} - \nabla_{\Gamma_h} c_h^n\right\|^2 + \frac{\epsilon^2}{2}\left\|\nabla_{\Gamma_h} c_h^{n+1} - 2\nabla_{\Gamma_h} c_h^n + \nabla_{\Gamma_h} c_h^{n-1}\right\|^2 - \frac{\epsilon^2}{2}\left\|\nabla_{\Gamma_h} c_h^n\right\|^2 - \frac{\epsilon^2}{2}\left\|2\nabla_{\Gamma_h} c_h^n - \nabla_{\Gamma_h} c_h^{n-1}\right\|^2 \\
&+ \frac{h\epsilon^2}{2}\left\|\mathbf{n}_h \cdot \nabla c_h^{n+1}\right\|^2_{L^2(\Omega_h^\Gamma)} + \frac{h\epsilon^2}{2}\left\|\mathbf{n}_h \cdot \nabla(2c_h^{n+1} - c_h^n)\right\|^2_{L^2(\Omega_h^\Gamma)} + \frac{h\epsilon^2}{2}\left\|\mathbf{n}_h \cdot \nabla(c_h^{n+1} - 2c_h^n + c_h^{n-1}\right\|^2_{L^2(\Omega_h^\Gamma)} \\
&- \frac{h\epsilon^2}{2}\left\|\mathbf{n}_h \cdot \nabla c_h^n\right\|^2_{L^2(\Omega_h^\Gamma)} - \frac{h\epsilon^2}{2}\left\|\mathbf{n}_h \cdot \nabla(2c_h^n - c_h^{n-1})\right\|^2_{L^2(\Omega_h^\Gamma)} = -\frac{2\Delta t}{\rho}(M(\widetilde{c}^n)\nabla_{\Gamma_h}\mu_h^{n+1}, \nabla_{\Gamma_h}\mu_h^{n+1}) \\
&- \frac{2h\Delta t}{\rho}\int_{\Omega_h^\Gamma}(\mathbf{n}_h \cdot \nabla\mu_h^{n+1})(\mathbf{n}_h \cdot \nabla\mu_h^{n+1})dx,
\end{aligned}
$$

which corresponds to (4.25). □

Note that both SAV-BDF1 and SAV-BDF2 finite element methods preserve the conservation property $\frac{d}{dt}\int_\Gamma c\,dx = 0$ of the Cahn-Hilliard equation posed on a closed smooth surface. One can see this by letting $v_h = \text{const} \neq 0$ in (4.13) and (4.21), which is a legitimate test function from V_h.

4.2.2 Implementation

Schemes (4.13)–(4.15) and (4.21)–(4.23) can be conveniently rewritten as relatively minor modifications of a "standard" mixed TraceFEM for the surface Cahn–Hilliard problem.

By plugging r_h^{n+1} obtained from (4.15) into eq. (4.14), we can rewrite problem (4.13)–(4.15) as: Given c_0 and the associated $E_1(c_0)$ and r_0 (4.7), for $n \geq 0$ at time step t^{n+1} find $(c_h^{n+1}, \mu_h^{n+1}) \in V_h \times V_h$

$$
\frac{\rho}{\Delta t}(c_h^{n+1}, v_h) + (M(c^n)\nabla_{\Gamma_h}\mu_h^{n+1}, \nabla_{\Gamma_h} v_h) + h\int_{\Omega_h^\Gamma}(\mathbf{n}_h \cdot \nabla\mu_h^{n+1})(\mathbf{n}_h \cdot \nabla v_h)dx = \frac{\rho}{\Delta t}(c_h^n, v_h), \tag{4.28}
$$

$$
\begin{aligned}
&(\mu_h^{n+1}, q_h) - \epsilon^2(\nabla c_h^{n+1}, \nabla q_h) - h^{-1}\epsilon^2\int_{\Omega_h^\Gamma}(\mathbf{n}_h \cdot \nabla c_h^{n+1})(\mathbf{n}_h \cdot \nabla q_h)dx \\
&\quad - \frac{1}{2E_1(c_h^n)}(f_0'(c_h^n), c_h^{n+1})(f_0'(c_h^n), q_h) \\
&\quad = \frac{r_h^n}{\sqrt{E_1(c_h^n)}}(f_0'(c_h^n), q_h) - \frac{1}{2E_1(c_h^n)}(f_0'(c_h^n), c_h^n)(f_0'(c_h^n), q_h)
\end{aligned} \tag{4.29}
$$

for all $(v_h, q_h) \in V_h \times V_h$. The only differences between (4.28)–(4.29) and a standard TraceFEM for the surface Cahn–Hilliard problem with the implicit Euler scheme for time discretization are the additional last term at the left-hand side in (4.29), which corresponds to a rank-one matrix in the algebraic form of the problem, and the modified terms at the right-hand side in (4.29). At every time step t^{n+1}, the value of the auxiliary variable is computed with (4.15).

In a similar way, we plug r_h^{n+1} obtained from (4.23) into eq. (4.22) and rewrite problem (4.21)–(4.23) as: Given c_0 and the associated $E_1(c_0)$ and r_0 (4.7), find $(c_h^1, \mu_h^1) \in V_h \times V_h$ such that (4.28)-(4.29) hold and get r_h^1 from (4.15), then for $n \geq 1$ at time step t^{n+1} find $(c_h^{n+1}, \mu_h^{n+1}) \in V_h \times V_h$ such that

$$\frac{\rho}{2\Delta t}(3c_h^{n+1}, v_h) + (M(\widetilde{c}^n)\nabla_{\Gamma_h}\mu_h^{n+1}, \nabla_{\Gamma_h} v_h) + h\int_{\Omega_h^\Gamma}(\mathbf{n}_h \cdot \nabla\mu_h^{n+1})(\mathbf{n}_h \cdot \nabla v_h)dx = b_c^{n+1}, \tag{4.30}$$

$$\begin{aligned}(\mu_h^{n+1}, q_h) - \epsilon^2(\nabla_{\Gamma_h} c_h^{n+1}, \nabla_{\Gamma_h} q_h) - h^{-1}\epsilon^2\int_{\Omega_h^\Gamma}(\mathbf{n}_h \cdot \nabla c_h^{n+1})(\mathbf{n}_h \cdot \nabla q_h)dx \\ - \frac{1}{2E_1(c_h^n)}(f_0'(\tilde{c}_h^n), c_h^{n+1})(f_0'(\tilde{c}_h^n), q_h) = b_\mu^{n+1},\end{aligned} \tag{4.31}$$

for all $(v_h, q_h) \in V_h \times V_h$. The forcing terms in (4.30)–(4.31) are computed from known quantities

$$\begin{aligned}b_c^{n+1} &= \frac{2\rho}{\Delta t}(c_h^n, v_h) - \frac{\rho}{2\Delta t}(c_h^{n-1}, v_h), \\ b_\mu^{n+1} &= \frac{4r_h^n}{3\sqrt{E_1(c_h^n)}}(f_0'(\tilde{c}_h^n), q_h) - \frac{r_h^{n-1}}{3\sqrt{E_1(c_h^n)}}(f_0'(\tilde{c}_h^n), q_h) - \frac{2}{3E_1(c_h^n)}(f_0'(\tilde{c}_h^n), c_h^n)(f_0'(\tilde{c}_h^n), q_h) \\ &\quad + \frac{1}{6E_1(c_h^n)}(f_0'(\tilde{c}_h^n), c_h^{n-1})(f_0'(\tilde{c}_h^n), q_h).\end{aligned}$$

These forcing terms and the last term at the left-hand side in (4.31) are the only differences with respect to a standard TraceFEM for the surface Cahn–Hilliard problem with BDF2 for time discretization. At every time step t^{n+1}, the value of the auxiliary variable is computed with (4.23).

For the numerical results in Chapter 5, we use the SAV-BDF2 scheme. In summary, we implement it as follows:

- *Step 0*: from c_0, get $E_1(c_0)$ as in (4.5) and r_0 from (4.7).

- *Step 1*: at $t^1 = \Delta t$, solve (4.28)-(4.29) to get (c_h^1, μ_h^1) and compute r_h^1 from (4.15).

- *Step 2*: at time t^{n+1}, $n \geq 1$, solve (4.30)-(4.31) to get (c_h^{n+1}, μ_h^{n+1}) and compute r_h^{n+1} from (4.23).

The implementation described above differs from the one presented in the original papers on SAV schemes for gradient flows [48, 64, 96]. In those papers, the properties of the finite difference method on uniform grids were utilized to enhance computational efficiency. However, since we have chosen to work with finite elements for greater geometric flexibility, we cannot leverage the same properties. As a result, we decided to rewrite the SAV scheme as a minor modification of a standard finite element discretization to simplify the implementation process. Consequently, the additional terms introduced by the SAV method lead to dense matrices in the associated linear systems.

4.2.3 Adaptive time-stepping scheme

The solution of the Cahn–Hilliard equation exhibits significant temporal scale variations. Initially, a rapid phase of spinodal decomposition is observed, which can be adequately captured with a small time step (e.g., $\Delta t = \mathcal{O}(10^{-5})$). This phase is followed by a slower process of domain coarsening and growth, for which a larger time step can be employed (e.g., Δt ranging from 10^{-1} to 10). As the phase separation process approaches equilibrium, the time step can be further increased (e.g., up to $\Delta t = \mathcal{O}(10^3)$). In the literature, various approaches can be found where different time-step sizes are manually set during the simulation. See, e.g., [115]. However, a more intelligent approach to handle such a wide range of temporal scales is to employ an adaptive-in-time method that selects the time step based on an accuracy criterion.

We choose to apply the adaptive time stepping technique first presented in [33]. Before explaining the algorithm and how the time step is chosen, let us write the time discretization of the space-discrete version of problem (4.10)-(4.2) using the BDF2 scheme with a variable time step. Let $\Delta t^n = t^{n+1} - t^n$ be the variable time step and set $\omega^n = \Delta t^n / \Delta t^{n-1}$. At time t^{n+1}, the time

derivative is approximated as follows

$$\frac{\partial c}{\partial t} \approx \frac{\alpha c^{n+1} - \beta c^n + \gamma c^{n-1}}{\Delta t}, \quad \alpha = \frac{1+2\omega^n}{1+\omega^n}, \quad \beta = 1+\omega^n, \quad \gamma = \frac{(\omega^n)^2}{1+\omega^n}.$$

Then, the fully discrete problem reads: for $n \geq 1$ at time step t^{n+1} find $(c_h^{n+1}, \mu_h^{n+1}, r_h^{n+1}) \in V_h \times V_h \times \mathbb{R}$ such that

$$\frac{\rho}{\Delta t}\left(\alpha c_h^{n+1} - \beta c_h^n + \gamma c_h^{n-1}, v_h\right) = -(M(\tilde{c}_h^n)\nabla_{\Gamma_h}\mu_h^{n+1}, \nabla_{\Gamma_h} v_h) - h\int_{\Omega_h^\Gamma} (\mathbf{n}_h \cdot \nabla \mu_h^{n+1})(\mathbf{n}_h \cdot \nabla v_h) dx, \tag{4.32}$$

$$\alpha r_h^{n+1} - \beta r_h^n + \gamma r_h^{n-1} = \frac{1}{2\sqrt{E_1(\tilde{c}_h^n)}}(f_0'(\tilde{c}_h^n), \alpha c_h^{n+1} - \beta c_h^n + \gamma c_h^{n-1}), \tag{4.33}$$

and (4.22) hold for all $(v_h, q_h) \in V_h \times V_h$. The formula to compute $\tilde{c}_h^n$ is (4.20).

For the implementation of (4.22),(4.32),(4.33), we proceed as explained in Sec. 4.2.2, i.e., we plug r_h^{n+1} obtained from (4.33) into eq. (4.22) and rewrite problem (4.22),(4.32),(4.33) as: for $n \geq 1$ at time step t^{n+1} find $(c_h^{n+1}, \mu_h^{n+1}) \in V_h \times V_h$ such that

$$\frac{\rho}{\Delta t}(\alpha c_h^{n+1}, v_h) + (M(\tilde{c}^n)\nabla_{\Gamma_h}\mu_h^{n+1}, \nabla_{\Gamma_h} v_h) + h\int_{\Omega_h^\Gamma} (\mathbf{n}_h \cdot \nabla \mu_h^{n+1})(\mathbf{n}_h \cdot \nabla v_h) dx = d_c^{n+1}, \tag{4.34}$$

$$\begin{aligned}(\mu_h^{n+1}, q_h) - \epsilon^2(\nabla_{\Gamma_h} c_h^{n+1}, \nabla_{\Gamma_h} q_h) - h^{-1}\epsilon^2 \int_{\Omega_h^\Gamma} (\mathbf{n}_h \cdot \nabla c_h^{n+1})(\mathbf{n}_h \cdot \nabla q_h) dx \\ - \frac{1}{2E_1(c_h^n)}(f_0'(\tilde{c}_h^n), c_h^{n+1})(f_0'(\tilde{c}_h^n), q_h) = d_\mu^{n+1},\end{aligned} \tag{4.35}$$

for all $(v_h, q_h) \in V_h \times V_h$. The forcing terms in (4.34)-(4.35) are computed from known quantities

$$\begin{aligned}d_c^{n+1} &= \frac{\rho}{\Delta t}(\beta c_h^n, v_h) - \frac{\rho}{\Delta t}(\gamma c_h^{n-1}, v_h), \\ d_\mu^{n+1} &= \frac{\beta r_h^n}{\alpha\sqrt{E_1(c_h^n)}}(f_0'(\tilde{c}_h^n), q_h) - \frac{\gamma r_h^{n-1}}{\alpha\sqrt{E_1(c_h^n)}}(f_0'(\tilde{c}_h^n), q_h) - \frac{\beta}{2\alpha E_1(c_h^n)}(f_0'(\tilde{c}_h^n), c_h^n)(f_0'(\tilde{c}_h^n), q_h) \\ &\quad + \frac{\gamma}{2\alpha E_1(c_h^n)}(f_0'(\tilde{c}_h^n), c_h^{n-1})(f_0'(\tilde{c}_h^n), q_h).\end{aligned}$$

Now, let us describe the adaptive time stepping technique. Let us call $c_{h,1}^{n+1}$ and $c_{h,2}^{n+1}$ the solutions at time t^{n+1} of (4.28)-(4.29) and (4.34)-(4.35), respectively. We define

$$e^{n+1} = \frac{\|c_{h,1}^{n+1} - c_{h,2}^{n+1}\|}{\|c_{h,2}^{n+1}\|}, \tag{4.36}$$

which is taken as input to update the time step:

$$\Delta t^{n+1} \leftarrow F(e^{n+1}, \Delta t^{n+1}) = \zeta \Big(\frac{tol}{e^{n+1}}\Big)^{1/2} \Delta t^{n+1}, \tag{4.37}$$

where ζ is a "safety" coefficient and *tol* is a user prescribed tolerance. Algorithm 1 describes the steps to take at time t^{n+1} in order to adapt the time step.

Algorithm 1 Adaptive time-stepping algorithm at time t^{n+1}

Given c_n and Δt^n
Solve (4.28)-(4.29) with $\Delta t^{n+1} = \Delta t^n$ to get $c_{h,1}^{n+1}$
Solve (4.34)-(4.35) with $\Delta t^{n+1} = \Delta t^n$ to get $c_{h,2}^{n+1}$
Compute e^{n+1} using (4.36)
if $e^{n+1} > tol$ **then**
    Update Δt^{n+1} using (4.37)
    goto 1
else
    Set $\Delta t^{n+1} = F(e_{n+1}, \Delta t^{n+1})$
end if
Continue to t^{n+2}

Approximately 40 years ago, it was demonstrated that a variable step BDF2 method for ordinary initial-value problems is zero-stable if $\omega^{n+1} < 1 + \sqrt{2}$ [37]. Advancing beyond this classical result has proven to be a challenging task, which has recently gained attention. Through the utilization of techniques involving discrete orthogonal convolution kernels, it has been possible to establish that variable time step BDF2 methods are computationally robust, with $0 < \omega^{n+1} < 3.561$, for linear diffusion models [68], a phase-field crystal model [66], and the molecular beam epitaxial model without slope selection [67]. These techniques have been extended to the Cahn-Hilliard model in [65]. The complexity associated with proving the energy stability of the scheme presented in this

section is significant, to the extent that it could be the subject of a separate research project. Therefore, we will not delve into it in this work.

4.3 Numerical method for the Navier-Stokes-Cahn-Hilliard equations

For the discretization of the variational problem (3.21)–(3.24) we also apply an unfitted finite element method TraceFEM. For convenience, let us briefly revisit the TraceFEM. To discretize surface equations, the TraceFEM relies on a tessellation of a 3D bulk computational domain Ω ($\Gamma \subset \Omega$ holds) into shape regular tetrahedra untangled to the position of Γ.

We start with required definitions to set up finite element spaces and variational form. A few auxiliary results will be proved. Then we proceed to the fully-discrete method by introducing a splitting time discretization, which decouples (3.21)–(3.24) into one linear fluid problem and one phase-field problem per every time step.

On $\mathcal{T}_h^\Gamma$ we use a standard finite element space of continuous functions that are polynomials of degree k on each $T \in \mathcal{T}_h^\Gamma$. This bulk (volumetric) finite element space is denoted by V_h^k:

$$V_h^k = \{v \in C(\Omega_h^\Gamma) \,:\, v \in P_k(T) \text{ for any } T \in \mathcal{T}_h^\Gamma\}.$$

In the trace finite element method formulated below, the traces of functions from V_h^k on Γ are used to approximate the surface fraction and the chemical potential. Our bulk velocity and pressure finite element spaces are either Taylor–Hood elements on Ω_h^Γ,

$$\mathbf{V}_h = (V_h^{m+1})^3, \quad Q_h = V_h^m \cap L_0^2(\Gamma), \tag{4.38}$$

or equal order velocity–pressure elements

$$\mathbf{V}_h = (V_h^m)^3, \quad Q_h = V_h^m \cap L_0^2(\Gamma), \quad m \geq 1. \tag{4.39}$$

These spaces are employed to discretize the surface Navier–Stokes system. Surface velocity and

pressure will be represented by the traces of functions from $\mathbf{V}_h$ and Q_h on Γ. In general, approximation orders k (for the phase-field problem) and m (for the fluid problem) can be chosen to be different.

Assumption 4.1. We assume that integrals over Γ can be computed exactly, i.e., we do not consider geometry errors.

In practice, Γ has to be approximated by a (sufficiently accurate) "discrete" surface $\Gamma_h \approx \Gamma$ in such a way that integrals over Γ_h can be computed accurately and efficiently. For first order finite elements ($m = 1$, $k = 1$), a straightforward polygonal approximation of Γ ensures that the geometric approximation error is consistent with the finite element interpolation error; see, e.g., [84]. For higher order elements, numerical approximation of Γ based on, e.g., isoparametric trace FE can be used to recover the optimal accuracy [36] in a practical situation when parametrization of Γ is not available explicitly.

There are two well-known issues related to the fact that we are dealing with surface and unfitted finite elements:

1. The numerical treatment of condition $\mathbf{u} \cdot \mathbf{n}$. Enforcing the condition $\mathbf{u}_h \cdot \mathbf{n} = 0$ on Γ for polynomial functions $\mathbf{u}_h \in \mathbf{V}_h$ is inconvenient and may lead to locking (i.e., only $\mathbf{u}_h = 0$ satisfies it). Instead, we add a penalty term to the weak formulation to enforce the tangential constraint weakly.

2. Possible small cuts of tetrahedra from $\mathcal{T}_h^\Gamma$ by the surface. For the standard choice of finite element basis functions, this may lead to poorly conditioned algebraic systems. We recover algebraic stability by adding certain volumetric terms to the finite element formulation similar to the finite element formulation (4.4) and (4.13)-(4.15).

To make the presentation of the finite element formulation more compact, we introduce the

following finite element bilinear forms related to the Cahn–Hilliard part of the problem:

$$a_\mu(\mu, v) \coloneqq \int_\Gamma M \nabla_\Gamma \mu \cdot \nabla_\Gamma v \, ds + \tau_\mu \int_{\Omega_h^\Gamma} (\mathbf{n} \cdot \nabla \mu)(\mathbf{n} \cdot \nabla v) \, d\mathbf{x}, \tag{4.40}$$

$$a_c(c, g) \coloneqq \epsilon \int_\Gamma \nabla_\Gamma c \cdot \nabla_\Gamma g \, ds + \tau_c \int_{\Omega_h^\Gamma} (\mathbf{n} \cdot \nabla c)(\mathbf{n} \cdot \nabla g) \, d\mathbf{x}. \tag{4.41}$$

Forms (4.40)–(4.41) are well defined for $\mu, v, c, g \in H^1(\Omega_h^\Gamma)$. The last terms in (4.40) and (4.41) take care of the issue of the small element cuts (the above issue 2), i.e., it holds $\|\mu\|^2_{L^2(\Omega_h^\Gamma)} \leq C a_{\mu,c}(\mu, \mu)$, $\mu \in H^1(\Omega_h^\Gamma)$, with a constant C independent of h and how Γ intersects the mesh, ensuring well-conditioned stiffness matrices [36]. These terms are consistent up to geometric errors related to the approximation of Γ by Γ_h and $\mathbf{n}$ by $\mathbf{n}_h$ in the following sense: any smooth solution μ and c can be extended off the surface along (quasi)-normal directions so that $\mathbf{n} \cdot \nabla \mu = 0$ and $\mathbf{n} \cdot \nabla c = 0$ in Ω_h^Γ. We set the stabilization parameters as follows:

$$\tau_\mu = h, \quad \tau_c = \epsilon \, h^{-1}.$$

This different scaling of parameters with respect to h is required by the analysis. In particular, we will need to control the $L^\infty(\Gamma)$ norm of the finite element approximation of the phase-field parameter, but not the approximation of the chemical potential. This is done in Lemma 4.4, which shows the scaling of the volume normal derivative with a negative power of h.

For the stability of a numerical method, it is crucial that the computed density and viscosity stay positive. The polynomial double-well potential does not enforce c to stay within $[0, 1]$ interval and hence ρ and η may eventually take negative values, if one adopts the linear relation between c and ρ in (3.10) or between c and η in (3.11). Numerical errors may be another reason for the order parameter to depart significantly from $[0, 1]$. Therefore, assuming without loss of generality that $\rho_1 \geq \rho_2$ and $\eta_1 \geq \eta_2$, we first replace (3.10) and (3.11) with the following cut-off functions that

ensure density and viscosity stay positive:

$$\rho(c) = \begin{cases} \rho_2 & c \le 0 \\ c\rho_1 + (1-c)\rho_2 & c > 0 \end{cases} \qquad \eta(c) = \begin{cases} \eta_2 & c \le 0 \\ c\eta_1 + (1-c)\eta_2 & c > 0 \end{cases} \tag{4.42}$$

Note that unlike some previous studies, we clip the linear dependence (3.10) and (3.11) only from below. The resulting convexity of $\rho(c)$ plays a role in the stability analysis later. Nevertheless, (4.42) is not completely satisfactory since $\theta^2 = \frac{\delta\rho}{\delta c}$ is discontinuous, while we need θ to be from C^1. To this end, we approximate $\rho(c)$ from (3.10) by a smooth monotone convex and uniformly positive function. In our implementation we let $\theta^2 = \frac{\rho_1-\rho_2}{2}(\tanh(c/\alpha)+1)$, with $\alpha = 0.1$, and $\rho(c) = \int_0^c \theta^2(t)dt + \rho_2$.

Later we make use of the decomposition of a vector field on Γ into its tangential and normal components: $\mathbf{u} = \overline{\mathbf{u}} + (\mathbf{u}\cdot\mathbf{n})\mathbf{n}$. For the Navier–Stokes part, we introduce the following forms:

$$a(\eta;\mathbf{u},\mathbf{v}) \coloneqq \int_\Gamma 2\eta E_s(\overline{\mathbf{u}}) : E_s(\overline{\mathbf{v}})\, ds + \tau \int_\Gamma (\mathbf{n}\cdot\mathbf{u})(\mathbf{n}\cdot\mathbf{v})\, ds + \beta_u \int_{\Omega_h^\Gamma} [(\mathbf{n}\cdot\nabla)\mathbf{u}]\cdot[(\mathbf{n}\cdot\nabla)\mathbf{v}]\, d\mathbf{x}, \tag{4.43}$$

$$c(\rho;\mathbf{w},\mathbf{u},\mathbf{v}) \coloneqq \int_\Gamma \rho\mathbf{v}^T(\nabla_\Gamma\overline{\mathbf{u}})\mathbf{w}\, ds + \frac{1}{2}\int_\Gamma \widehat{\rho}(\operatorname{div}_\Gamma\overline{\mathbf{w}})\overline{\mathbf{u}}\cdot\overline{\mathbf{v}}\, ds, \tag{4.44}$$

$$b(\mathbf{u},q) = \int_\Gamma \mathbf{u}\cdot\nabla_\Gamma q\, ds, \tag{4.45}$$

$$s(p,q) \coloneqq \beta_p \int_{\Omega_h^\Gamma} (\mathbf{n}\cdot\nabla p)(\mathbf{n}\cdot\nabla q)\, d\mathbf{x}, \tag{4.46}$$

with $\widehat{\rho} = \rho - \frac{d\rho}{dc}c$. Forms (4.43)–(4.46) are well defined for $p, q \in H^1(\Omega_h^\Gamma)\cap H^1(\Gamma)$, $\mathbf{u},\mathbf{v},\mathbf{w} \in H^1(\Omega_h^\Gamma)^3 \cap H^1(\Gamma)^3$. In (4.43), $\tau > 0$ is a penalty parameter to enforce the tangential constraint (i.e., to address the above issue 1), while $\beta_u \ge 0$ in (4.43) and $\beta_p \ge 0$ in (4.46) are stabilization parameters to deal with possible small cuts. They are set according to [52]:

$$\tau = h^{-2}, \quad \beta_p = h, \quad \beta_u = h^{-1}. \tag{4.47}$$

If one uses equal order pressure-velocity trace elements instead of Taylor–Hood elements, then form

(4.46) should be replaced by

$$s(p,q) \coloneqq \beta_p \int_{\Omega_h^\Gamma} \nabla p \cdot \nabla q \, d\mathbf{x}.$$

The second term in (4.44) is consistent since the divergence of the true tangential velocity is zero. To avoid differentiation of the projector operator, one may use the identity $\nabla_\Gamma \overline{\mathbf{u}} = \nabla_\Gamma \mathbf{u} - (\mathbf{u}\cdot\mathbf{n})\mathbf{H}$ to implement the a-form and c-form. For the analysis, we need the identity for the form (4.44) given in the following elementary lemma.

Lemma 4.3. For any $\mathbf{u}, \mathbf{w} \in H^1(\Gamma)^3$, it holds

$$c(\rho; \mathbf{w}, \mathbf{u}, \mathbf{u}) = -\frac{1}{2} \int_\Gamma \theta^2 \, \mathrm{div}_\Gamma(c\overline{\mathbf{w}}) |\overline{\mathbf{u}}|^2 \, ds.$$

Proof. Using the definition of the covariant gradient in terms of tangential operators, $\nabla_\Gamma \overline{\mathbf{u}} = \mathbf{P}(\nabla \overline{\mathbf{u}})\mathbf{P}$, and the integration by parts (2.6), we compute for the first integral term in (4.44)

$$\begin{aligned}
\int_\Gamma \rho \mathbf{u}^T (\nabla_\Gamma \overline{\mathbf{u}}) \mathbf{w} \, ds &= \int_\Gamma \rho \overline{\mathbf{u}}^T (\nabla_\Gamma \overline{\mathbf{u}}) \overline{\mathbf{w}} \, ds = -\int_\Gamma \mathrm{div}_\Gamma(\rho \overline{\mathbf{u}} \otimes \overline{\mathbf{w}}) \cdot \overline{\mathbf{u}} \, ds \\
&= -\int_\Gamma \rho \, \mathrm{div}_\Gamma(\overline{\mathbf{w}}) |\overline{\mathbf{u}}|^2 \, ds - \int_\Gamma \overline{\mathbf{u}} \nabla_\Gamma(\rho \overline{\mathbf{u}}) \overline{\mathbf{w}} \, ds \\
&= -\int_\Gamma \rho \, \mathrm{div}_\Gamma(\overline{\mathbf{w}}) |\overline{\mathbf{u}}|^2 \, ds - \int_\Gamma \rho \mathbf{u}^T (\nabla_\Gamma \overline{\mathbf{u}}) \mathbf{w} \, ds - \int_\Gamma (\overline{\mathbf{w}} \cdot \nabla_\Gamma \rho) |\overline{\mathbf{u}}|^2 \, ds
\end{aligned}$$

From this equality and using $\nabla_\Gamma \rho = \frac{d\rho}{dc} \nabla_\Gamma c$ we obtain:

$$\int_\Gamma \rho \mathbf{u}^T (\nabla_\Gamma \overline{\mathbf{u}}) \mathbf{w} \, ds = -\frac{1}{2} \int_\Gamma \rho \, \mathrm{div}_\Gamma(\overline{\mathbf{w}}) |\overline{\mathbf{u}}|^2 \, ds - \frac{1}{2} \int_\Gamma \frac{d\rho}{d\,c} (\overline{\mathbf{w}} \cdot \nabla_\Gamma c) |\overline{\mathbf{u}}|^2 \, ds \tag{4.48}$$

We recall that $\widehat{\rho} = \rho - \frac{d\rho}{d\,c} c$ and substitute (4.48) into the definition of the form (4.44). After

straightforward computations, we arrive at the result:

$$
\begin{aligned}
c(\rho;\mathbf{w},\mathbf{u},\mathbf{u}) &= \int_\Gamma \rho \mathbf{u}^T(\nabla_\Gamma \overline{\mathbf{u}})\mathbf{w}\, ds + \frac{1}{2}\int_\Gamma (\rho - \frac{d\rho}{d\,c}c)(\,\mathrm{div}_\Gamma \overline{\mathbf{w}})|\overline{\mathbf{u}}|^2\, ds \\
&= -\frac{1}{2}\int_\Gamma \rho\,\mathrm{div}_\Gamma(\overline{\mathbf{w}})|\overline{\mathbf{u}}|^2\, ds - \frac{1}{2}\int_\Gamma \frac{d\rho}{d\,c}(\overline{\mathbf{w}}\cdot\nabla_\Gamma c)|\overline{\mathbf{u}}|^2\, ds + \frac{1}{2}\int_\Gamma (\rho - \frac{d\rho}{d\,c}c)(\,\mathrm{div}_\Gamma \overline{\mathbf{w}})|\overline{\mathbf{u}}|^2\, ds \\
&= -\frac{1}{2}\int_\Gamma \frac{d\rho}{d\,c}(\overline{\mathbf{w}}\cdot\nabla_\Gamma c)|\overline{\mathbf{u}}|^2\, ds - \frac{1}{2}\int_\Gamma \frac{d\rho}{d\,c}c(\,\mathrm{div}_\Gamma \overline{\mathbf{w}})|\overline{\mathbf{u}}|^2\, ds \\
&= -\frac{1}{2}\int_\Gamma \frac{d\rho}{d\,c}\,\mathrm{div}_\Gamma(c\overline{\mathbf{w}})|\overline{\mathbf{u}}|^2\, ds = -\frac{1}{2}\int_\Gamma \theta^2\,\mathrm{div}_\Gamma(c\overline{\mathbf{w}})|\overline{\mathbf{u}}|^2\, ds.
\end{aligned}
$$

□

For the numerical experiments in Chapter 5, we also add to bilinear form (4.43) the grad-div stabilization term [82], $\widehat{\gamma}\int_\Gamma \mathrm{div}_\Gamma \mathbf{u}\,\mathrm{div}_\Gamma \mathbf{v}\, ds$. This term is not essential, in particular for the analysis in Sec. 4.3.2, but we find it beneficial for the performance of the iterative algebraic solver and for the overall accuracy of the solution. We set the grad-div stabilization parameter $\widehat{\gamma} = 1$.

The semi-discrete finite element formulation of (3.21)–(3.24) then reads: Find $c_h(t), \mu_h(t) : (0,T] \to V_h^k$, $\mathbf{u}_h(t) : (0,T] \to \mathbf{V}_h$, $p_h(t) : (0,T] \to Q_h$ satisfying initial conditions solving

$$
\begin{aligned}
(\rho\partial_t \overline{\mathbf{u}}_h, \mathbf{v}_h) + c(\rho;\mathbf{u}_h,\mathbf{u}_h,\mathbf{v}_h) + a(\eta;\mathbf{u}_h,\mathbf{v}_h) + b(\mathbf{v}_h,p_h) &= -(\sigma_\gamma c_h \nabla_\Gamma \mu_h, \mathbf{v}_h) \\
&\quad + M\,(\nabla_\Gamma(\theta\overline{\mathbf{u}}_h)\nabla_\Gamma\mu_h, \theta\mathbf{v}_h) + (\mathbf{f}_h, \mathbf{v}_h), \\
b(\mathbf{u}_h, q_h) - s(p_h, q_h) &= 0, \\
(\partial_t c_h, v_h) - (\mathbf{u}_h c_h, \nabla_\Gamma v_h) + a_\mu(\mu_h, v_h) &= 0, \\
\left(\mu_h - \frac{1}{\epsilon}f_0'(c_h),\, g_h\right) - a_c(c_h, g_h) &= 0,
\end{aligned}
$$

for all $t \in (0,T]$, $(v_h, g_h) \in V_h^k \times V_h^k$, $(\mathbf{v}_h, q_h) \in \mathbf{V}_h \times Q_h$. Next, we are interested in time discretization.

4.3.1 Splitting scheme

At time instance $t^n = n\Delta t$, with time step $\Delta t = \frac{T}{N}$, ζ^n denotes the approximation of generic variable $\zeta(t^n, \mathbf{x})$. Further, we introduce the following notation for a first order approximation of the time derivative:

$$[\zeta]_t^n = \frac{\zeta^n - \zeta^{n-1}}{\Delta t}. \tag{4.49}$$

The decoupled linear finite element method analyzed and tested in this paper reads as follows. At time step t^{n+1}, perform:

- Step 1: Given $\mathbf{u}_h^n \in \mathbf{V}_h$ and $c_h^n \in V_h^k$, find $(c_h^{n+1}, \mu_h^{n+1}) \in V_h^k \times V_h^k$ such that:

$$\left([c_h]_t^{n+1}, v_h\right) - \left(\mathbf{u}_h^n c_h^{n+1}, \nabla_\Gamma v_h\right) + a_\mu(\mu_h^{n+1}, v_h) = 0, \tag{4.50}$$

$$\left(\mu_h^{n+1} - \frac{\gamma_c \Delta t}{\epsilon}[c_h]_t^{n+1} - \frac{1}{\epsilon} f_0'(c_h^n),\, g_h\right) - a_c(c_h^{n+1}, g_h) = 0, \tag{4.51}$$

  for all $(v_h, g_h) \in V_h^k \times V_h^k$.

- Step 2: Set $\theta^{n+1} = \sqrt{\frac{d\rho}{dc}(c_h^{n+1})}$. Find $(\mathbf{u}_h^{n+1}, p_h^{n+1}) \in \mathbf{V}_h \times Q_h$ such that

$$\begin{aligned}
&(\rho^n [\overline{\mathbf{u}}_h]_t^{n+1}, \mathbf{v}_h) + c(\rho^{n+1}; \mathbf{u}_h^n, \mathbf{u}_h^{n+1}, \mathbf{v}_h) + a(\eta^{n+1}; \mathbf{u}_h^{n+1}, \mathbf{v}_h) + b(\mathbf{v}_h, p_h^{n+1}) \\
&\qquad = -(\sigma_\gamma c_h^{n+1} \nabla_\Gamma \mu_h^{n+1}, \mathbf{v}_h) + M\left((\nabla_\Gamma(\theta^{n+1}\overline{\mathbf{u}}_h^{n+1}))\nabla_\Gamma \mu_h^{n+1}, \theta^{n+1}\mathbf{v}_h\right) + (\mathbf{f}_h^{n+1}, \mathbf{v}_h)
\end{aligned} \tag{4.52}$$

$$b(\mathbf{u}_h^{n+1}, q_h) - s(p_h^{n+1}, q_h) = 0 \tag{4.53}$$

  for all $(\mathbf{v}_h, q_h) \in \mathbf{V}_h \times Q_h$.

At each sub-step of the scheme, a linear problem (Cahn–Hilliard type system at step 1 and linearized Navier–Stokes system at step 2) has to be solved. This allows us to achieve low computational costs, while the scheme is provably stable under relatively mild restrictions. Moreover, the results of numerical experiments in Chapter 5 do not show that any restrictions on the discretization parameters are required in practice, Remark 4.6 discusses what arguments in our analysis require

these restrictions. We note that an attractive alternative to treating f_0' explicitly would be the convex–concave splitting [28], which does not require the additional stabilizing term in (4.51).

Before proceeding with analysis, we note that the above scheme does not modify the advection velocity in (4.50) for the purpose of analysis, unlike some other linear decoupled schemes for the NSCH equations found in the literature. We also avoid another common helpful trick to prove energy stability of the variable density NSCH, namely the modification of the momentum equation based on a mass conservation condition of the form $\partial_t \rho + \mathbf{u} \cdot \nabla_\Gamma c - \operatorname{div}_\Gamma (M \nabla_\Gamma \mu) = 0$, which follow from (3.15) and (3.10). This modification, however, is not consistent if a non-linear relation between ρ and c is adopted; also it introduces several extra terms in the finite element formulation.

4.3.2 Analysis of the decoupled finite element method

For the analysis in this section, we assume no forcing term, i.e., $\mathbf{f}^{n+1} = \mathbf{0}$ for all n. To avoid technical complications related to handling Killing vector fields (see, e.g., the discussion in [10] and FE analysis for the surface Navier–Stokes equation in [86]), we shall also assume that the surface does not support any tangential rigid motions, and so $\mathbf{V}_T^0 = \mathbf{V}_T$.

We further use the $a \lesssim b$ notation if inequality $a \leq c\, b$ holds between quantities a and b with a constant c independent of h, Δt, ϵ, and the position of Γ in the background mesh. We give similar meaning to $a \gtrsim b$, and $a \simeq b$ means that both $a \lesssim b$ and $a \gtrsim b$ hold.

The following lemma will be useful in the proof of the main result, which is reported in Theorem 4.5.

Lemma 4.4. There exists $h_0 \simeq 1$ such that for $h \leq h_0$ it holds

$$\|v_h\|_{L^\infty(\Gamma)} \lesssim |\ln h|^{\frac{1}{2}} \|v_h\|_{H^1(\Gamma)} + h^{-\frac{1}{2}} \|\mathbf{n} \cdot \nabla v_h\|_{L^2(\Omega_h^\Gamma)} \qquad \forall\, v_h \in V_h^k. \tag{4.54}$$

For v_h satisfying $\int_\Gamma v_h \, ds = 0$, the factor $\|v_h\|_{H^1(\Gamma)}$ on the r.h.s. can be replaced by $\|\nabla_\Gamma v_h\|_{L^2(\Gamma)}$.

Proof. Denote by $\mathbf{p}(\mathbf{x}) \in \Gamma$, $\mathbf{x} \in \Omega$, the closest point projection on Γ. Since Γ is smooth, there is a

tubular neighborhood of Γ

$$U = \{\mathbf{x} \in \mathbb{R}^3 \,:\, \mathrm{dist}(\mathbf{x}, \Gamma) < d\},$$

with some $d > 0$ depending on smoothness of Γ, such that $\mathbf{x} = \mathbf{p}(\mathbf{x}) + s\mathbf{n}$, $\mathbf{x} \in U$, defines the local coordinate system $(s, \mathbf{y})$, with $\mathbf{y} = \mathbf{p}(\mathbf{x})$ and $|s| = \mathrm{dist}(\mathbf{x}, \Gamma)$. We can always assume $h \le h_0 = O(1)$, such that $\Omega_h^\Gamma \subset U$. For $u \in H^1(U)$, we have in U

$$u(\mathbf{x}) = u(\mathbf{y}) + \int_0^s \mathbf{n} \cdot \nabla u(r, \mathbf{y})\, dr. \tag{4.55}$$

Denote by $\widetilde{\Omega}_h^\Gamma$ a "reachable from Γ" part of Ω_h^Γ in the following sense: for any $\mathbf{x} \in \widetilde{\Omega}_h^\Gamma$ the interval $(\mathbf{x}, \mathbf{p}(\mathbf{x}))$ is completely inside Ω_h^Γ. Let

$$g_\pm(\mathbf{y}) = \pm \sup\{s \in \mathbb{R} \,:\, (\mathbf{y} \pm s\mathbf{n}, \mathbf{y}) \subset \widetilde{\Omega}_h^\Gamma\}, \quad \mathbf{y} \in \Gamma,$$

where $g_\pm(\mathbf{y})$ are piecewise smooth and $\|g_\pm\|_{L^\infty(\Gamma)} \lesssim h$. Thanks to the co-area formula and the smoothness of Γ, it holds

$$\int_{\widetilde{\Omega}_h^\Gamma} |f|\, d\mathbf{x} \simeq \int_\Gamma \int_{g_-}^{g_+} |f|\, d\mathbf{y}\, ds, \quad \text{for any } f \in L^1(\widetilde{\Omega}_h^\Gamma). \tag{4.56}$$

From (4.55) and (4.56), we have:

$$\|u(\mathbf{x})\|_{L^p(\widetilde{\Omega}_h^\Gamma)} \simeq \left(\int_\Gamma \int_{g_-}^{g_+} \left| u(\mathbf{y}) + \int_0^s \mathbf{n} \cdot \nabla u(r, \mathbf{y})\, dr \right|^p ds\, d\mathbf{y} \right)^{\frac{1}{p}},$$

for any real exponent $p \ge 1$. Triangle inequality and inequality:

$$\left(\int_\Gamma \int_{g_-}^{g_+} |u(\mathbf{y})|^p \, ds\, d\mathbf{y} \right)^{\frac{1}{p}} \le |g_+ - g_-|^{\frac{1}{p}} \|u\|_{L^p(\Gamma)}$$

yield

$$\|u\|_{L^p(\widetilde{\Omega}_h^\Gamma)} \lesssim h^{\frac{1}{p}} \|u\|_{L^p(\Gamma)} + \left(\int_\Gamma \int_{g_-}^{g_+} \left| \int_0^s \mathbf{n} \cdot \nabla u(r, \mathbf{y})\, dr \right|^p ds\, d\mathbf{y} \right)^{\frac{1}{p}}. \tag{4.57}$$

To handle the second term on the right-hand side, we apply Hölder's inequality with $p' = p/(p-1)$:

$$\begin{aligned}
\left(\int_\Gamma \int_{g_-}^{g_+} \left| \int_0^s \mathbf{n}\cdot\nabla u(r,\mathbf{y})\, dr \right|^p ds\, d\mathbf{y}\right)^{\frac{1}{p}} &\le \left(\int_\Gamma \int_{g_-}^{g_+} \left| \left(\int_0^s |\mathbf{n}\cdot\nabla u(r,\mathbf{y})|^p\ dr\right)^{\frac{1}{p}} \left(\int_0^s dr\right)^{\frac{1}{p'}} \right|^p ds\, d\mathbf{y}\right)^{\frac{1}{p}} \\
&= \left(\int_\Gamma \int_{g_-}^{g_+} \left(\int_0^s |\mathbf{n}\cdot\nabla u(r,\mathbf{y})|^p\ dr\right) s^{p-1}\, ds\, d\mathbf{y}\right)^{\frac{1}{p}} \\
&\le \left(\int_\Gamma \int_{g_-}^{g_+} |\mathbf{n}\cdot\nabla u(r,\mathbf{y})|^p\ dr\, d\mathbf{y}\right)^{\frac{1}{p}} \left(\int_{g_-}^{g_+} s^{p-1}\, ds\right)^{\frac{1}{p}} \\
&\lesssim h \left\|\mathbf{n}\cdot\nabla u\right\|_{L^p(\widetilde{\Omega}_h^\Gamma)}
\end{aligned}$$

Substituting this in (4.57) and using $\widetilde{\Omega}_h^\Gamma \subset \Omega_h^\Gamma$ we get

$$\|u\|_{L^p(\widetilde{\Omega}_h^\Gamma)} \lesssim h^{\frac{1}{p}} \|u(\mathbf{x})\|_{L^p(\Gamma)} + h \left\|\mathbf{n}\cdot\nabla u\right\|_{L^p(\Omega_h^\Gamma)}. \tag{4.58}$$

Letting $u = u_h \in V_h^k$ and applying FE inverse inequality to treat the last term in (4.58), we arrive at

$$\|u_h\|_{L^p(\widetilde{\Omega}_h^\Gamma))} \lesssim h^{\frac{1}{p}} \|u_h\|_{L^p(\Gamma)} + h^{\frac{3}{p}-\frac{1}{2}} \left\|\mathbf{n}\cdot\nabla u_h\right\|_{L^2(\Omega_h^\Gamma)}. \tag{4.59}$$

Next, we need the following technical result from Lemma 7.9 in [36]: There is $\delta \simeq h$, depending only on the shape regularity of the mesh $\mathcal{T}_h^\Gamma$ such that for any $T \in \mathcal{T}_h^\Gamma$ there exists a ball $B_\delta(T) \subset T \cap \widetilde{\Omega}_h^\Gamma$ of radius δ. Since on every tetrahedron u_h is polynomial function of a fixed degree, by the standard norm equivalence argument, we have

$$\left(\int_T |u_h|^p\, d\mathbf{x}\right)^{\frac{1}{p}} \le C \left(\int_{B_\delta(T)} |u_h|^p\, d\mathbf{x}\right)^{\frac{1}{p}},$$

with C depending only on δ and the shape regularity of T. Raising both parts of this inequality to power p, summing over all $T \in \mathcal{T}_h^\Gamma$, raising both parts to power $1/p$ and using $B_\delta(T) \subset \widetilde{\Omega}_h^\Gamma$, we get

$$\|u_h\|_{L^p(\Omega_h^\Gamma)} \lesssim \|u_h\|_{L^p(\widetilde{\Omega}_h^\Gamma)}.$$

We now use this in (4.59) and apply another FE inverse inequality to get

$$\|u_h\|_{L^\infty(\Gamma)} \leq \|u_h\|_{L^\infty(\Omega_h^\Gamma)} \lesssim h^{-\frac{3}{p}} \|u_h\|_{L^p(\Omega_h^\Gamma)} \lesssim h^{-\frac{2}{p}} \|u_h\|_{L^p(\Gamma)} + h^{-\frac{1}{2}} \|\mathbf{n} \cdot \nabla u_h\|_{L^2(\Omega_h^\Gamma)}. \tag{4.60}$$

For $u \in H^1(\Gamma)$, recall that the Sobolev embedding theorem implies $u \in L^p(\Gamma)$, $p \in [1, \infty)$, and

$$\|u\|_{L^p(\Gamma)} \leq c\, p^{\frac{1}{2}} \|u\|_{H^1(\Gamma)}.$$

This result follows from the corresponding embedding theorem in $\mathbb{R}^2$ by standard arguments based on the surface local parametrization and partition of unity. Using this in (4.60), we obtain the estimate

$$\|u_h\|_{L^\infty(\Gamma)} \lesssim h^{-\frac{2}{p}} p^{\frac{1}{2}} \|u_h\|_{H^1(\Gamma)} + h^{-\frac{1}{2}} \|\mathbf{n} \cdot \nabla u_h\|_{L^2(\Omega_h^\Gamma)}. \tag{4.61}$$

Letting $p = |\ln h|$ proves the result in (4.54). Applying the Poincaré inequality for the function u_h satisfying $\int_\Gamma u_h \, ds = 0$ proves the second claim of the lemma. □

Following [97], we modify the double-well potential in (3.8) for the purpose of analysis so that it is C^2 smooth but has quadratic growth for large $|c|$. Straightforward calculations give us the following expression for $f_0'(c)$ with sufficiently large but fixed $\alpha > 1$:

$$f_0'(c) = \begin{cases} \frac{3\alpha^2-1}{4} c - \left(\frac{\alpha^3}{4} + \frac{3}{8}\alpha^2 - \frac{1}{8} \right), & c > \frac{1+\alpha}{2}, \\ \left(c^2 - \frac{3}{2} c + \frac{1}{2} \right) c, & c \in \left[\frac{1-\alpha}{2}, \frac{1+\alpha}{2} \right], \\ \frac{3\alpha^2-1}{4} c + \left(\frac{\alpha^3}{4} - \frac{3}{8}\alpha^2 + \frac{1}{8} \right), & c < \frac{1-\alpha}{2}. \end{cases}$$

Function $f_0'(x)$ satisfies the following Lipschitz condition with $L = \frac{3\alpha^2-1}{4}$:

$$-\frac{1}{4} \leq \frac{f_0'(x) - f_0'(y)}{x - y} \leq L, \quad \forall x, y \in \mathbb{R},\ x \neq y, \tag{4.62}$$

and growth condition

$$|f_0'(x)| \leq L|x|. \tag{4.63}$$

Theorem 4.5. Assume h and Δt satisfy $\Delta t \leq c|\ln h|^{-1}\epsilon$ and $h \leq c|\ln h|^{-1}\min\{\Delta t, |\ln h|^{-\frac{1}{2}}\epsilon|\Delta t|^{\frac{1}{2}}\}$ for some sufficiently small $c > 0$, independent of h, Δt, ϵ and position of Γ in the background mesh. Then, it holds

$$\int_\Gamma \left(\rho^N|\overline{\mathbf{u}}_h^N|^2 + \frac{\sigma_\gamma}{\epsilon}f_0(c_h^N)\right)ds + a_c(c_h^N, c_h^N) + \sum_{n=1}^{N}\Delta t\left(a(\eta^n; \mathbf{u}_h^n, \mathbf{u}_h^n) + a_\mu(\mu^n, \mu^n) + s_h(p_h^n, p_h^n)\right) \leq K, \tag{4.64}$$

for all $N = 1, 2, \ldots$, with $K = \int_\Gamma \left(\rho^0|\mathbf{u}_h^0|^2 + \frac{\sigma_\gamma}{\epsilon}f_0(c_h^0)\right)ds + a_c(c_h^0, c_h^0)$.

Proof. We use induction on N to prove (4.64). For $N = 0$, the estimate is trivial and provided by the initial condition. For the induction step, assume that it holds with $N = n$.

Letting $v_h = \mu_h^{n+1}$ in (4.50) and $g_h = -[c_h]_t^{n+1}$ in (4.51) and adding the two equations together, we get

$$\begin{aligned}
&-(c_h^{n+1}\mathbf{u}_h^n, \nabla_\Gamma\mu_h^{n+1}) + a_\mu(\mu_h^{n+1}, \mu_h^{n+1}) + \left(\frac{1}{\epsilon}[c_h]_t^{n+1}, f_0'(c_h^n)\right) \\
&\quad + \frac{1}{2\Delta t}\left(a_c(c_h^{n+1}, c_h^{n+1}) - a_c(c_h^n, c_h^n) + |\Delta t|^2 a_c([c_h]_t^{n+1}, [c_h]_t^{n+1})\right) + \frac{\gamma_c\Delta t}{\epsilon}\|[c_h]_t^{n+1}\|^2 = 0.
\end{aligned} \tag{4.65}$$

With the truncated Taylor expansion $f_0(c_h^{n+1}) = f_0(c_h^n) + |\Delta t|[c_h]_t^{n+1} f_0'(c_h^n) + \frac{1}{2}|\Delta t|^2|[c_h]_t^{n+1}|^2 f_0''(\xi^n)$, and (4.62), we get:

$$\begin{aligned}
\left(\frac{1}{\epsilon}[c_h]_t^{n+1}, f_0'(c_h^n)\right) &= \frac{1}{\epsilon}\int_\Gamma \frac{f_0(c_h^{n+1}) - f_0(c_h^n)}{\Delta t}ds - \frac{\Delta t}{2\epsilon}\int_\Gamma |[c_h]_t^{n+1}|^2 f_0''(\xi^n)ds \\
&\geq \frac{1}{\epsilon}\int_\Gamma \frac{f_0(c_h^{n+1}) - f_0(c_h^n)}{\Delta t}ds - \frac{L\Delta t}{2\epsilon}\|[c_h]_t^{n+1}\|^2.
\end{aligned}$$

Since the second term on the right-hand side has a negative sign, we let γ_c be large enough in order

to cancel it with the $\frac{1}{2}$ of the last term on the left-hand side of (4.65). We obtain

$$a_\mu(\mu_h^{n+1},\mu_h^{n+1})+\frac{1}{\epsilon}\int_\Gamma \frac{f_0(c_h^{n+1})-f_0(c_h^n)}{\Delta t}\,ds+\frac{1}{2\Delta t}\left(a_c(c_h^{n+1},c_h^{n+1})-a_c(c_h^n,c_h^n)\right)$$
$$+\Delta t\left(\frac{1}{2}a_c([c_h]_t^{n+1},[c_h]_t^{n+1})+\frac{\gamma_c}{2\epsilon}\|\,[c_h]_t^{n+1}\,\|^2\right)\le (c_h^{n+1}\mathbf{u}_h^n,\nabla_\Gamma\mu_h^{n+1}). \quad (4.66)$$

After re-arranging terms, multiplying by Δt, and dropping some non-negative terms on the left-hand side, we obtain the following inequality

$$\frac{1}{\epsilon}\int_\Gamma f_0(c_h^{n+1})ds+\Delta t a_\mu(\mu_h^{n+1},\mu_h^{n+1})+\frac{1}{2}a_c(c_h^{n+1},c_h^{n+1})+\Delta t^2\frac{\gamma_c}{2\epsilon}\|\,[c_h]_t^{n+1}\,\|^2$$
$$\le\frac{1}{\epsilon}\int_\Gamma f_0(c_h^n)ds+\frac{1}{2}a_c(c_h^n,c_h^n)+\Delta t(c_h^{n+1}\mathbf{u}_h^n,\nabla_\Gamma\mu_h^{n+1}). \quad (4.67)$$

The first two terms on the right-hand side of (4.67) are bounded due to the induction assumption. To handle the third term on the right-hand side, we let $c_0=|\Gamma|^{-1}\int_\Gamma c_h^{n+1}\,ds$ and use Lemma 4.4 that yields $\|c_h^{n+1}-c_0\|_{L^\infty(\Gamma)}\lesssim|\ln h|^{\frac{1}{2}}\epsilon^{-\frac{1}{2}}|a_c(c_h^{n+1},c_h^{n+1})|^{\frac{1}{2}}$ by the definition of the a_c form in (4.41). This, the Cauchy inequality, and the equality $\mathbf{u}_h^n\cdot\nabla_\Gamma\mu_h^{n+1}=\overline{\mathbf{u}}_h^n\cdot\nabla_\Gamma\mu_h^{n+1}$ help us with the following estimate:

$$\begin{aligned}\Delta t|(c_h^{n+1}\mathbf{u}_h^n,\nabla_\Gamma\mu_h^{n+1})|&\le\Delta t|(\,(c_h^{n+1}-c_0)\mathbf{u}_h^n,\nabla_\Gamma\mu_h^{n+1})|+\Delta t|(c_0\mathbf{u}_h^n,\nabla_\Gamma\mu_h^{n+1})|\\&\le\Delta t\|\overline{\mathbf{u}}_h^n\|\|c_h^{n+1}-c_0\|_{L^\infty(\Gamma)}\|\nabla_\Gamma\mu_h^{n+1}\|+\Delta t\|\overline{\mathbf{u}}_h^n\||c_0|\|\nabla_\Gamma\mu_h^{n+1}\|\\&\le\frac{C\Delta t}{\sqrt{\epsilon}}\|\overline{\mathbf{u}}_h^n\||\ln h|^{\frac{1}{2}}|a_c(c_h^{n+1},c_h^{n+1})|^{\frac{1}{2}}\|\nabla_\Gamma\mu_h^{n+1}\|+\Delta t\|\overline{\mathbf{u}}_h^n\||c_0|\|\nabla_\Gamma\mu_h^{n+1}\|\\&\le\Delta t|a_\mu(\mu_h^{n+1},\mu_h^{n+1})|^{\frac{1}{2}}\sqrt{\frac{K}{\rho_2 M}}\left(\frac{C|\ln h|^{\frac{1}{2}}}{\sqrt{\epsilon}}|a_c(c_h^{n+1},c_h^{n+1})|^{\frac{1}{2}}+|c_0|\right).\end{aligned} \quad (4.68)$$

In the last inequality in (4.68), we used the induction assumption to estimate $\|\mathbf{u}_h^n\|$ and the fact that $\rho^n\ge\rho_2$ by definition of the $\rho(c)$ function. Letting $v_h=1$ in (4.50) we have

$$\int_\Gamma[c_h]_t^{n+1}\,ds=0\quad\Rightarrow\quad c_0=|\Gamma|^{-1}\int_\Gamma c_h^0\,ds.$$

We conclude that $|c_0|$ in (4.68) can be bounded by a constant depending only on the initial data. Then, using Young's inequality in (4.68) we get the following bound

$$\Delta t|(\mathbf{u}_h^n \cdot \nabla_\Gamma \mu_h^{n+1}, c_h^{n+1})| \leq \frac{1}{4} a_c(c_h^{n+1}, c_h^{n+1}) + |\Delta t|^2 \frac{C_1 |\ln h|}{\epsilon} a_\mu(\mu_h^{n+1}, \mu_h^{n+1}) + C_2,$$

with some constants C_1, C_2 independent of h, Δt, ϵ, and position of Γ in the background mesh. Using this back in (4.67) with Δt satisfying assumptions of the theorem, and applying (4.64) for $N = n$ for the remainder terms on the right-hand side of (4.67), we get:

$$\frac{1}{\epsilon}\int_\Gamma f_0(c_h^{n+1})ds + \frac{\Delta t}{2} a_\mu(\mu_h^{n+1}, \mu_h^{n+1}) + \frac{1}{4} a_c(c_h^{n+1}, c_h^{n+1}) + \frac{\Delta t^2 \gamma_c}{2\epsilon} \| [c_h]_t^{n+1} \|^2 \leq C, \tag{4.69}$$

with some $C > 0$ independent of h, Δt, ϵ and the position of Γ in the mesh. We need this bound later in the proof.

Let $\mathbf{v}_h = \mathbf{u}_h^{n+1}$ in (4.52) and $q_h = -p_h^{n+1}$ in (4.53), and add the two equations together. We also apply Lemma 4.3 to handle the c-form. This brings us to the following equality:

$$\begin{aligned}
&\frac{1}{2\Delta t}\left(\|(\rho^n)^{\frac{1}{2}} \overline{\mathbf{u}}_h^{n+1}\|^2 - \|(\rho^n)^{\frac{1}{2}} \overline{\mathbf{u}}_h^{n}\|^2 + |\Delta t|^2 \|(\rho^n)^{\frac{1}{2}} [\overline{\mathbf{u}}_h]_t^{n+1} \|^2 \right) \\
&\quad - \frac{1}{2}\int_\Gamma |\theta^{n+1}|^2 \operatorname{div}_\Gamma(c_h^{n+1} \overline{\mathbf{u}}_h^n) |\overline{\mathbf{u}}_h^{n+1}|^2 \, ds + a(\eta^{n+1}; \mathbf{u}_h^{n+1}, \mathbf{u}_h^{n+1}) + s(p_h^{n+1}, p_h^{n+1}) \\
&\quad = -(\sigma_\gamma c_h^{n+1} \nabla_\Gamma \mu_h^{n+1}, \mathbf{u}_h^{n+1}) + M\left((\nabla_\Gamma(\theta^{n+1} \overline{\mathbf{u}}_h^{n+1})) \nabla_\Gamma \mu_h^{n+1}, \theta^{n+1} \mathbf{u}_h^{n+1} \right).
\end{aligned}$$

By adding $\pm \frac{1}{2\Delta t} \|(\rho^{n+1})^{\frac{1}{2}} \overline{\mathbf{u}}_h^{n+1}\|^2$ and re-arranging terms, we get

$$\begin{aligned}
&\frac{1}{2\Delta t}\left(\|(\rho^{n+1})^{\frac{1}{2}} \overline{\mathbf{u}}_h^{n+1}\|^2 - \|(\rho^n)^{\frac{1}{2}} \overline{\mathbf{u}}_h^{n}\|^2 + |\Delta t|^2 \|(\rho^n)^{\frac{1}{2}} [\overline{\mathbf{u}}_h]_t^{n+1} \|^2 \right) \\
&\quad - \frac{1}{2}\int_\Gamma \frac{\rho^{n+1} - \rho^n}{\Delta t} |\overline{\mathbf{u}}_h^{n+1}|^2 \, ds - \frac{1}{2}\int_\Gamma |\theta^{n+1}|^2 \operatorname{div}_\Gamma(c_h^{n+1} \overline{\mathbf{u}}_h^n) |\overline{\mathbf{u}}_h^{n+1}|^2 \, ds \\
&\quad + a(\eta^{n+1}; \mathbf{u}_h^{n+1}, \mathbf{u}_h^{n+1}) + s(p_h^{n+1}, p_h^{n+1}) \\
&\quad = -(\sigma_\gamma c_h^{n+1} \nabla_\Gamma \mu_h^{n+1}, \mathbf{u}_h^{n+1}) + M\left((\nabla_\Gamma(\theta^{n+1} \overline{\mathbf{u}}_h^{n+1})) \nabla_\Gamma \mu_h^{n+1}, \theta^{n+1} \mathbf{u}_h^{n+1} \right).
\end{aligned} \tag{4.70}$$

Denote by $\mathcal{P}_h : H^1(\Gamma) \to V_h^k$ an H^1-type projection into V_h^k given by the a_μ bilinear form:

$$a_\mu(\mathcal{P}_h(u), v_h) = M\left(\nabla_\Gamma u, \nabla_\Gamma v_h\right) \quad \forall\, v_h \in V_h^k.$$

By standard analysis of the TraceFEM for the Laplace-Beltrami problem, e.g. [89], we have

$$\|u - \mathcal{P}_h(u)\| \lesssim h\|\nabla_\Gamma u\|. \tag{4.71}$$

Since ρ is a convex function of c and $\frac{d\rho}{dc} \geq 0$, we have

$$\rho^{n+1} - \rho^n \leq \frac{d\rho}{dc}\Big|_{c_h^{n+1}}(c_h^{n+1} - c_h^n) = |\theta^{n+1}|^2(c_h^{n+1} - c_h^n). \tag{4.72}$$

Using (4.72) and eq. (4.50) with $v_h = \mathcal{P}_h\left(|\theta^{n+1}\overline{\mathbf{u}}_h^{n+1}|^2\right)$, for the terms on the second line of (4.70) we obtain

$$\begin{aligned}
&\int_\Gamma \frac{\rho^{n+1} - \rho^n}{\Delta t}|\overline{\mathbf{u}}_h^{n+1}|^2 + |\theta^{n+1}|^2\,\mathrm{div}_\Gamma(c_h^{n+1}\overline{\mathbf{u}}_h^n)|\overline{\mathbf{u}}_h^{n+1}|^2\,ds \\
&\quad\leq \int_\Gamma \left(\frac{c^{n+1} - c^n}{\Delta t} + \mathrm{div}_\Gamma(c_h^{n+1}\overline{\mathbf{u}}_h^n)\right)|\theta^{n+1}\overline{\mathbf{u}}_h^{n+1}|^2\,ds \\
&\quad= -\int_\Gamma M\nabla_\Gamma\mu_h^{n+1}\cdot\nabla_\Gamma|\theta^{n+1}\overline{\mathbf{u}}_h^{n+1}|^2\,ds + I(e_h),
\end{aligned} \tag{4.73}$$

with

$$I(e_h) = \int_\Gamma \left(\frac{c_h^{n+1} - c_h^n}{\Delta t} + \mathrm{div}_\Gamma(c_h^{n+1}\overline{\mathbf{u}}_h^n)\right)e_h\,ds, \quad e_h \coloneqq |\theta^{n+1}\overline{\mathbf{u}}_h^{n+1}|^2 - \mathcal{P}_h\left(|\theta^{n+1}\overline{\mathbf{u}}_h^{n+1}|^2\right).$$

Next, we use (4.73) to simplify (4.70) as follows:

$$\begin{aligned}
&\frac{1}{2\Delta t}\left(\|(\rho^{n+1})^{\frac{1}{2}}\overline{\mathbf{u}}_h^{n+1}\|^2 - \|(\rho^n)^{\frac{1}{2}}\overline{\mathbf{u}}_h^n\|^2 + |\Delta t|^2\|(\rho^n)^{\frac{1}{2}}\,[\overline{\mathbf{u}}_h]_t^{n+1}\,\|^2\right) \\
&\qquad + a(\eta^{n+1}; \mathbf{u}_h^{n+1}, \mathbf{u}_h^{n+1}) + s(p_h^{n+1}, p_h^{n+1}) \leq -(\sigma_\gamma c_h^{n+1}\nabla_\Gamma\mu_h^{n+1}, \mathbf{u}_h^{n+1}) + I(e_h).
\end{aligned} \tag{4.74}$$

After adding (4.66) multiplied by σ_γ to (4.74) and dropping some non-negative terms on the left-hand side, we arrive at

$$\begin{aligned}
&\frac{1}{2\Delta t}\Big(\|(\rho^{n+1})^{\frac{1}{2}}\overline{\mathbf{u}}_h^{n+1}\|^2-\|(\rho^n)^{\frac{1}{2}}\overline{\mathbf{u}}_h^n\|^2+|\Delta t|^2\|(\rho^n)^{\frac{1}{2}}\,[\overline{\mathbf{u}}_h]_t^{n+1}\,\|^2\\
&\quad+\sigma_\gamma(a(c_h^{n+1},c_h^{n+1})-a(c_h^n,c_h^n))+\frac{2\sigma_\gamma}{\epsilon}\int_\Gamma(f_0(c_h^{n+1})-f_0(c_h^n))ds\Big)+s_h(p_h^{n+1},p_h^{n+1})\\
&\quad+a(\eta^{n+1};\mathbf{u}_h^{n+1},\mathbf{u}_h^{n+1})+\sigma_\gamma a_\mu(\mu_h^{n+1},\mu_h^{n+1})\\
&\quad\le-\Delta t(\sigma_\gamma c_h^{n+1}\nabla_\Gamma\mu_h^{n+1},[\mathbf{u}_h]_t^{n+1})+I(e_h).
\end{aligned}\tag{4.75}$$

It remains to estimate the terms on the right-hand side of (4.75). We handle the first term by invoking the result of Lemma 4.4 as follows:

$$\begin{aligned}
\Delta t|(\sigma_\gamma c_h^{n+1}\nabla_\Gamma\mu_h^{n+1},[\mathbf{u}_h]_t^{n+1})|&\le\sigma_\gamma\Delta t|((c_h^{n+1}-c_0)\nabla_\Gamma\mu_h^{n+1},[\mathbf{u}_h]_t^{n+1})|+\sigma_\gamma\Delta t|(c_0\nabla_\Gamma\mu_h^{n+1},[\mathbf{u}_h]_t^{n+1})|\\
&\le\sigma_\gamma\Delta t\|c_h^{n+1}-c_0\|_{L^\infty(\Gamma)}\|\nabla_\Gamma\mu_h^{n+1}\|\|\,[\overline{\mathbf{u}}_h]_t^{n+1}\,\|+\sigma_\gamma\Delta t|c_0|\|\nabla_\Gamma\mu_h^{n+1}\|\|\,[\overline{\mathbf{u}}_h]_t^{n+1}\,\|\\
&\le\frac{C}{\rho_2^{\frac{1}{2}}\epsilon^{\frac{1}{2}}}|\ln h|^{\frac{1}{2}}\sigma_\gamma\Delta t|a_c(c_h^{n+1},c_h^{n+1})|^{\frac{1}{2}}\|\nabla_\Gamma\mu_h^{n+1}\|\|(\rho^n)^{\frac{1}{2}}\,[\overline{\mathbf{u}}_h]_t^{n+1}\,\|\\
&\quad+\frac{\sigma_\gamma\Delta t}{\rho_2^{\frac{1}{2}}}|c_0|\|\nabla_\Gamma\mu_h^{n+1}\|\|(\rho^n)^{\frac{1}{2}}\,[\overline{\mathbf{u}}_h]_t^{n+1}\,\|.
\end{aligned}\tag{4.76}$$

Thanks to the a priori bound $a_c(c_h^{n+1},c_h^{n+1})\le C$ from (4.69), estimate (4.76) yields

$$\Delta t|(\sigma_\gamma c_h^{n+1}\nabla_\Gamma\mu_h^{n+1},[\mathbf{u}_h]_t^{n+1})|\le C\sigma_\gamma\Delta t(\epsilon^{-\frac{1}{2}}|\ln h|^{\frac{1}{2}}+1)\|(\rho^n)^{\frac{1}{2}}\,[\overline{\mathbf{u}}_h]_t^{n+1}\,\||a_\mu(\mu_h^{n+1},\mu_h^{n+1})|^{\frac{1}{2}}.\tag{4.77}$$

With the help of $\Delta t\le C|\ln h|^{-1}\epsilon$ for sufficiently small C and $\epsilon\lesssim 1$ we obtain

$$\begin{aligned}
\Delta t|(\sigma_\gamma c_h^{n+1}\nabla_\Gamma\mu_h^{n+1},[\mathbf{u}_h]_t^{n+1})|&\le\frac{\Delta t}{2}\|(\rho^n)^{\frac{1}{2}}\,[\overline{\mathbf{u}}_h]_t^{n+1}\,\|^2+C\sigma_\gamma\Delta t(\epsilon^{-\frac{1}{2}}|\ln h|^{\frac{1}{2}}+1)^2a_\mu(\mu_h^{n+1},\mu_h^{n+1})\\
&\le\frac{\Delta t}{2}\|(\rho^n)^{\frac{1}{2}}\,[\overline{\mathbf{u}}_h]_t^{n+1}\,\|^2+\frac{1}{2}\sigma_\gamma a_\mu(\mu_h^{n+1},\mu_h^{n+1}).
\end{aligned}\tag{4.78}$$

Now, we proceed with the terms in $I_h(e_h)$. For the first terms in $I_h(e_h)$, the Cauchy-Schwarz

inequality and estimate (4.71) for the $L^2(\Gamma)$ norm of e_h gives:

$$\int_\Gamma \left(\frac{c_h^{n+1} - c_h^n}{\Delta t} \right) e_h \, ds \leq \| \, [c_h]_t^{n+1} \, \| \| e_h \| \lesssim h \| \, [c_h]_t^{n+1} \, \| \| \nabla_\Gamma (|\theta^{n+1} \overline{\mathbf{u}}_h^{n+1}|^2) \|. \tag{4.79}$$

To estimate the right-most factor, we need the inequalities

$$\|\overline{\mathbf{u}}_h^{n+1}\|_{L^\infty(\Gamma)}^2 \lesssim |\ln h| \|\overline{\mathbf{u}}_h^{n+1}\|_{H^1(\Gamma)}^2 + h^{-1} \|\mathbf{n} \cdot \nabla |\overline{\mathbf{u}}_h^{n+1}\|_{L^2(\Omega_h^\Gamma)}^2 \lesssim |\ln h| a(\eta^{n+1}, \mathbf{u}_h^{n+1}, \mathbf{u}_h^{n+1}),$$

which follow by applying Lemma 4.4 componentwise and then using the Korn inequality (3.20) and the fact that η^{n+1} is uniformly bounded from below (see the definition in (4.42)). Thanks to $0 \leq \theta^2 \lesssim 1$ and $0 \leq \frac{d\theta^2}{dc} = \frac{d^2\rho}{dc^2} \lesssim 1$, we have

$$\begin{aligned}
\|\nabla_\Gamma (|\theta^{n+1} \overline{\mathbf{u}}_h^{n+1}|^2)\| &\lesssim \| |\overline{\mathbf{u}}_h^{n+1}|^2 \nabla_\Gamma c_h^{n+1} \| + \| \nabla_\Gamma |\overline{\mathbf{u}}_h^{n+1}|^2 \| \\
&\lesssim \|\overline{\mathbf{u}}_h^{n+1}\|_{L^\infty(\Gamma)}^2 \|\nabla_\Gamma c_h^{n+1}\| + \|\overline{\mathbf{u}}_h^{n+1}\|_{L^\infty(\Gamma)} \|\nabla_\Gamma \overline{\mathbf{u}}_h^{n+1}\| \\
&\lesssim |\ln h| a(\eta^{n+1}, \mathbf{u}_h^{n+1}, \mathbf{u}_h^{n+1}) \|\nabla_\Gamma c_h^{n+1}\| + |\ln h|^{\frac{1}{2}} a(\eta^{n+1}, \mathbf{u}_h^{n+1}, \mathbf{u}_h^{n+1}) \\
&\lesssim (|\ln h| \epsilon^{-\frac{1}{2}} + |\ln h|^{\frac{1}{2}}) a(\eta^{n+1}, \mathbf{u}_h^{n+1}, \mathbf{u}_h^{n+1}) \\
&\lesssim |\ln h| \epsilon^{-\frac{1}{2}} a(\eta^{n+1}, \mathbf{u}_h^{n+1}, \mathbf{u}_h^{n+1}).
\end{aligned}$$

Using this together with the a priori bound for $\| \, [c_h]_t^{n+1} \, \|$ from (4.69) in (4.79) and using the assumption $h \leq c |\ln h|^{-1} \Delta t$ for sufficiently small c, we have

$$\int_\Gamma \left(\frac{c_h^{n+1} - c_h^n}{\Delta t} \right) e_h \, ds \leq c \, h |\ln h| \Delta t^{-1} a(\eta^{n+1}, \mathbf{u}_h^{n+1}, \mathbf{u}_h^{n+1}) \leq \frac{1}{4} a(\eta^{n+1}, \mathbf{u}_h^{n+1}, \mathbf{u}_h^{n+1}). \tag{4.80}$$

Next, we treat the second term in $I(e_h)$. Using Cauchy–Schwarz inequality and estimating $\|e_h\|$ as above we have

$$\int_\Gamma \operatorname{div}_\Gamma (c_h^{n+1} \overline{\mathbf{u}}_h^n) e_h \, ds \lesssim h |\ln h| \epsilon^{-\frac{1}{2}} \| \operatorname{div}_\Gamma (c_h^{n+1} \overline{\mathbf{u}}_h^n) \| a(\eta^{n+1}, \mathbf{u}_h^{n+1}, \mathbf{u}_h^{n+1}). \tag{4.81}$$

By the triangle inequality

$$\|\operatorname{div}_\Gamma(c_h^{n+1}\overline{\mathbf{u}}_h^n)\| \le \|c_h^{n+1}\operatorname{div}_\Gamma(\overline{\mathbf{u}}_h^n)\| + \|\mathbf{u}_h^n\cdot\nabla_\Gamma c_h^{n+1}\|.$$

Each term on the right hand side can be treated individually by invoking Lemma 4.4, a priori bound from (4.69), and induction assumption:

$$\begin{aligned}\|c_h^{n+1}\operatorname{div}_\Gamma(\overline{\mathbf{u}}_h^n)\| &\le \|c_h^{n+1}\|_{L^\infty(\Gamma)}\|\operatorname{div}_\Gamma(\overline{\mathbf{u}}_h^n)\|\\ &\lesssim |\ln h|^{\frac12}\|c_h^{n+1}\|_{H^1(\Gamma)}\|\operatorname{div}_\Gamma(\overline{\mathbf{u}}_h^n)\|\\ &\lesssim |\ln h|^{\frac12}\epsilon^{-\frac12}\|\operatorname{div}_\Gamma(\overline{\mathbf{u}}_h^n)\| \lesssim |\ln h|^{\frac12}\epsilon^{-\frac12}|a(\eta^n,\mathbf{u}_h^n,\mathbf{u}_h^n)|^{\frac12} \lesssim |\ln h|^{\frac12}\epsilon^{-\frac12}|\Delta t|^{-\frac12}.\end{aligned}$$

and

$$\begin{aligned}\|\mathbf{u}_h^n\cdot\nabla_\Gamma c_h^{n+1}\| &\le \|\overline{\mathbf{u}}_h^n\|_{L^\infty(\Gamma)}\|\nabla_\Gamma c_h^{n+1}\|\\ &\lesssim \epsilon^{-\frac12}\|\overline{\mathbf{u}}_h^n\|_{L^\infty(\Gamma)} \lesssim \epsilon^{-\frac12}|\ln h|^{\frac12}\|\overline{\mathbf{u}}_h^n\|_{H^1(\Gamma)}\\ &\lesssim \epsilon^{-\frac12}|\ln h|^{\frac12}|a(\eta^n,\mathbf{u}_h^n,\mathbf{u}_h^n)|^{\frac12} \lesssim |\ln h|^{\frac12}\epsilon^{-\frac12}|\Delta t|^{-\frac12}.\end{aligned}$$

Using these estimates back into (4.81) and with the assumption $h \le c|\ln h|^{-\frac32}\epsilon|\Delta t|^{-\frac12}$ for sufficiently small c, we arrive at the estimate

$$|I(e_h)| \le \frac12 a(\eta^{n+1};\mathbf{u}_h^{n+1},\mathbf{u}_h^{n+1}). \tag{4.82}$$

Finally, we substitute (4.78) and (4.82) in (4.75) to obtain

$$\begin{aligned}&\frac{1}{2\Delta t}\left(\|(\rho^{n+1})^{\frac12}\overline{\mathbf{u}}_h^{n+1}\|^2 + \sigma_\gamma a(c_h^{n+1},c_h^{n+1}) + \frac{2\sigma_\gamma}{\epsilon}\int_\Gamma f_0(c_h^{n+1})ds\right) + \frac12 a(\eta^{n+1};\mathbf{u}_h^{n+1},\mathbf{u}_h^{n+1})\\ &+ \frac12\sigma_\gamma a_\mu(\mu_h^{n+1},\mu_h^{n+1}) + s_h(p_h^{n+1},p_h^{n+1}) \le \frac{1}{2\Delta t}\left(\|(\rho^n)^{\frac12}\overline{\mathbf{u}}_h^n\|^2 + \sigma_\gamma a(c_h^n,c_h^n) + \frac{2\sigma_\gamma}{\epsilon}\int_\Gamma f_0(c_h^n)ds\right).\end{aligned}$$

This completes the induction step. □

Remark 4.6. From the proof, we see that the assumption $h \leq c|\ln h|^{-1}\min\{\Delta t, |\ln h|^{-\frac{1}{2}}\epsilon|\Delta t|^{\frac{1}{2}}\}$ results from the fact that at the discrete level we cannot test the transport equation for the order parameter with $v_h = |\mathbf{u}_h^{n+1}|^2$, and so we have to project $|\mathbf{u}_h^{n+1}|^2$ (or $|\overline{\mathbf{u}}_h^{n+1}|^2$ for surfaces) in the finite element space V_h^k and handle the resulting inconsistency. If the finite element velocity space is such that $|\mathbf{v}_h|^2 \in V_h^k$ for $\mathbf{v}_h \in \mathbf{V}_h$, then the upper bound on h is not needed in the analysis (in the surface case we still would need to handle $|\mathbf{u}_h^{n+1}|^2 - |\overline{\mathbf{u}}_h^{n+1}|^2$, but this is possible due to the control over $\|\mathbf{n}\cdot\mathbf{u}_h^{n+1}\|^2$ that we have thanks to penalty term in the TraceFEM formulation). An example, when $|\mathbf{v}_h|^2 \in V_h^k$ holds, is $\mathbf{P_1}$–P_1 stabilized velocity–pressure element combined with P_2 element for the order parameter and chemical potential.

In the numerical experiments however, we observed only a restriction of the form $h \lesssim \epsilon$, which is very typical for a phase field approach. We hypothesize that our analysis may not be sharp with respect to the assumption on h in the theorem statement. We also note that the failure of mesh to resolve the interface, i.e., $h \geq \epsilon$, led to inaccurate FE solutions rather than a blow-up in time.

5 Numerical experiments

5.1 Numerical experiments with the Cahn–Hilliard model

After validating the accuracy of the numerical methods presented in Sec. 4.2.2, we compare the numerical results obtained with our SAV methods against the results obtained with a stabilized scheme inspired from [97] and presented in [115]. We will start by comparing the numerical results produced by the different methods on a sphere in Sec. 5.1.2. Then, in Sec. 5.1.3 we will present results on a more complex surface that represents an idealized cell.

For the implementation of the methods in Sec. 4.2.1 and 4.2.3, we use open source Finite Element package DROPS [23].

5.1.1 Convergence test

To assess our implementation of the SAV schemes presented in Sec. 4.2.2, we consider the following exact solution to the non-homogeneous surface Cahn–Hilliard equations on the unit sphere, centered at the origin:

$$c^*(t, \mathbf{x}) = \frac{1}{2}\left(1 + \tanh \frac{x_3}{2\sqrt{2}\epsilon}\right), \quad t \in [0, 1]. \tag{5.1}$$

Here, $\mathbf{x} = (x_1, x_2, x_3)^T$ denotes a point in $\mathbb{R}^3$. The exact chemical potential μ^* can be readily computed from eq. (3.6) using the free energy per unit surface in (3.8) and the above c^*. The non-zero forcing term is computed by plugging c^* and μ^* into (3.5). We set $\rho = 1$ and mobility M as in (3.7). In (4.7), we take $C = 1$. Since it is known that smaller values ϵ are numerically challenging (see, e.g., [30, 97]), we consider decreasing values of ϵ: $\epsilon = 1, 0.1, 0.05$.

We characterize the surface Γ as the zero level set of function $\phi(\mathbf{x}) = \|\mathbf{x}\|_2 - 1$, and embed Γ in an outer cubic domain $\Omega = [-5/3, 5/3]^3$. The initial triangulation $\mathcal{T}_{h_\ell}$ of Ω consists of 8 sub-cubes, where each of the sub-cubes is further subdivided into 6 tetrahedra. Further, the mesh is refined towards the surface, and $\ell \in \mathbb{N}$ denotes the level of refinement, with the associated mesh

size $h_\ell = \frac{10/3}{2^{\ell+1}}$. Fig. 1 shows the approximation of (5.1) with $\epsilon = 0.05$ computed with mesh level $\ell = 6$ and a magnified view of the interface thickness with the bulk mesh near the surface. The time step is also refined with the mesh as specified below. Time step adaptivity is not used for this test.

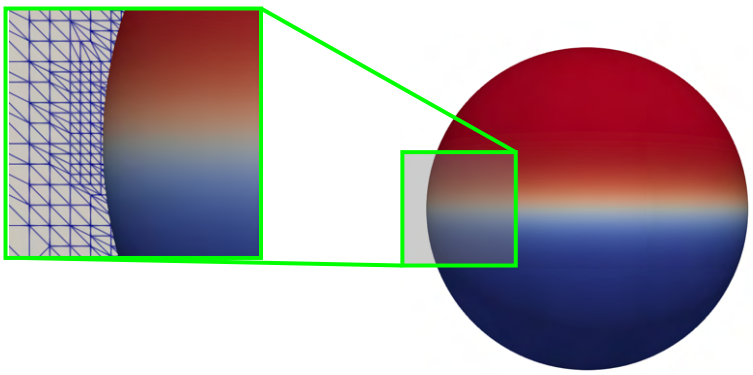

Figure 1: Approximation of exact solution (5.1) with $\epsilon = 0.05$ computed with mesh level $\ell = 6$ and a magnified view of the interface thickness with the bulk mesh near the surface.

Fig. 2 shows the evolution of the L_2 errors of c computed with the SAV-BDF1 and SAV-BDF2 methods for $\epsilon = 0.05, 0.1, 1$. We used $\mathbb{P}^1$ elements and for each panel in Fig. 2 we report the L_2 errors associated to four mesh refinement levels. We see that in all the cases the errors increase slightly at the beginning of the time interval and then they tend to reach a plateau. The thinner the interface between phases is (i.e., the smaller ϵ), the faster the plateau is reached. In the case of the smallest ϵ, i.e., $\epsilon = 0.05$, Fig. 3 displays the evolution of modified energy (4.16), which is associated to the SAV-BDF1 method, and modified energy (4.24), which is associated to the SAV-BDF2 method, for mesh level $\ell = 5$. As expected, the modified energies decay in time. Note that SAV-BDF1 modified energy approximates $E(c)$ from (4.5), while the SAV-BDF2 modified energy approximates $2E(c)$.

Tables 1 and 2 report the L_2 errors of c at the end of the time interval (i.e., $t = 1$) computed with the SAV-BDF1 and SAV-BDF2 method, respectively. Mesh refinement level and associated time steps are reported in the tables, which provide the order of convergence too. We see that while the L_2 errors are somewhat different, the order of convergence is the same. It is around 2, especially

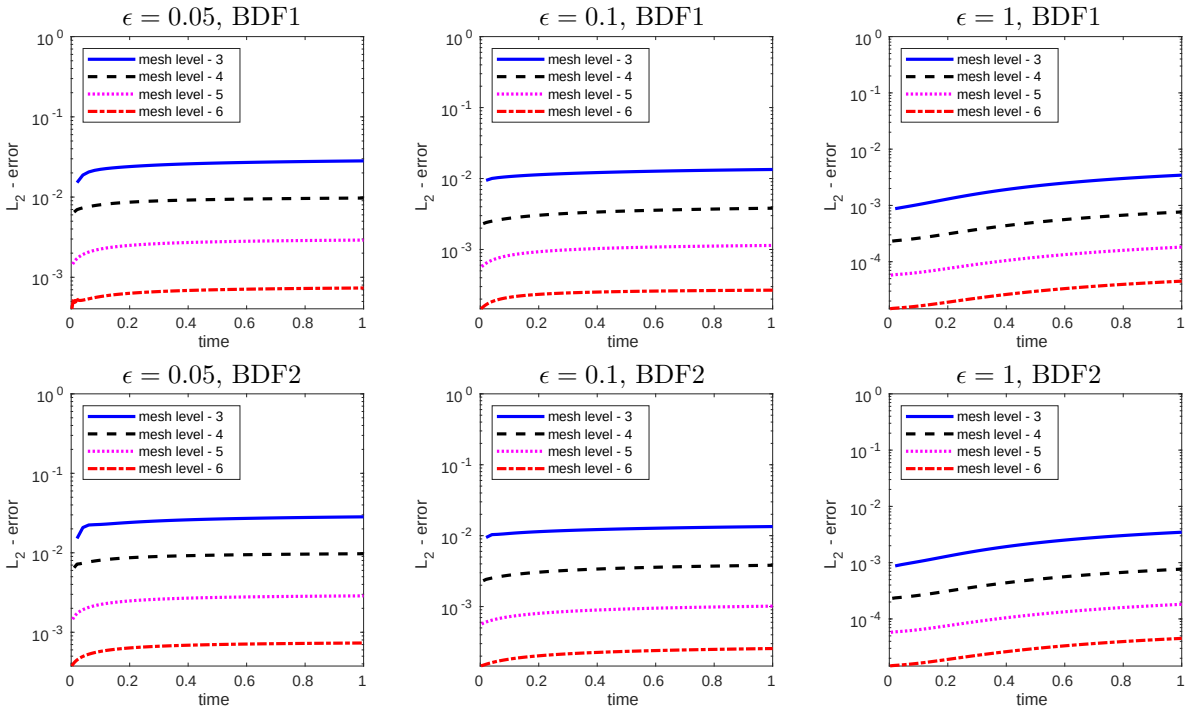

Figure 2: Convergence test: evolution of the L_2 errors of c computed with the SAV-BDF1 method (top row) or SAV-BDF2 method (bottom row) for $\epsilon = 0.05$ (left), $\epsilon = 0.1$ (center), and $\epsilon = 1$ (right).

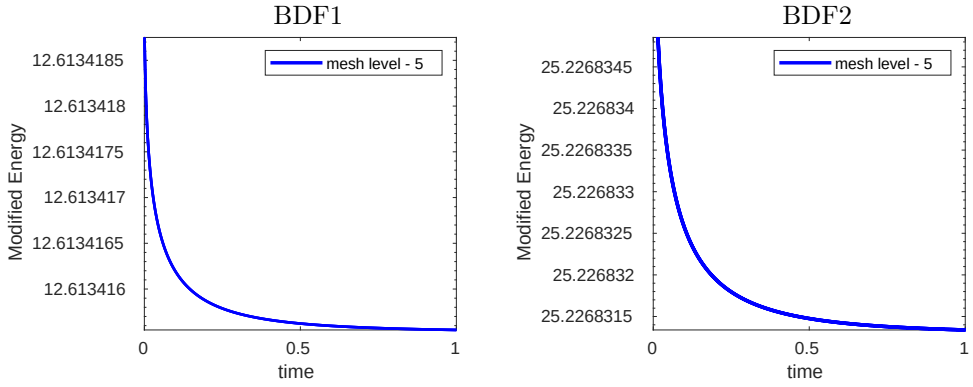

Figure 3: Convergence test, $\epsilon = 0.05$: decay of modified energy (4.16) (left) and (4.24) (right) for mesh level $\ell = 5$.

when going from $\ell = 5$ to $\ell = 6$, which is the optimal order of convergence for $\mathbb{P}^1$ elements. We believe that the order of convergence is not spoiled when using BDF1 for time discretization because the time step value is small enough to prevent the time discretization error from dominating over the space discretization error. Table 2 can be compared with Table 3, which provides L_2 errors

of c at $t = 1$ computed with the stabilized method in [115] and BDF2, together with the rates of convergence. Not just the convergence rates are the same, but the errors are also very similar. We have highlighted in red the digits in Table 3 that differ from Table 2.

Table 1: Convergence test, $\epsilon = 0.05, 0.1, 1$: L_2 errors of c at $t = 1$ computed with the SAV-BDF1 method and $\mathbb{P}^1$ elements for different meshes and time steps, together with the rates of convergence

		$\epsilon = 0.05$		$\epsilon = 0.1$		$\epsilon = 1$	
mesh level	Δt	error	rate	error	rate	error	rate
3	0.02	$2.8247 \cdot 10^{-2}$		$1.3409 \cdot 10^{-2}$		$0.3453 \cdot 10^{-2}$	
4	0.01	$0.9720 \cdot 10^{-2}$	1.54	$0.3816 \cdot 10^{-2}$	1.81	$0.0765 \cdot 10^{-2}$	2.18
5	0.005	$0.2909 \cdot 10^{-2}$	1.76	$0.1139 \cdot 10^{-2}$	1.91	$0.0181 \cdot 10^{-2}$	2.07
6	0.0025	$0.0735 \cdot 10^{-2}$	1.96	$0.0267 \cdot 10^{-2}$	1.98	$0.0045 \cdot 10^{-2}$	2.01

Table 2: Convergence test, $\epsilon = 0.05, 0.1, 1$: L_2 errors of c at $t = 1$ computed with the SAV-BDF2 method and $\mathbb{P}^1$ elements for different meshes and time steps, together with the rates of convergence

		$\epsilon = 0.05$		$\epsilon = 0.1$		$\epsilon = 1$	
mesh level	Δt	error	rate	error	rate	error	rate
3	0.02	$2.8338 \cdot 10^{-2}$		$1.3438 \cdot 10^{-2}$		$0.3474 \cdot 10^{-2}$	
4	0.01	$0.9727 \cdot 10^{-2}$	1.54	$0.3824 \cdot 10^{-2}$	1.81	$0.0767 \cdot 10^{-2}$	2.18
5	0.005	$0.2869 \cdot 10^{-2}$	1.76	$0.1013 \cdot 10^{-2}$	1.91	$0.0181 \cdot 10^{-2}$	2.07
6	0.0025	$0.0732 \cdot 10^{-2}$	1.96	$0.0255 \cdot 10^{-2}$	1.98	$0.0045 \cdot 10^{-2}$	2.01

Table 3: Convergence test, $\epsilon = 0.05, 0.1, 1$: L_2 errors of c at $t = 1$ computed with the stabilized method in [115], $\mathbb{P}^1$ elements, and BDF2 for different meshes and time steps, together with the rates of convergence

		$\epsilon = 0.05$		$\epsilon = 0.1$		$\epsilon = 1$	
mesh level	Δt	error	rate	error	rate	error	rate
3	0.02	$2.8335 \cdot 10^{-2}$		$1.3434 \cdot 10^{-2}$		$0.3475 \cdot 10^{-2}$	
4	0.01	$0.9725 \cdot 10^{-2}$	1.54	$0.3823 \cdot 10^{-2}$	1.81	$0.0767 \cdot 10^{-2}$	2.18
5	0.005	$0.2869 \cdot 10^{-2}$	1.76	$0.1013 \cdot 10^{-2}$	1.91	$0.0182 \cdot 10^{-2}$	2.07
6	0.0025	$0.0732 \cdot 10^{-2}$	1.96	$0.0255 \cdot 10^{-2}$	1.98	$0.0045 \cdot 10^{-2}$	2.01

The results in this section give us confidence in our implementation of the SAV methods within DROPS. In addition, they suggest that for the values of ϵ we consider $\ell = 5$ and $\Delta t = 0.005$ are appropriate levels of refinement for mesh size and time step as they provide small discretization errors and are more computationally efficient than $\ell = 6$ and $\Delta t = 0.0025$. Hence, for the results in the next section we will use $\ell = 5$ and $\Delta t = 0.005$.

5.1.2 Phase separation on the sphere

Our interest in surface phase field problems, such as the Cahn–Hilliard equation [88, 111, 115, 116, 117], stems from their practical applications in targeted drug delivery. The phenomenon of lipid phase separation has been utilized to enhance the delivery performance of targeted lipid vesicles [8, 55], as the formation of phase-separated patterns on the vesicle surface has been associated with increased target selectivity, cell uptake, and overall efficacy. In our previous works [111, 117], we validated our numerical results obtained using the approaches described in [88, 115] against laboratory experiments. We achieved good agreement between the numerical and experimental results for different lipid membrane compositions.

In this dissertation, we consider 3 membrane compositions. Each membrane composition corresponds to a certain fraction a of the sphere surface area (since these vesicles are spherical) covered by one representative phase. In this section, we present results for $a = 0.5, 0.3, 0.7$, which are experimentally relevant values.

In order to model an initially homogenous mix of components, the initial composition c_0 is defined as a realization of Bernoulli random variable $c_{\text{rand}} \sim \text{Bernoulli}(a)$ with mean value a, i.e., we set:

$$c_0 \coloneqq c_{\text{rand}}(\mathbf{x}) \quad \text{for active mesh nodes } \mathbf{x}. \tag{5.2}$$

As mentioned at the end of the previous section, the interface thickness ϵ is set to 0.05, which is a realistic value for lipid vesicles.

Let us start with the results obtained with the SAV-BDF2 method without time step adaptivity and compare them with the results obtained with the stabilized method in [115]. Fig. 4 shows the evolution of phases for $a = 0.5$, which means that 50% of the sphere surface is covered by the representative phase (red in the figure) and the remaining 50% is covered by the other phases (blue in the figure). There is no observable difference in the spinodal decomposition and subsequent domain ripening given by the two methods.

Fig. 5 and 6 display the evolution of phases for $a = 0.3$ and $a = 0.7$, respectively. Notice that

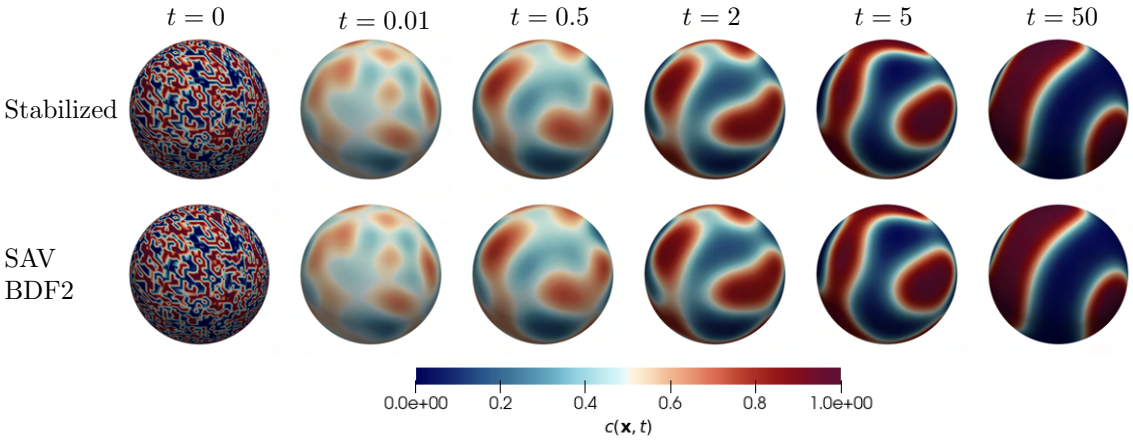

Figure 4: Phase separation on the sphere, $a = 0.5$: evolution of phases computed with the stabilized method in [115] (top) and the SAV-BDF2 method without time step adaptivity (bottom).

there are opposite cases: 30% of the sphere surface is covered by the representative (red) phase for $a = 0.3$, while 30% of the sphere surface is covered by the opposite (blue) phase for $a = 0.7$. If we were to use opposite initial conditions in these two cases, Fig. 5 and 6 would look identical just with inverted colors (red to blue and viceversa). However, the initial conditions were generated randomly according to (5.2) and so the evolution of the red domains in Fig. 5 looks similar (but not identical) to the evolution of the blue domains in Fig. 6. For both values of a though, we see that again there is no observable difference in the solution computed with the stabilized method in [115] and the solution give by the SAV-BDF2 method without time step adaptivity.

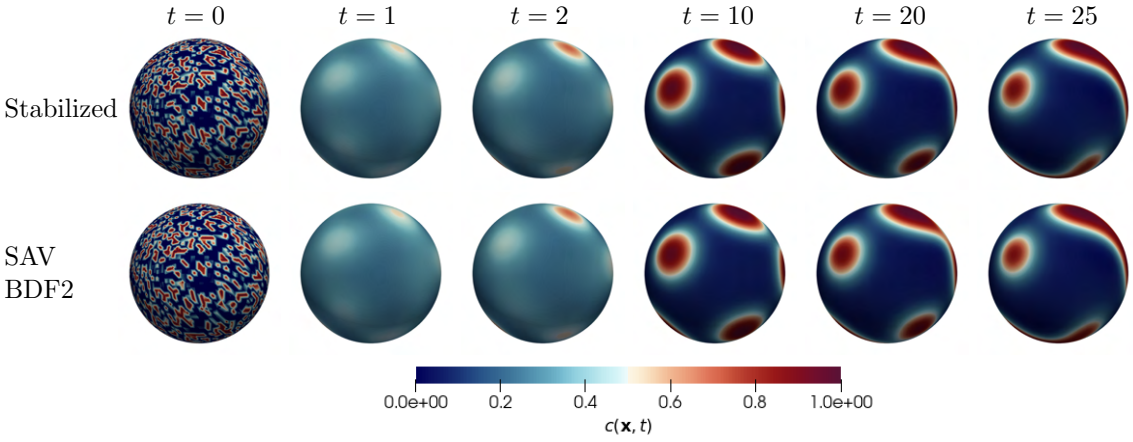

Figure 5: Phase separation on the sphere, $a = 0.3$: evolution of phases computed with the stabilized method in [115] (top) and the SAV-BDF2 method without time step adaptivity (bottom).

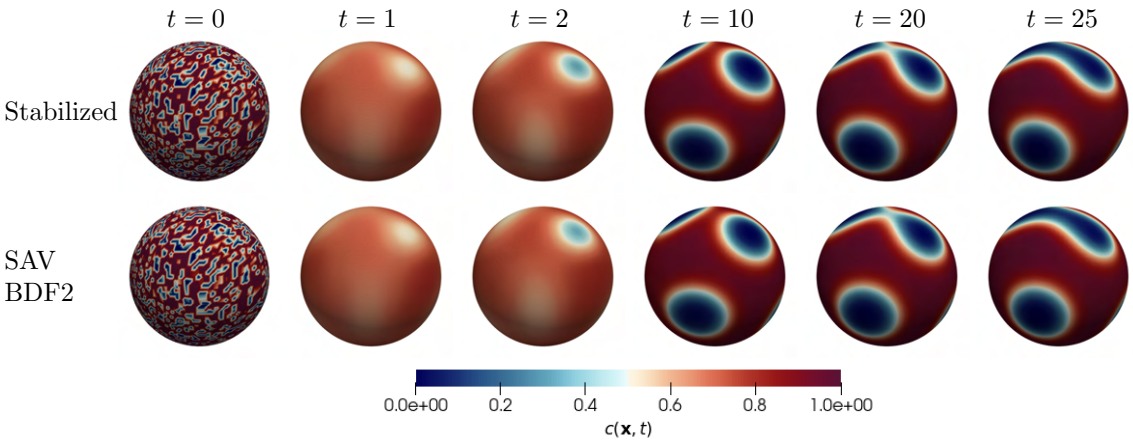

Figure 6: Phase separation on the sphere, $a = 0.7$: evolution of phases computed with the stabilized method in [115] (top) and the SAV-BDF2 method without time step adaptivity (bottom).

Fig. 7 displays the decay of modified energy (4.24) for the three values of a. We see that the decay is more or less rapid depending on the value of a. However, in no case at $t = 25$ the system is close to an energy plateau, which we observed already at $t = 1$ for the simple convergence test in Sec 5.1.1. See the graphs in Fig. 3.

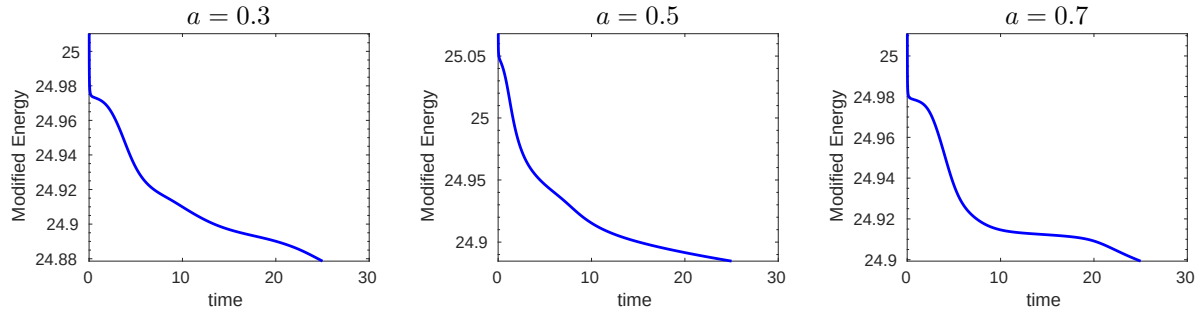

Figure 7: Phase separation on the sphere: decay of modified energy (4.24) for $a = 0.3$ (left), $a = 0.5$ (center), and $a = 0.7$ (right).

Next, we compare the results obtained with the time-adaptive SAV-BDF2 method to those obtained with the stabilized method in [115] in its time adaptive version. For this comparison, we select only one representative value of a, namely $a = 0.5$. In Fig. 8, which illustrates the evolution of phases until reaching the equilibrium configuration, we once again observe no difference in either the spinodal decomposition or the domain ripening between the two methods.

A comparison of the time step sizes and time step number over time is shown in Fig. 9. From

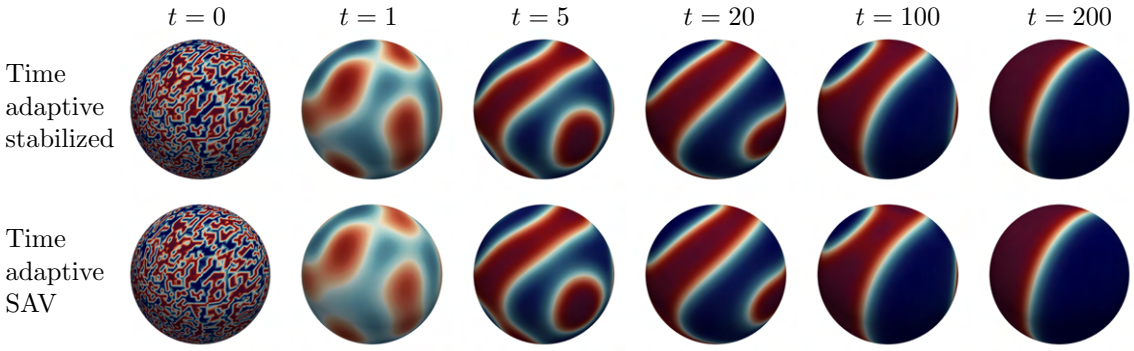

Figure 8: Phase separation on the sphere, $a = 0.5$: evolution of phases computed with the time-adaptive stabilized method in [115] (top) and the time-adaptive SAV-BDF2 method (bottom).

Fig. 9 (left), we can see that the time step grows for both methods until approximately $t = 50$, after which it fluctuates around $\Delta t = 1$. Although the time step sizes are generally comparable for both methods, the SAV method utilizes slightly larger time steps during this initial integration stage. Consequently, time step number n required to integrate the system up to any $t \leq 200$ is smaller for the time-adaptive SAV-BDF2 method compared to the time-adaptive stabilized method in [115]. However, the difference is not significant. See Fig. 9 (right).

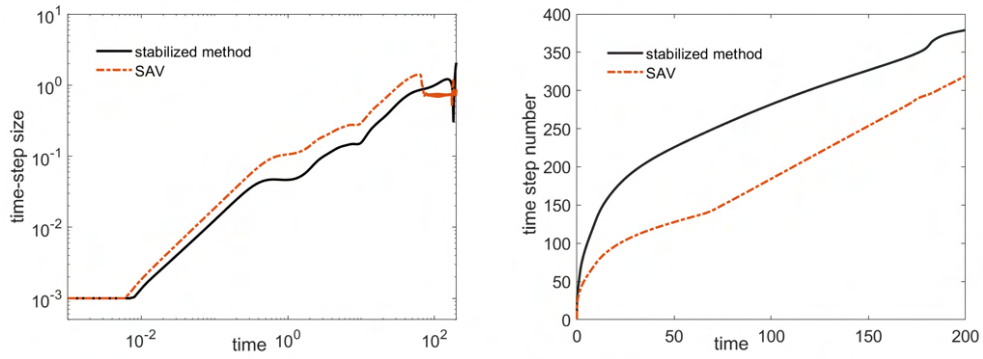

Figure 9: Phase separation on the sphere, $a = 0.5$: evolution of the time step size Δt (left) and number of the time steps required at each time instant (right) for the time-adaptive stabilized method from [115] and the BDF2-SAV method with time step adaptivity.

We conclude this section with a comment on the computational time. All the computations were executed on a machine with an AMD EPYC 7513 32-Core Processor and 512 GB RAM. Fig. 10 reports the computational time needed by the simulations whose results are shown in Fig. 4, 5,

and 6 to complete the first 100 time steps. The time required by the stabilized method in [115] varies between one half and two thirds of the time required by the SAV method with no time step adaptivity. Let us now turn to the simulations in Fig. 8, i.e., those with time adaptivity. The time-adaptive SAV-BDF2 method takes 319 time steps in time interval $(0, 200]$ for a total computational time of about 41 minutes, while the time-adaptive stabilized method in [115] takes about 9 minutes to complete 379 time steps in the same time interval. The simulation with the time-adaptive SAV-BDF2 method requires less time steps but takes longer overall. As mentioned at the end of Sec. 4.2.2, the reason for this difference in the computational times is due to the fact that the extra terms introduced by the SAV method make the matrices of the associated linear systems dense. If one used a finite difference method on uniform grids for space discretization as in [48, 64, 96], higher computational efficiency could be achieved for the SAV method. Our preference for a finite element method and non-uniform meshes is for greater geometric flexibility, as shown in the next subsection.

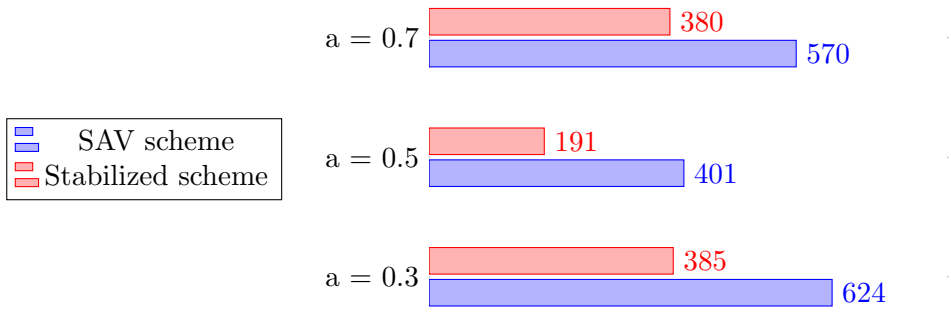

Figure 10: Phase separation on the sphere: computational time (in s) needed by the stabilized method in [115] and the SAV method with no time step adaptivity to complete the first 100 time steps of the simulations in Fig. 4 ($a = 0.5$), 5 ($a = 0.3$), and 6 ($a = 0.7$)

5.1.3 Phase separation on a complex manifold

Because of our interest in phase separation on biological membranes in general, not just lipid vescicles, we need to be able to handle surfaces that are more complex than the sphere. Here, we

consider an idealized cell with surface Γ given by the zero level set of following function [25, 115]:

$$\phi(\mathbf{x}) = \frac{1}{4}x_1^2 + x_2^2 + \frac{4x_3^2}{(1+\frac{1}{2}\sin(\pi x_1))^2} - 1.$$

Fig. 11 illustrates a side view of this complex manifold and an angle view of the surface mesh.

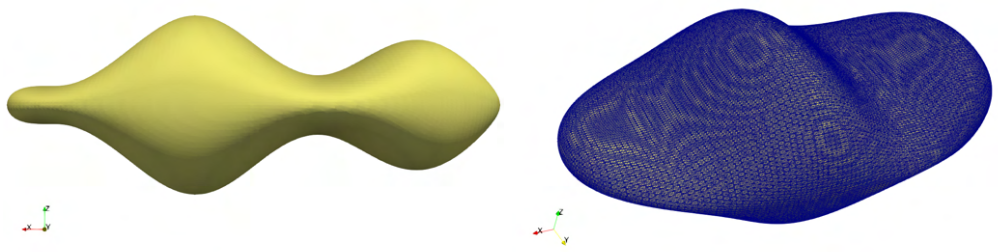

Figure 11: Illustration of the complex manifold

We embed surface Γ in bulk domain $\Omega = [-2, 2] \times [-4/3, 4/3] \times [-4/3, -4/3]$. A tetrahedral mesh for Ω is generated in the same way as for the cases in the previous subsection, i.e., by diving Ω into cubes and then diving the cubes into tetrahedra. The active elements, which are the elements that intersect surface, are further refined for a total of 14298 degrees of freedom. This mesh has a level of refinement comparable to mesh $\ell = 5$ in Sec. 5.1.2. We fix the time step to $\Delta t = 0.005$ and do not allow for time step adaptivity.

We set the interface thickness ϵ to 0.05, like in Sec. 5.1.2. Fig. 12 compares the evolution of the phases given by SAV- BDF2 method without time step adaptivity with the evolution given by the stabilized method in [115] for $a = 0.5$. We recall that $a = 0.5$ means that 50% of the idealized cell surface is covered by the representative (red) phase and the remaining 50% is covered by the other phases. Just like in the case of the sphere (see Fig. 4), there is no observable difference in the results given by the two methods.

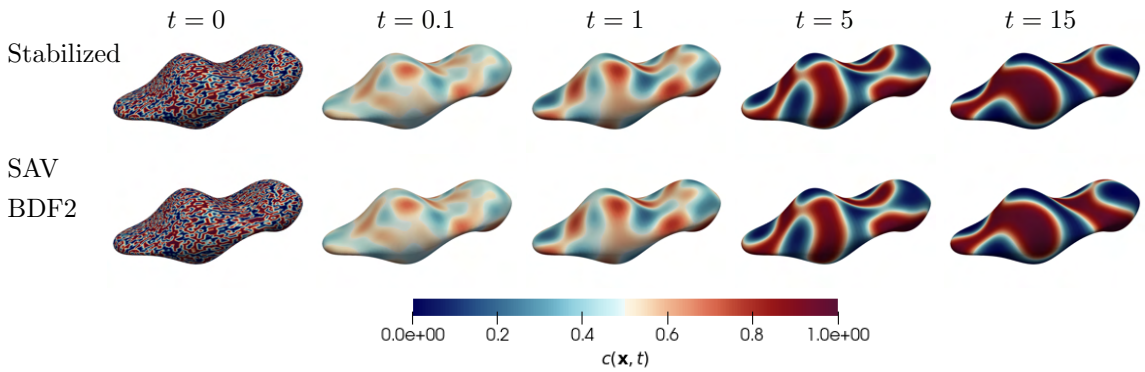

Figure 12: Phase separation on an idealized cell: evolution of phases computed with the stabilized method in [115] (top) and the SAV method and BDF2 without time step adaptivity (bottom).

5.2 Numerical experiments with the Navier–Stokes–Cahn–Hilliard equations

After checking the convergence orders of the method described in Sec. 4.3, we present a series of numerical tests to study well-known two-phase fluid flows (the Kelvin–Helmholtz and Rayleigh–Taylor instabilities) on surfaces. Thanks to our method, we can investigate the effect of line tension on such instabilities. In addition, for the Rayleigh–Taylor instability we assess the effect of viscosity and surface shape.

For all the tests, we choose $\mathbf{P_2}$–P_1 finite elements for fluid velocity and pressure and P_1–P_1 finite elements for surface fraction and chemical potential.

5.2.1 Convergence test

We proceed with checking the spatial accuracy of the finite element method described in Sec. 4.3 with a benchmark test. The aim is to validate our implementation of the method. For this purpose, we consider the two-phase fluid system on the unit sphere centered at the origin. The surface is characterized as the zero level set of function $\phi(\mathbf{x}) = \|\mathbf{x}\|_2 - 1$ and is embedded in an outer cubic domain $\Omega = [-5/3, 5/3]^3$. We choose Van der Waals "tanh" exact solution for the surface fraction and solenoidal Killing vector field for velocity:

$$c^*(t, \mathbf{x}) = \frac{1}{2}\left(1 + \tanh\frac{z\cos(\pi t) - y\sin(\pi t)}{2\sqrt{2}\epsilon}\right), \quad \mathbf{u}^*(t, \mathbf{x}) = \pi\,(0, -z, y)^T.$$

Killing vectors fields such $\mathbf{u}^*$ have been excluded from the analysis in Sec. 4.3.2 for simplicity, but they allow us to build a relatively easy analytical solution. The nonzero CH equation forcing term is computed from (3.15). We set $\epsilon = 0.05$. Fig. 13 (leftmost panel) displays $c(0, \mathbf{x})$. For this test, we consider fluids with matching densities and viscosities: $\rho_1 = \rho_2 = 1$ and $\eta_1 = \eta_2 = 1$. In addition, we set $M = 0.05$ and $\sigma_\gamma = 0$. The time interval of interest is $t \in [0, 1]$, during which the initial configuration c_0 is rotated by 180°. See Fig. 13. Notice that by setting $\sigma_\gamma = 0$ the NSCH system one-way coupled: phase-separation is affected by the fluid flow, but not vice versa.

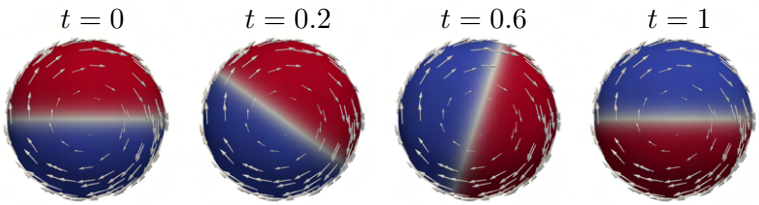

Figure 13: Evolution of the surface fraction c over time computed with mesh $\ell = 5$.

The initial triangulation $\mathcal{T}_{h_\ell}$ of Ω consists of eight sub-cubes, where each of the sub-cubes is further subdivided into six tetrahedra. Further, the mesh is refined towards the surface, and $\ell \in \mathbb{N}$ denotes the level of refinement, with the associated mesh size $h_\ell = \frac{10/3}{2^{\ell+1}}$. For the purpose of numerical integration, we apply several "virtual" levels of refinements for the tetrahedra cut by the mesh and integrate our bilinear forms over a piecewise planar approximation of Γ on this virtual grid. This allowed us to apply a standard quadrature rule and reduce the geometric error in our convergence test. The time step is refined together with the mesh size according to $\Delta t = 1/(25 \cdot 4^{\ell-2})$. First, we show the convergence results obtained with BDF1 for the time discretization of the Cahn–Hilliard problem, which is what we used in (4.50). Table 4 reports the H_1 and L_2 errors for the velocity and the L_2 error for the order parameter at the end of the time interval, i.e., $t = 1$, for levels $\ell = 3, 4, 5$. For each mesh, Table 4 gives the number of sublevels (virtual levels) used for more accurate numerical integration. We observe slightly better than expected convergence rates for the velocity, which might be the effect of the interplay between interpolation and geometric error reduction. We notice that we are able to refine the time step more aggressively than the

spacial mesh size. Thus, we hypothesize that the restrictions on h in terms of Δt in Theorem 4.5 may be an artifact of the analysis.

Table 4: H_1 and L_2 errors for the velocity and the L_2 error for surface fraction at $t = 1$ for levels $\ell = 3, 4, 5$ and rate of convergence when BDF1 is used for the time discretization of the Cahn–Hilliard problem

ℓ	sublevels	$\|\|\mathbf{u}^* - \mathbf{u}_h\|\|_{H^1(\Gamma)}$	rate	$\|\|\mathbf{u}^* - \mathbf{u}_h\|\|_{L^2(\Gamma)}$	rate	$\|\|c^* - c_h\|\|_{L^2(\Gamma)}$	rate
3	1	0.097166		0.009215		0.448303	
4	2	0.019923	2.29	0.000572	4.01	0.174764	1.36
5	4	0.004541	2.13	0.000059	3.28	0.048930	1.84

Next, we switch to BDF2 for the time discretization of the Cahn–Hilliard problem and allow for a larger time step: $\Delta t = 1/(25 \cdot 2^{\ell-2})$. Notice that the time step is refined linearly to compare with the results in Table 4. Table 5 reports the corresponding errors and rates of convergence. In this case, we observe a slightly better than expected convergence rate for c too.

Table 5: H_1 and L_2 errors for the velocity and the L_2 error for surface fraction at $t = 1$ for levels $\ell = 3, 4, 5$ and rate of convergence when BDF2 is used for time discretization of the Cahn–Hilliard problem

ℓ	sublevels	$\|\|\mathbf{u}^* - \mathbf{u}_h\|\|_{H^1(\Gamma)}$	rate	$\|\|\mathbf{u}^* - \mathbf{u}_h\|\|_{L^2(\Gamma)}$	rate	$\|\|c^* - c_h\|\|_{L^2(\Gamma)}$	rate
3	1	0.081485		0.010026		0.311232	
4	2	0.016800	2.28	0.000619	4.02	0.081597	1.93
5	4	0.003905	2.10	0.000046	3.75	0.015086	2.43

5.2.2 The Kelvin–Helmholtz instability

While the Kelvin–Helmholtz (KH) instability is a classical example of two-phase fluid flow in planar or volumetric domains, the number of numerical studies on curved surfaces is limited. The KH instability arises when there is a difference in velocity at the interface between the two fluids and a perturbation is added to the interface. This perturbation eventually makes the interface curl up and generates a vortex strip. Here, we will simulate the KH instability on a sphere and investigate the effect of varying line tension.

To design this experiment, we follow what is done in [61, 52, 87]. The initial velocity field is given by the counter-rotating upper and lower hemispheres with speed approximately equal 1 closer

to equator and vanishing at the poles. The velocity field has a sharp transition layer along the equator, where the perturbation is added. See, e.g., [87] for details on the perturbation. The initial surface fraction is given by

$$c_0 = \frac{1}{2}\left(1 + \tanh\frac{z}{2\sqrt{2}\epsilon}\right),$$

where $\epsilon = 0.01$. Also for this test, we consider fluids with matching densities and viscosities: $\rho_1 = \rho_2 = 1$ and $\eta_1 = \eta_2 = 10^{-5}$. In addition, we set $M = 0.01$. We consider time interval $[0, 10]$.

We select mesh level $\ell = 6$ (see mesh description for the previous test). We choose $\Delta t = 1/640$. Fig. 14 and 15 show the evolution of surface fraction and vorticity for three different values of line tension: $\sigma_\gamma = 0, 0.01, 0.1$. The evolution of both quantities does not vary significantly when going from $\sigma_\gamma = 0$ to $\sigma_\gamma = 0.01$, although some differences can be noticed from $t = 4.5$ on. Changing to $\sigma_\gamma = 0.1$ produces more evident differences, starting already from $t = 1.375$. When $\sigma_\gamma \neq 0$, the NS part of the CHNS system is two-way coupled to the CH part. So, the differences are significant both for surface fraction and vorticity.

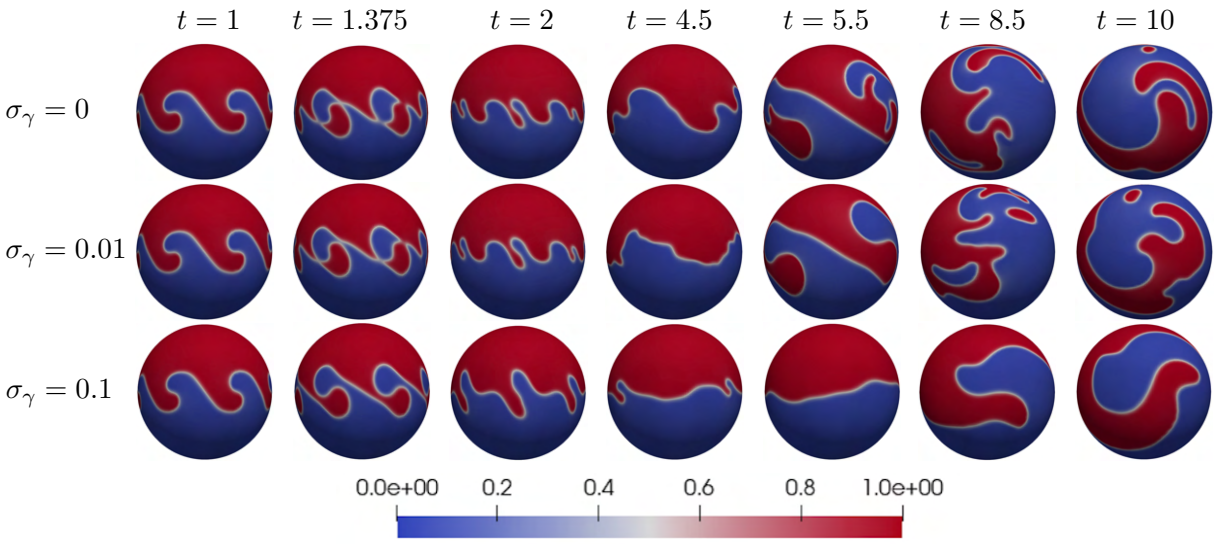

Figure 14: KH instability: evolution of order parameter for different values of line tension: $\sigma = 0$ (top), $\sigma = 0.01$ (center), and $\sigma = 0.1$ (bottom).

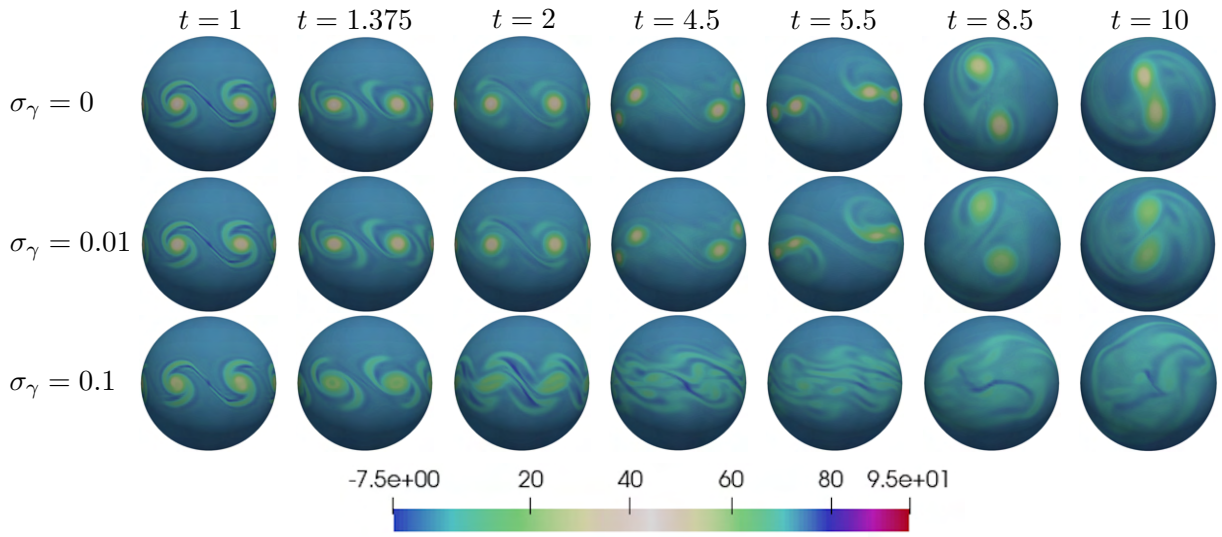

Figure 15: KH instability: evolution of the vorticity for different values of line tension: $\sigma_\gamma = 0$ (top), $\sigma_\gamma = 0.01$ (center), and $\sigma_\gamma = 0.1$ (bottom).

5.2.3 The Rayleigh–Taylor instability

The Rayleigh–Taylor (RT) instability occurs when a gravity force (taken to be $(0, 0, -1)$) is acting on a heavier fluid that lies above a lighter fluid. As the RT instability develops, "plumes" of the lighter fluid flow upwards (with respect to the gravitational field) and "spikes" of the heavier fluid fall downwards. We will simulate the RT instability on a sphere and on a torus with the aim of investigating the effect of the geometry. In addition, we will vary line tension and fluid viscosity.

We take two fluids with densities $\rho_2 = 3$, $\rho_1 = 1$ and matching viscosities $\eta_1 = \eta_2 = \eta$, which will be specified for each test. The initial surface fraction is given by

$$c_0 = \frac{1}{2}\left(1 + \tanh\frac{z + z_{rand}}{2\sqrt{2}\epsilon}\right),$$

where $\epsilon = 0.025$ and z_{rand} is a uniformly generated random number from the range $(-0.1\epsilon, 0.1\epsilon)$. The role of the perturbation generated by z_{rand} is to onset the RT instability. We set $M = 0.0025$.

Let us start with the sphere. We select mesh level $\ell = 5$ (see mesh description for the convergence test) and set $\Delta t = 0.1$. Fig. 16 shows the evolution of the surface fractions and velocity field for $\eta = 10^{-2}$ and two values of line tension: $\sigma_\gamma = 0$ and $\sigma_\gamma = 0.025$. At time $t = 7$, for $\sigma_\gamma = 0.025$ we

observe the characteristic flow structures of the RT instability. Instead, for $\sigma_\gamma = 0$ such structures have already broken up at $t = 7$. The effect of line tension is also seen at $t = 30$: for $\sigma_\gamma = 0.025$ we observe that the heavier fluid has already settled at the bottom of the sphere, while for $\sigma_\gamma = 0$ that has not happened yet. It takes till $t = 55$ to have the heavier fluid at the bottom in the absence of line tension. After the revolution, the fluid phases do not achieve steady state quickly but the waves keep traveling along the equator.

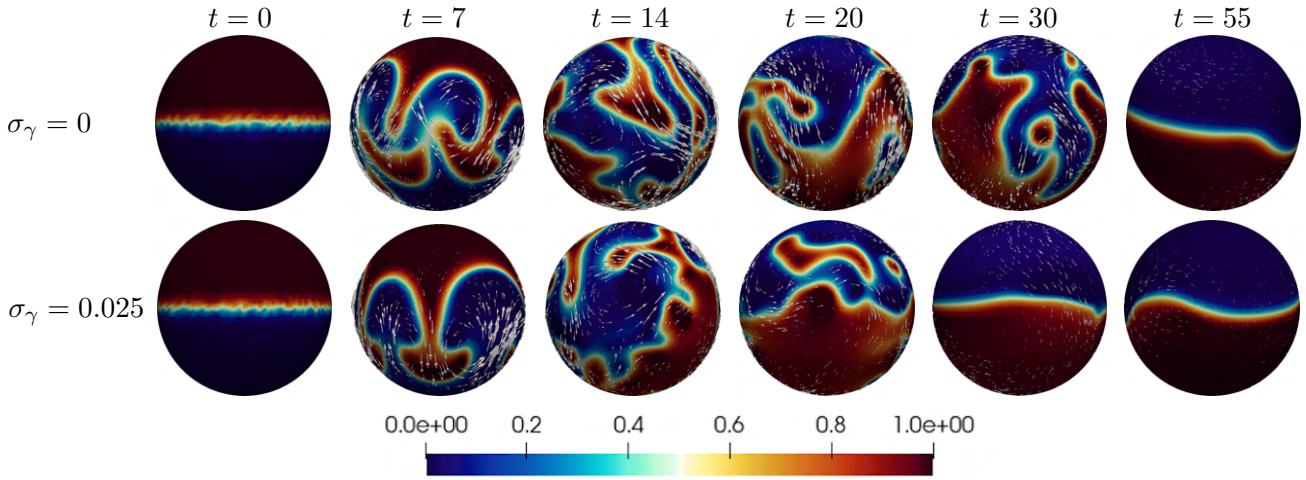

Figure 16: RT instability on the sphere: evolution of the order parameter (color) and velocity field (arrows) for $\eta = 10^{-2}$ and different values of line tension: $\sigma_\gamma = 0$ (top) and $\sigma_\gamma = 0.025$ (bottom).

Next, we consider an asymmetric torus with constant distance from the center of the tube to the origin $R = 1$ and variable radius of the tube: $r_{min} = 0.3 \leq r(x, y) \leq r_{max} = 0.6$, with $r(x, y) = r_{min} + 0.5(r_{max} - r_{min})(1 - \frac{x}{\sqrt{x^2+y^2}})$. We characterize the torus surface as the zero level set of function $\phi = (x^2+y^2+z^2+R^2-r(x,y)^2)^2-4R^2(x^2+y^2)$. The torus is embedded in an outer domain $\Omega = [-5/3, 5/3]^3$, just like the sphere. We also selected same mesh level ($l = 5$) and same time step ($\Delta t = 0.1$) as for the sphere. We set the line tension to $\sigma = 0.025$ and vary the viscosity: $\eta = 10^{-2}, 10^{-1}, 1$. Fig. 17 displays the evolution of the surface fractions for these three values of viscosity. First, we observe that in all cases the instability develops more slowly on the "skinny" side of the torus. See second column in Fig. 17. The fact that geometry has a considerable effect on the surface RT instability is also clear when one compares the results on the sphere and the torus for the same values of σ_γ and η, i.e., the top row in Fig. 17 with the bottom row in Fig. 16.

In particular, notice that while the heavier fluid reaches the bottom of the sphere around $t = 30$ (Fig. 16, bottom second-last panel), the two fluids are still very much mixed on the torus at $t = 160$ (Fig. 17, top left panel). We need to increase the viscosity value to 1 to be able to see most of the heavier fluid at the bottom of the torus at $t = 160$ (Fig. 17, bottom left panel), although that is still far from being settled.

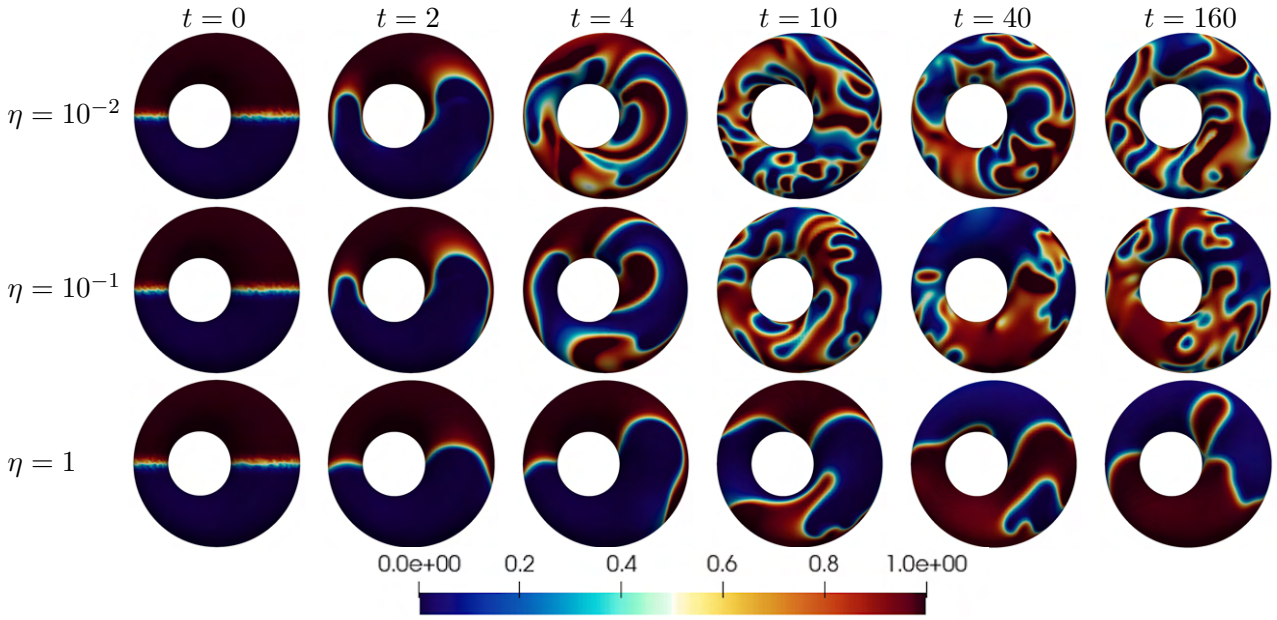

Figure 17: RT instability on the torus: evolution of the order parameter for $\sigma_\gamma = 0.025$ and different values of viscosity: $\eta = 10^{-2}$ (top), $\eta = 10^{-1}$ (center), and $\eta = 1$ (bottom).

6 Applications

6.1 Mathematical model

In this section, we apply our NSCH model to investigate i) the coarsening and fluidity of lipid vesicles and ii) the fusogenicity of lipid vesicles. In order to reproduce and predict experimentally observed phenomena, the mathematical model needs to account for three major physical factors: i) phase separation, ii) surface density flow, and iii) electrostatic forces. The thermodynamically consistent NSCH model accounts only for i) and ii), i.e., only phase separation and flow phenomena occurring in lipid membranes can be modeled computationally. Here, we extend the NSCH model to include the electrostatic forces between the positively charged lipids in the SUVs and the GUVs, whose average measured zeta potential is negative (see Table 7).

Let Γ be a sphere representing the lipid vesicles let $\mathbf{F}_e$ denote the electrostatic force per unit surface area acting on the lipid vesicle. The NSCH equations (3.13)-(3.16) with the electrostatic force term are used to model membranes. Specifically, the NSCH system with electrostatic forcing that governs the evolution of c, $\mathbf{u}$, p, and μ in time t and space $\mathbf{x} \in \Gamma \subset \mathbb{R}^3$ is given by:

$$\underbrace{\rho(\partial_t \mathbf{u} + (\nabla_\Gamma \mathbf{u})\mathbf{u})}_{\text{inertia}} - \underbrace{\mathbf{div}_\Gamma(2\eta E_s(\mathbf{u})) + \nabla_\Gamma p}_{\text{lateral stresses}} = \mathbf{F}_e \underbrace{-\sigma_\gamma \epsilon^2 \operatorname{div}_\Gamma(\nabla_\Gamma c \otimes \nabla_\Gamma c)}_{\text{line tension}} + \underbrace{M\theta(\nabla_\Gamma(\theta \mathbf{u}))\nabla_\Gamma \mu}_{\text{chemical momentum flux}} \tag{6.1}$$

$$\underbrace{\operatorname{div}_\Gamma \mathbf{u} = 0}_{\text{membrane inextensibility}} \tag{6.2}$$

$$\underbrace{\partial_t c + \operatorname{div}_\Gamma(c\mathbf{u})}_{\text{transport of phases}} - \underbrace{\operatorname{div}_\Gamma(M\nabla_\Gamma \mu)}_{\substack{\text{phase masses exchange} \\ \text{Fick's law}}} = 0, \qquad \mu = \underbrace{f_0'(c) - \epsilon^2 \Delta_\Gamma c}_{\text{mixture free energy variation}} \tag{6.3}$$

on Γ for $t \in (0, t^{\text{final}}]$.

In the next Section 6.2, we investigate the coarsening and fluidity of lipid vesicles. For the purposes of this section we set $\mathbf{F}_e = 0$. In the subsection 6.3, we discuss the fusogenicity of lipid vesicles. Further details are provided in the corresponding subsections.

6.2 Lipid domain coarsening and fluidity in multicomponent lipid vesicles

Biological membranes are heterogenous and this characteristic is critical for their functionality. The lipid bilayer in these membranes hosts a variety of lipid species that may be organized into one of the two phases: liquid disordered and liquid ordered [107]. The tight packing of saturated lipids and cholesterol in the liquid ordered phase, in contrast to the loosely packed unsaturated lipids present in the liquid disordered phase leads, under certain conditions, to the lipid phase separation in membranes [13]. The liquid ordered domains - also known as lipid rafts - that are surrounded with liquid disordered phase in biological membranes, have been recognized as a key platform for cell signaling and membrane trafficking among other cellular processes [13, 12, 69, 7, 104]. Thus, these domains have received growing interest in the past few decades and have been the focus of numerous experimental and theoretical studies [62, 9].

More recently, domain formation on membranes has also been utilized to create novel membrane-based materials with heterogenous surfaces. When explored for drug delivery applications, these heterogenous membrane materials showed clear advantage over their homogenous membrane counterparts [8, 91]. With the increasing number of available lipid-conjugated molecules (e.g., peptides, polymers, etc.), lipid membranes with heterogenous and spatially-organized surfaces can open new avenues for the design of novel materials. However, efficient design of such heterogenous membrane-based materials requires computer-aided modeling that can predict the lipid domain formation and dynamics on a given membrane composition in a reliable and quantitative manner.

Our current understanding of membrane phase separation is mainly based on the experimental studies performed on model membranes with well-defined lipid compositions. Amongst these model membranes, giant unilamellar vesicles (GUVs) have provided a particularly suitable platform for studying membrane phase behavior as their free-standing lipid bilayer closely mimics the natural membranes and their large size (micron-scale) makes them resolvable under optical microscopy [112]. The combined use of GUVs and advanced fluorescence-based microscopy techniques have, for instance, shaped our knowledge on membrane domains' thermodynamic equilibria [106, 31]

and their coarsening dynamics [101]. These studies have also provided us with an insight into the distinct characteristics (e.g. morphology and fluidity) of liquid ordered and liquid disordered phases [54, 92, 93].

It has been demonstrated that membrane fluidity within the liquid ordered domains can be substantially lower than that in the liquid disordered phase [93]. Such a difference can affect the coarsening dynamics of domains on membranes [101]. This interesting aspect of lipid domains was not considered in our previous study [117] as fluidity is not accounted for in the Cahn–Hilliard model. Hence, we apply the Navier–Stokes–Cahn–Hilliard model, and compare its numerical results to our experimental data on GUVs with ternary membrane compositions. Specifically, we examine the phase separation on GUVs with two distinct compositions (with opposite and nearly inverse phase behavior) and monitor the number of lipid domains, area fraction and perimeter over time and compare these results to those from our computational model. It is noteworthy that the Cahn–Hilliard model would predict nearly the same evolution of the domain ripening process for these two compositions. However, our experiments reveal different domain ripening dynamics, which can be captured by the more complex Navier–Stokes–Cahn–Hilliard model.

Lipid compositions applied in this study were (i) DOPC: DPPC with a 1:1 molar ratio and 15% Chol, referred to as 1:1:15% composition, and (ii) DOPC: DPPC with a 1:2 molar ratio and 25% Chol, referred to as 1:2:25% composition. Details of GUV preparation, materials and imaging process can be found in the following paper [111].

Several experimental works help with the settings of viscosity [90] and line tension [45, 58, 59]. For density, we calculated the value for each phase using the estimated molecular weight and molecular surface area for the corresponding phase [111].

In order to model an initially homogenous liposome, the surface fraction c_0 is defined as a realization of Bernoulli random variable $c_{\text{rand}} \sim \text{Bernoulli}(a_D)$ with mean value a_D, where a_D denotes domain area fraction, i.e., we set:

$$c_0 \coloneqq c_{\text{rand}}(\mathbf{x}) \quad \text{for active mesh nodes } \mathbf{x}. \tag{6.4}$$

Following the thermodynamic principles described in our previous work [117], we set $a_D = 0.71$ for the 1:2:25% (DOPC : DPPC : Chol) composition and $a_D = 0.29$ for the 1:1:15% composition.

6.2.1 Results and Discussion

We focused on a ternary membrane composition DOPC:DPPC:Chol, which is known to separate into co-existing liquid ordered (l_o) and liquid disordered (l_d) phases near room temperature when mixed in proper ratios [53, 105]. Upon phase separation, the l_d phase is composed primarily of DOPC and the l_o phase is primarily composed of Chol and DPPC. The relative size of these two phases can be tuned by adjusting the molar ratio of the lipid components. To assess our model of phase separation, we decided to focus our experiments on two membrane compositions that provide distinct and nearly opposite phase-behavior: one composition with majority l_o phase and the other one with a minority l_o phase. We chose membranes composed of DOPC:DPPC:Chol at molar ratio of 1:1:15%, in which the l_o phase is predicted to occupy about 29% of the membrane surface at 25°C and 1:2:25%, in which the l_o phase would occupy about 70% of the membrane area at 15°C. These area fractions were calculated using an approach described in [117] that relies on the composition of each phase (determined based on the phase diagram tie-lines [106]) and the molecular area of the lipid components. The Cahn–Hilliard model, as well as continuum based models applied in other studies [109, 74, 100, 63, 32], would predict nearly the same evolution of the domain ripening process for these two compositions since it does not account for in-membrane viscous and transport effects. However, the experimental data presented in this section reveal a different domain ripening dynamics, which can be correctly captured by the more complex NSCH model (6.1)-(6.3).

Using confocal fluorescence microscopy, our collaborators examined a minimum of 18 GUVs (from 4-5 independent experiments) for the number of their lipid domains as well as area and perimeter of domains at different time points, for each GUV composition. The fraction of vesicle surface area occupied by the l_o phase, i.e., lipid domain area fraction, in GUVs was calculated from the confocal images.

Independent of the experimental results, 10 numerical simulations were run for each composition. All the simulated liposomes had a 10 µm diameter and they differed in the realization of the random variable used to set up initial state. For each simulation, we tracked the total lipid domain perimeter and the total number of lipid domains in order to compare with the experimental data. The computed lipid domain area fraction is not reported since, the NSCH model is conservative and thus the lipid domain area fraction stays constant over time.

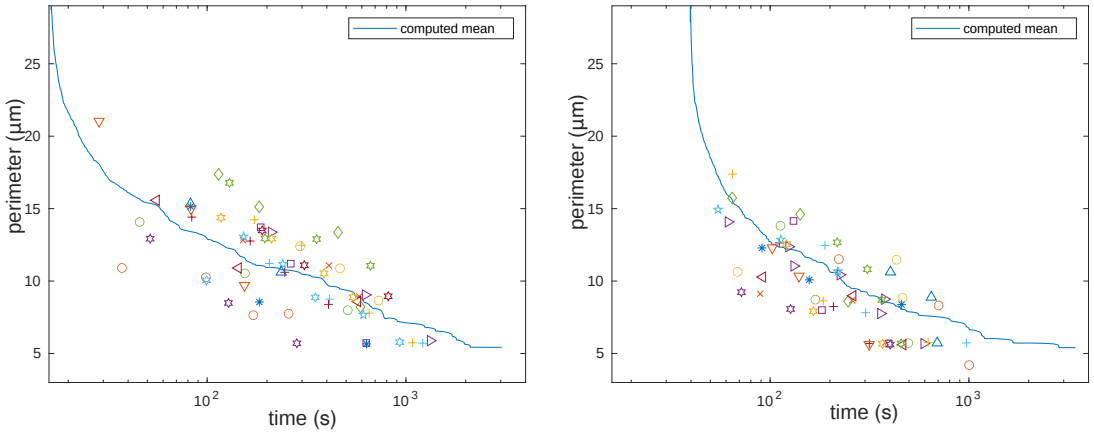

Figure 18: Total lipid domain perimeter in µm over time for composition 1:2:25% (left) and 1:1:15% (right): numerical results average (solid line) and experimental data (markers).

In order to compare the total lipid domain perimeter between simulations and experiments, we first scaled all dimensional observables that depend on a length unit by the radius of the corresponding GUV, since the diameter of GUVs varied in the experiments (between 9-16 µm) while it was constant in the simulations. Fig. 18 reports all the rescaled experimental measurements with markers (a different marker for each GUV) and the average of the computed total lipid domain perimeter from all the simulations with a solid line for compositions 1:2:25% and 1:1:15%. In both cases, the average of the computed total lipid domain perimeters falls within the cloud of experimental measurements. We note that no experimental measurement is available before 40 s because no lipid domains were observed in this time frame, presumably due to the small size of domains that could not be resolved under fluorescence microscopy. We introduced a time shift to match the time in the computations with the time in the experiments (i.e., the time on the horizontal axis) in Fig. 18. Indeed, the initial time for the computations is the time when phase

separation is initiated, which is hard to observe experimentally.

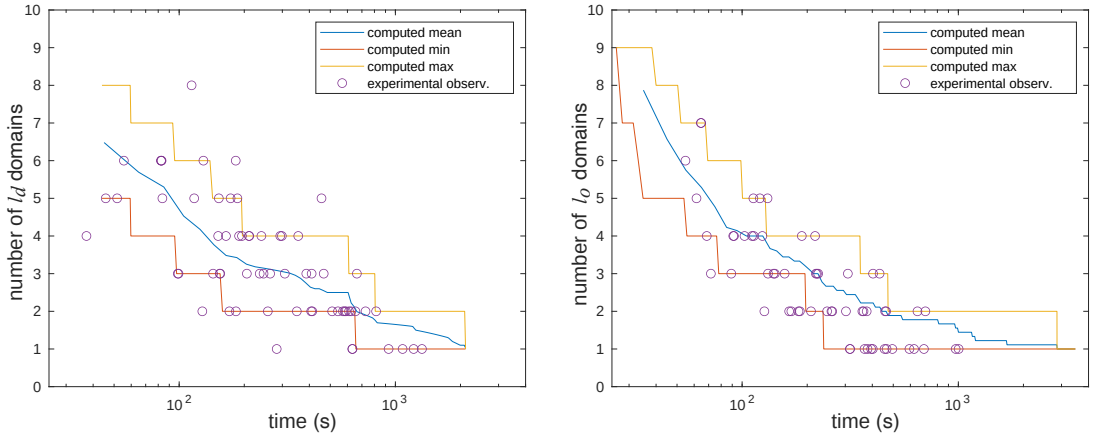

Figure 19: Total number of lipid domains over time for composition 1:2:25% (left) and 1:1:15% (right): numerical results average (solid blue line), minimum and maximum values found numerically (solid orange and yellow lines, respectively), and experimental data (circles).

Next, we performed a quantitative comparison for the total number of lipid domains on a GUV over time. Fig. 19 shows the experimentally measured and numerically computed data for both examined compositions. The measurements are reported with a circle, while for the simulations we reported three solid lines corresponding to the numerical results average, minimum, and maximum number of lipid domains found in the simulations. We see that the vast majority of the experimental data (89% for composition 1:2:25% and 91% for composition 1:1:15%) falls within the computed extrema.

In order to facilitate the understanding of the different domain ripening dynamics for the two membrane compositions under consideration, we superimpose the experimental data for total lipid domain perimeter and total number of lipid domains in Fig. 20. We observe in average faster dynamics towards the equilibrium state (i.e., one domain of the minority phase within a background of the majority phase) for composition 1:1:15%, which has majority l_d phase. This is correctly captured by the NSCH model. Indeed, we see that the solid blue curve (corresponding to the computed mean for composition 1:1:15%) lies below the red curve (corresponding to the computed mean for composition 1:2:25%) for the majority of the time interval under consideration in both graphs in Fig. 20. With consideration of membrane viscosity in each phase, the NSCH model

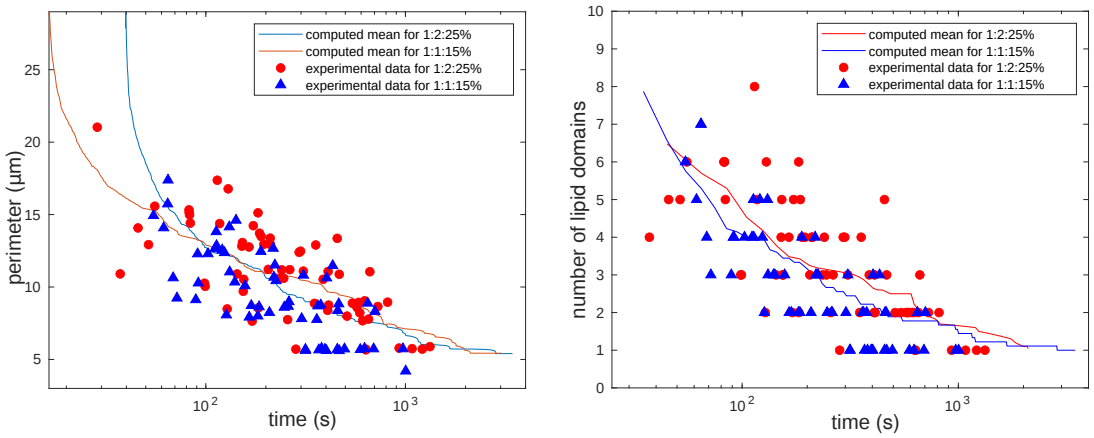

Figure 20: Superimposition of experimental data for composition 1:2:25% (red dots) and 1:1:15% (blue triangles) with the corresponding computed means (solid line with corresponding color) for the total lipid domain perimeter (left) and total number of lipid domains (right).

provides a more accurate prediction of phase separation dynamics in membranes with the opposite phase behavior.

To further compare the experimental data to the simulation results, we present a qualitative comparison between images acquired with epi-fluorescence microscopy and images obtained from post-processing the numerical results. Fig. 21 and Fig. 22 present such comparison for compositions 1:2:25% and 1:1:15%, respectively. Overall, from Fig. 21 and 22 we see an excellent qualitative agreement between experiments and simulations.

Beyond the experimental validation presented above, numerical simulations can provide information about quantities that cannot be measured experimentally or phenomena that cannot be visualized, e.g., the flow field. Fig. 23 shows the evolution of the computed velocity vectors superimposed to the computed surface fraction for both compositions. We observe a larger velocity magnitude when there are several lipid domains on the surface that are in the process of merging. The velocity magnitude becomes smaller as the number of lipid domain decreases and the system gets closer to an equilibrium. Such flow field details could be of interest in other contexts, such as evolution of rafts in cell membranes.

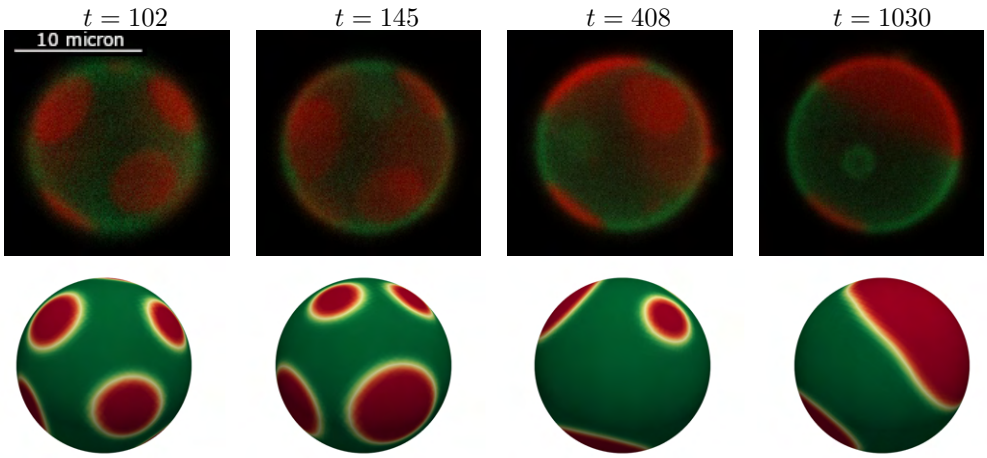

Figure 21: Qualitative comparison for 1:2:25%: epi-fluorescence microscopy images (with black background) and numerical results (with white background) at four different times in time interval $[102, 1030]$ s.

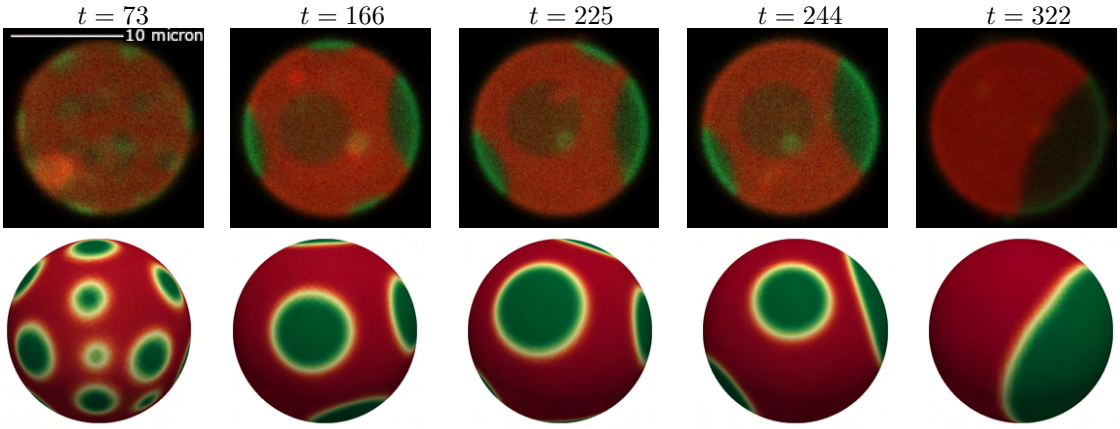

Figure 22: Qualitative comparison for 1:1:15%: epi-fluorescence microscopy images (with black background) and numerical results (with white background) at five different times in time interval $[73, 322]$ s.

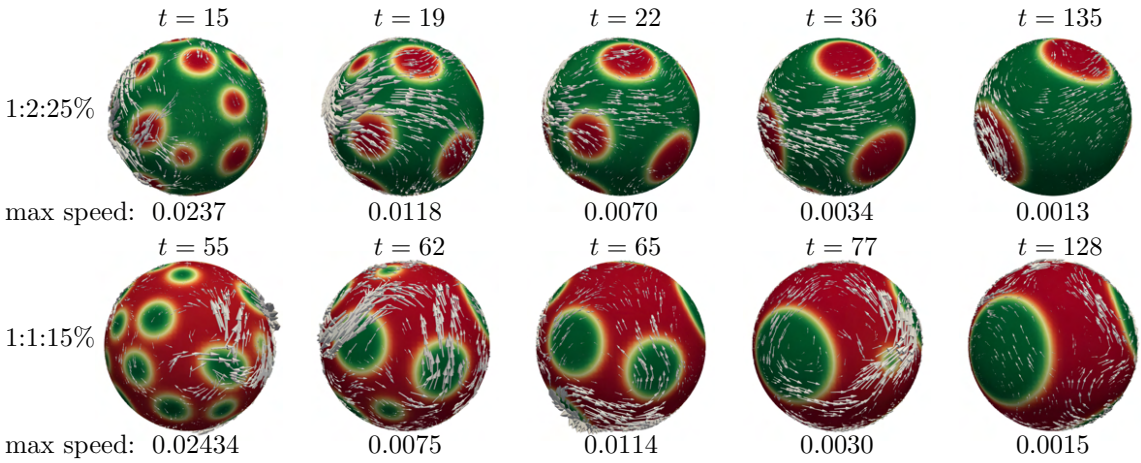

Figure 23: Composition 1:2:25%: Evolution of the velocity vectors superimposed to the lipid domains and maximum speed in µm/s for composition 1:2:25% (top) and 1:1:15% (bottom). The velocity vectors are magnified by a factor 100, 300, 300, 700, and 1500 (from left to right) for visualization purposes.

6.3 On fusogenicity of positively charged phased-separated lipid vesicles

Liposomes that contain cationic lipids [50, 6], such as 1,2-dioleoyl-3-trimethylammonium-propane (DOTAP), are known for their high fusogenicity [99]. Cationic lipids, with their conical shape and cationic headgroup, are critical for fusion [72, 46, 57]. While these lipids are typically non-toxic at lower concentrations, concerns arise regarding their toxicity when used at higher concentrations, attributed to their tetraalkylammonium moiety [75]. Therefore, designing delivery liposomes that offer both high fusogenicity and low toxicity is a challenge. This challenge may be overcome by controlling the surface density of cationic DOTAP on the surface of liposomes using the membrane phase separation phenomenon.

Phase separation is a fundamental process that occurs in multicomponent lipid membranes with substantial unfavorable interactions among their lipid components [44]. Ternary mixture of DOPC:DPPC:Chol is an example of a phase-separating composition that can, for instance, form a tightly-packed liquid ordered phase and a loosely-packed liquid disordered phase at certain molar ratios. We previously combined experiments and modeling to investigate the phase behavior in this lipid mixture. Here, we aim to explore the use of phase-separation in DOTAP:DOPC:DPPC:Chol mixture to modulate surface density of DOTAP on liposomes and hence their fusogenicity.

We hypothesize that concentrating DOTAP into small patches on the liposome's surface, through phase separation, can enhance the liposome's fusogenicity without the need for high DOTAP concentrations. We further postulate that liposomes with the smallest patch area (i.e., the highest local density of DOTAP when the amount of DOTAP is kept fixed) would exhibit the highest level of fusogenicity into target membranes when compared to other liposomes with similar DOTAP content. To test these hypotheses, we examine the fusogenicity of nano-scale liposomes (referred to as small unilamellar vesicles - SUVs) of three different phase-separating compositions containing DOTAP (referred to as patchy liposomes - PAT) into micron-sized liposomes (referred to as giant unilamellar vesicles - GUVs) as model target membranes. Fluorescence microscopy was used as a tool to assess the level of SUV fusogenicity. To enable fluorescence microscopy as a gauge tool, different fluorescent lipids, Rho-PE and AF488-PE, were added to SUV and GUV membranes, respectively. The setup is schematically illustrated in Fig. 24.

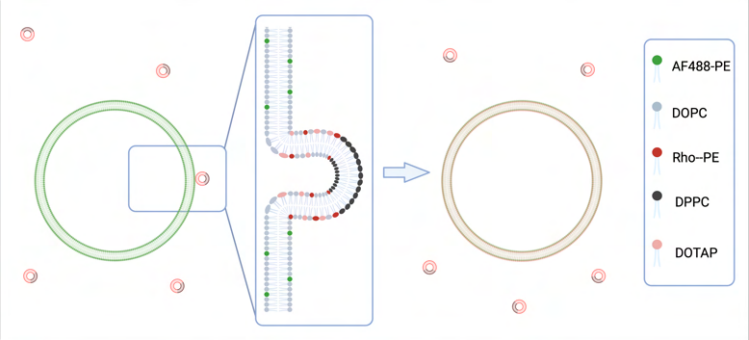

Figure 24: Schematic illustration of the phase-separated cationic SUVs (labeled with red-fluorescent lipids) fusing in to GUVs (labeled with green-fluorescent lipids).

To set viscosity and line tension, we referred to experimental work from [90, 45, 58, 59]. In [111], we calculated the value of density for each phase using the estimated molecular weight and molecular surface area for the corresponding phase. However, those values do not take into account the fact that the vesicle is loaded with and surrounded by an aqueous solution. Hence, in this work we have increased the values to account for the "added mass" coming from such solution. Table 6 reports the domain (L_o phase) area fraction a_D and the values or range of values for viscosity, line tension, and density for the compositions under consideration. We note that temperature

does not appear in eq. (6.1)–(6.3), which describe the evolution of phases and coupled surface flow independently of what initiates phase separation. Indeed, the same model could be used if phase separation was triggered by, e.g., pH [7] instead of temperature. This assumes that variations of the temperature are small (thermodynamically insignificant) after the phase separation is initiated.

Table 6: Domain (L_o phase) area fraction a_D (at the given temperature), value or range of values for the density of liquid ordered (ρ_{L_o}) and liquid disordered (ρ_{L_d}) phases in Kg/(mol·Å^2), viscosity of liquid ordered (η_{L_o}) and liquid disordered (η_{L_d}) phases in 10^{-8} Pa·s·m, and line tension in pN for the three membrane compositions under consideration

Composition	a_D	ρ_{L_o}	ρ_{L_d}	η_{L_o}	η_{L_d}	σ_γ
PAT1	10.8% (15°C)	1401	1172	$0.5-6$	$0.2-0.4$	$1.2-1.4$
PAT2	34.57% (17.5°C)	1401	1172	$0.43-5.7$	$0.2-0.4$	$1.2-1.6$
PAT3	70.37% (15°C)	1435	1172	$5-8$	$0.2-0.4$	$1.2-1.8$

In the simulations, we exposed one SUV to one GUV. Because the GUVs are significantly larger than the SUVs, the curvature of a GUV is negligible at the scale given by the size of an SUV. Hence, we will approximate a GUV with a plane for the computation of the electrostatic force $\mathbf{F}_e$. Therefore, the electric field $\mathbf{E}$ generated by a GUV can be (locally) computed by:

$$\boldsymbol{E} = \frac{\sigma}{2\varepsilon_0}, \tag{6.5}$$

where σ is the GUV surface charge density and ε_0 is the vacuum permittivity ($8.85 \cdot 10^{-12}\,\mathrm{F\,m^{-1}}$). The value of σ is estimated from a linear approximation of Grahame's formula [42], which is valid in low-potential situations:

$$\sigma \approx \varepsilon \cdot \varepsilon_0 \cdot \kappa \cdot \Psi_0, \quad \Psi_0 = \frac{\zeta}{\exp(-\kappa \cdot x)}, \tag{6.6}$$

where ε is the relative permittivity of water (about 80 at 20°C), κ is the Debye length parameter for a NaCl solution (10/7 $\mathrm{nm^{-1}}$ [20]), Ψ_0 is the surface potential [20], x is the slip plane (0.24 nm [20]), and ζ is the zeta potential. The measured average zeta potentials for the GUVs and SUVs are reported in Table 7.

Table 7: Measured average zeta potentials for the GUVs composed of DOPC (in sucrose solution) and patchy SUVs (in dilute PBS) used in the experiments

Vesicle	Zeta Potential
GUV	-8.56 mV
PAT1	18.35 mV
PAT2	18.87 mV
PAT3	20.41 mV

Once the electric field $\mathbf{E}$ is computed, the electrostatic force $\mathbf{F}_e$ in (6.1) is given by $\mathbf{F}_e(\mathbf{x}) = \mathbf{E}q(\mathbf{x})$, where q is a point charge located at $\mathbf{x}$ on an SUV (see Fig. 25). Since we cannot measure a point charge on an SUV, we resort to an approximation. We find the surface charge density (6.6) for an SUV using the measured zeta potentials reported in Table 7 for each composition under consideration. With the SUV surface charge density, we get the total attraction force density and we distribute it proportionally to the SUV surface. To exemplify the calculation, we consider a PAT3 SUV, which has $a_D = 70.37\%$, i.e., about 70% of the surface of the SUV is covered by the L_o phase (red in Fig. 25). For composition PAT3, the concentration of DOTAP in the L_d phase (blue in Fig. 25) is 41.8% (see Table 8), corresponding to 67.15% of the total DOTAP in the SUV. So, we uniformly distribute 67.15% of the total charge density, and hence force, to the L_d phase.

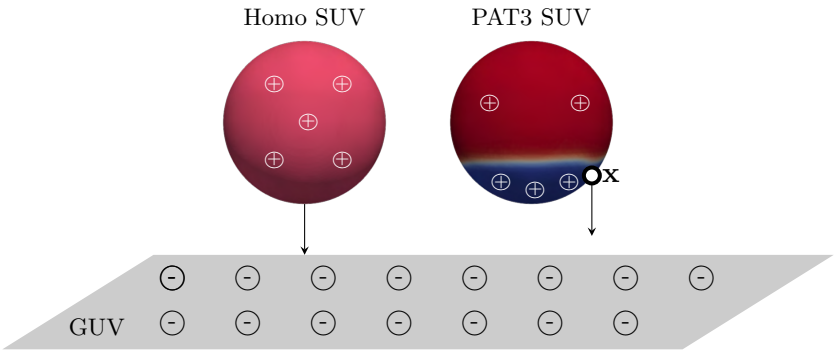

Figure 25: Relative positions of GUV, represented as a plane, and a positively charged SUV, homogeneous (sphere on the left) or phase-separated PAT3 SUV (sphere on the right), in a simulation. The L_o phase in the phase-separated SUV is colored in red, while the L_d phase is blue.

6.3.1 Results and Discussion

In order to investigate the effect of surface density of cationic lipid DOTAP on liposomes' fusogenicity, we selected a phase-separating lipid composition DOPC:DPPC:Chol and focused on three different molar ratios reported in Table 6 with distinct domain (L_o) area fractions a_D. We replaced 15 mol% of DOPC in these liposomal formulations with DOTAP. Given that DOTAP's acyl-chain chemistry is similar to that of DOPC, we assumed that this lipid would have similar phase partitioning behavior as DOPC and would mostly partition into the L_d phase. Table 8 summarizes the lipid distribution among L_o and L_d phases. These lipid distributions are estimated based on the tie-lines available in literature [106] and as described in [111, 117]. With the same DOTAP content, composition PAT3 is expected to have the highest surface density of DOTAP in L_d phase because it has the largest a_D, and composition PAT1 is expected to have the lowest density of DOTAP in its L_d phase because it has the smallest a_D.

Table 8: Lipid distribution among the two phases in the examined phase-separated SUVs

	L_d phase				L_o phase			
Composition	DOTAP	DOPC	DPPC	Chol	DOTAP	DOPC	DPPC	Chol
PAT1 (15%)	16.67%	49.33%	16%	18%	5.56%	16.44%	43%	35%
PAT2 (15%)	22.91%	41.09%	29%	7%	4.65%	8.35%	61%	26%
PAT3 (15%)	41.80%	26.20%	24%	8%	8.61%	5.39%	57%	29%

Here, we present the computational data and show how they corroborate the observations made from the experiments. Details of laboratory experiments can be found in [110]. As mentioned in before, in phase-separated SUVs with cationic lipids there is a complex interplay of the forces driving phase separation, forces driving surface flow, and electrostatic forces. In order to facilitate our understanding of how patches of fusogenic lipids promote fusion, we let the SUVs undergo phase-separation before exposing them to the target model membranes both in the simulations and in the experiments. This serves the purpose of disentangling the effect of phase separation forces from the effect of electrostatic forces. By the time the SUVs are exposed to the model membranes (i.e., $>$ 60 min after formation), most SUVs have reached the equilibrium phase-separated state,

mostly with one patch of the minority phase against the background of the majority phase. From results in the previous section, we know that membranes of different lipid compositions take different times to reach the equilibrium state, specifically it happens faster for compositions with smaller L_o domain area fractions. See Fig. 26 for the average time needed to reach the equilibrium for the three lipid compositions under consideration. The average is taken over five simulations with the given composition and random initial distributions. We see that a PAT3 SUV ($a_D \approx 70\%$) takes more than the double of the time a PAT1 SUV ($a_D \approx 11\%$) needs to reach the equilibrium state. We remark that the time in the simulations correspond to physical time.

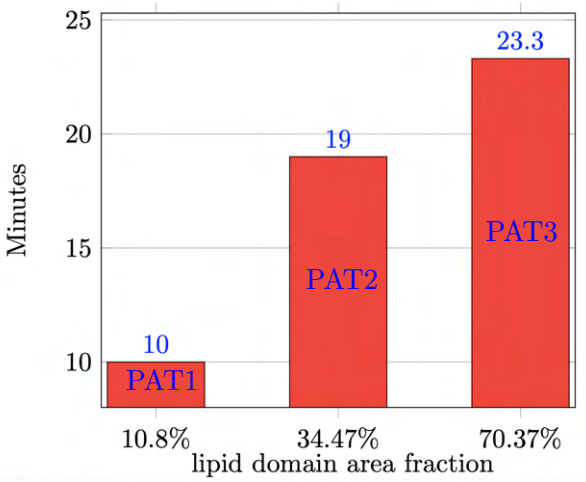

Figure 26: Average time needed for a simulated SUV to reach the equilibrium state (i.e., one patch of the minority phase against the background of the majority phase) for the three compositions under consideration.

Once a SUV has reached the phase-separated equilibrium, it is exposed to the target model membrane (equivalent of GUV in experiments), which is represented as a horizontal plane below the SUV in the simulations. Initially, we place the L_d phase, which is the phase with the majority of the positive charge, opposite to the model membrane, i.e., at the top of the SUV. See the first column in Fig. 27. In a sense, this is the worst-case scenario as it will take the longest to reorient the L_d phase so that it faces the model membrane. Once the L_d phase faces the model membrane, the SUV is in the optimal configuration to initiate fusion since the majority of the fusogenic lipids is in the L_d phase (see Table 8). Fig. 27 shows snapshots of the simulated reorientation process

for the three compositions. From Fig. 27, we clearly see that each SUV takes a different amount of time to have the L_d phase face the model membrane. Fig. 28 reports such (average) time for each composition. The average is computed again over 5 simulations per composition, as explained above. We take this time as a proxy for the promotion of fusion since it is the time need to have the SUV in the optimal configuration for fusion, i.e., with the majority of the fusogenic lipids facing the GUV. Fig. 28 informs us that in average a PAT1 SUV takes ten times longer than a PAT3 SUV to reorient its L_d phase. In contrast, the PAT1 and PAT2 SUVs exposed to a GUV in the worst-case scenario (i.e., L_d phase opposite to the GUV) did not have sufficient time to have the L_d phase face the GUV. This provides an explanation why the PAT3 SUVs outperform both the PAT1 and PAT2 SUVs.

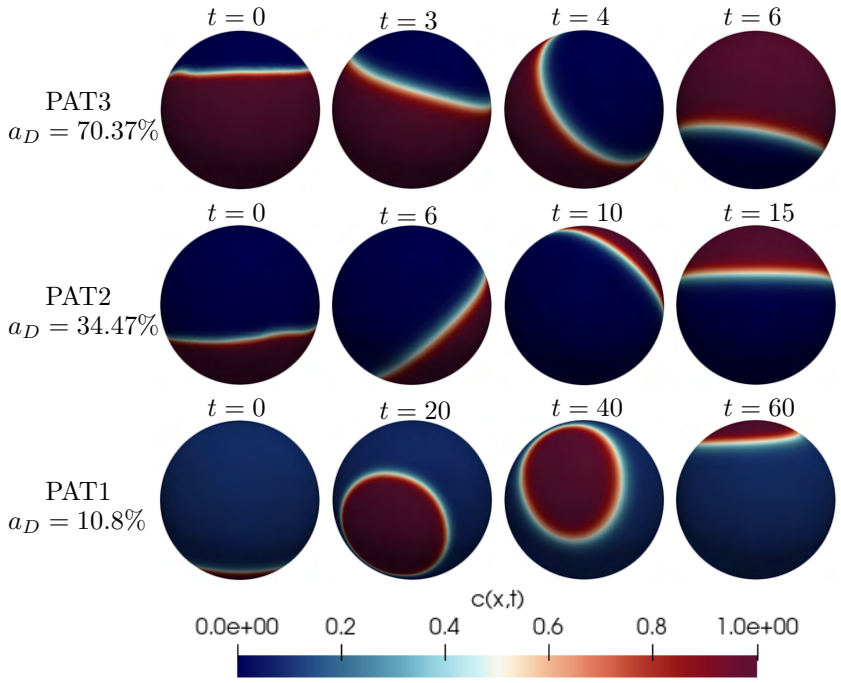

Figure 27: Snapshots of a simulation with the phase-separated PAT3 SUV (top), PAT2 SUV (center), and PAT1 SUV (bottom) at different times (min). Red corresponds to the L_o phase and blue to the L_d phase. For each composition, the L_d phase is initially placed at the top of the SUV (first column). The model membrane, not seen in the figure, is represented as a horizontal plane below the SUV.

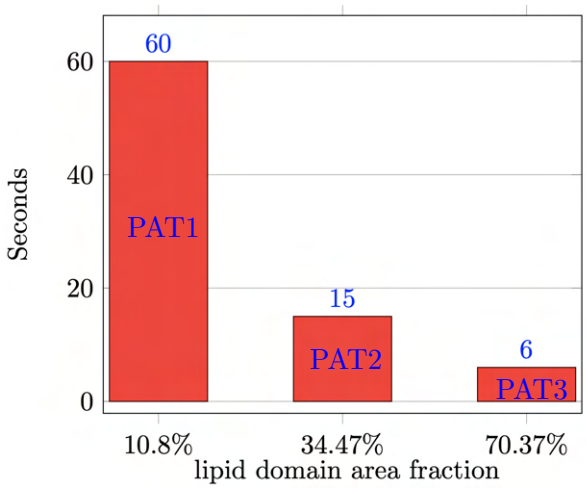

Figure 28: Average time needed to have the L_d phase in a simulated SUV face the target model membrane starting from the worst-case scenario configuration.

7 Conclusion

In this dissertation, we introduced and investigated an SAV formulation of the geometrically unfitted trace finite element method for the surface Cahn–Hilliard equations with degenerate mobility. Additionally, we presented an extension of a well-known phase field model for two-phase incompressible flow, applying and analyzing an unfitted finite element method for its numerical approximation. Subsequently, we applied our Navier–Stokes–Cahn–Hilliard model to investigate (i) the coarsening and fluidity of lipid vesicles and (ii) the fusogenicity of lipid vesicles.

Both the BDF1 and BDF2 versions concerning the SAV method were proven to dissipate specific energy, aligning with the fundamental property of the continuous problem. The method demonstrated optimal convergence rates for smooth solutions and performed well in predicting phase separation and pattern formation in spherical and more complex shapes. Thus, it proved to be a valuable tool in modeling multicomponent lipid vesicles. A comparison with a semi-explicit mixed trace finite element method formulation with stabilization from [115] shows very similar performance of both methods for the given class of problems. Both methods are well-suited for time adaptation. Experiments suggested that the SAV method allows for somewhat larger time steps when the same adaptive criteria are used for the SAV and semi-explicit stabilized methods. The stabilized method requires an additional parameter to be chosen, while the SAV method adds a rank-one dense matrix to the resulting system of algebraic equations, which must be solved at each time step. The availability of a fast algebraic solver for such systems may determine one's preference between these two solid methods.

The advantage of our surface Navier–Stokes–Cahn–Hilliard model is its thermodynamic consistency for a general monotone relation of density and the phase-field variable. To reduce the computational cost, the discrete scheme we proposed decouples the fluid problem (a linearized Navier–Stokes type problem) from the phase-field problem (a Cahn–Hilliard type problem with constant mobility) at each time step. An attractive feature of our scheme is that the numerical

solution satisfies the same stability bound as the solution of the original system under some restrictions on the discretization parameters. We validated our implementation of the proposed numerical scheme with a benchmark problem and applied it to simulate well-known two-phase fluid flows: the Kelvin–Helmholtz and Rayleigh–Taylor instabilities. We investigated the effect of line tension on such instabilities. For the Rayleigh–Taylor instability, we also assessed the effect of viscosity and surface shape, which plays an important role in the evolution of the instability.

Finally, the surface Navier–Stokes–Cahn–Hilliard model incorporating electrostatic forces was employed to investigate the fusogenicity of positively charged lipid vesicles. Experimental observations in the laboratory align with numerical simulations conducted using a mathematical model for phase-separated charged liposomes. The surface Navier–Stokes–Cahn–Hilliard model offers a valuable framework for designing and developing highly fusogenic liposomes with minimal toxicity.

8 Appendix

For the implementation of the methods in this work, the open source Finite Element package DROPS [23] was used. The version of the package to reproduce the results from this work can be found here: `https://github.com/56th/drops`.

In order to reproduce simulations with the Navier-Stokes-Cahn-Hilliard model build the directory `surfnsch`, and for the implementations related to SAV method refer to the directory `savch`. The `readme` page of the repository contains detailed instructions.

Bibliography

[1] Abels, H., and Breit, D. Weak solutions for a non-newtonian diffuse interface model with different densities. *Nonlinearity 29*, 11 (2016), 3426.

[2] Abels, H., Garcke, H., and Grün, G. Thermodynamically consistent, frame indifferent diffuse interface models for incompressible two-phase flows with different densities. *Mathematical Models and Methods in Applied Sciences 22*, 03 (2012), 1150013.

[3] Abels, H., Garcke, H., and Weber, J. Existence of weak solutions for a diffuse interface model for two-phase flow with surfactants. *Communications on Pure & Applied Analysis 18*, 1 (2019), 195–225.

[4] Aki, G. L., Dreyer, W., Giesselmann, J., and Kraus, C. A quasi-incompressible diffuse interface model with phase transition. *Mathematical Models and Methods in Applied Sciences 24*, 05 (2014), 827–861.

[5] Akrivis, G., Li, B., and Li, D. Energy-decaying extrapolated RK–SAV methods for the Allen–Cahn and Cahn–Hilliard equations. *SIAM Journal on Scientific Computing 41*, 6 (2019), A3703–A3727.

[6] Almofti, M. R., Harashima, H., Shinohara, Y., Almofti, A., Baba, Y., and Kiwada, H. Cationic liposome-mediated gene delivery: biophysical study and mechanism of internalization. *Archives of Biochemistry and Biophysics 410*, 2 (2003), 246–253.

[7] Bandekar, A., and Sofou, S. Floret-shaped solid domains on giant fluid lipid vesicles induced by pH. *Langmuir 28* (2012), 4113–4122.

[8] Bandekar, A., Zhu, C., Gomez, A., Menzenski, M. Z., Sempkowski, M., and Sofou, S. Masking and triggered unmasking of targeting ligands on liposomal chemotherapy selectively suppress tumor growth in vivo. *Molecular Pharmaceutics 10*, 1 (2013), 152–160.

[9] Bennett, W. D., and Tieleman, D. P. Computer simulations of lipid membrane domains. *Biochimica et Biophysica Acta (BBA) - Biomembranes 1828*, 8 (2013), 1765–1776.

[10] Bonito, A., Demlow, A., and Licht, M. A divergence-conforming finite element method for the surface stokes equation. *SIAM Journal on Numerical Analysis 58*, 5 (2020), 2764–2798.

[11] Boyer, F. A theoretical and numerical model for the study of incompressible mixture flows. *Computers & Fluids 31*, 1 (2002), 41–68.

[12] Brown, D., and London, E. Structure and function of sphingolipid- and cholesterol-rich membrane rafts. *J. Biol. Chem. 275*, 23 (2000), 17221–17224.

[13] Brown, R. Sphingolipid organization in biomembranes: what physical studies of model membranes reveal. *Journal of Cell Science 111*, 1 (1998), 1–9.

[14] Burman, E., Hansbo, P., and Larson, M. G. A stabilized cut finite element method for partial differential equations on surfaces: the Laplace–Beltrami operator. *Computer Methods in Applied Mechanics and Engineering 285* (2015), 188–207.

[15] Cahn, J. W. On spinodal decomposition. *Acta Metallurgica 9*, 9 (1961), 795 – 801.

[16] Cahn, J. W., and Hilliard, J. E. Free energy of a nonuniform system. i. interfacial free energy. *The Journal of Chemical Physics 28*, 2 (1958), 258–267.

[17] Chen, C., and Yang, X. Fast, provably unconditionally energy stable, and second-order accurate algorithms for the anisotropic Cahn–Hilliard model. *Computer Methods in Applied Mechanics and Engineering 351* (2019), 35–59.

[18] Chen, H., Mao, J., and Shen, J. Optimal error estimates for the scalar auxiliary variable finite-element schemes for gradient flows. *Numerische Mathematik 145*, 1 (2020), 167–196.

[19] Cheng, Q., Shen, J., and Yang, X. Highly efficient and accurate numerical schemes for the epitaxial thin film growth models by using the SAV approach. *Journal of Scientific Computing 78* (2019), 1467–1487.

[20] Chibowski, E., and Szcześ, A. Zeta potential and surface charge of DPPC and DOPC liposomes in the presence of PLC enzyme. *Adsorption 22* (2016), 755–765.

[21] Ding, H., Spelt, P. D., and Shu, C. Diffuse interface model for incompressible two-phase flows with large density ratios. *Journal of Computational Physics 226*, 2 (2007), 2078–2095.

[22] Dong, S., and Shen, J. A time-stepping scheme involving constant coefficient matrices for phase-field simulations of two-phase incompressible flows with large density ratios. *Journal of Computational Physics 231*, 17 (2012), 5788–5804.

[23] DROPS package. `http://www.igpm.rwth-aachen.de/DROPS/`.

[24] Du, Q., Ju, L., and Tian, L. Finite element approximation of the Cahn–Hilliard equation on surfaces. *Computer Methods in Applied Mechanics and Engineering 200*, 29-32 (2011), 2458–2470.

[25] Dziuk, G., and Elliott, C. M. Finite element methods for surface PDEs. *Acta Numerica 22* (2013), 289–396.

[26] Eilks, C., and Elliott, C. Numerical simulation of dealloying by surface dissolution via the evolving surface finite element method. *Journal of Computational Physics 227*, 23 (2008), 9727 – 9741.

[27] Emmerich, H. *The Diffuse Interface Approach in Materials Science: Thermodynamic Concepts and Applications of Phase-Field Models*. Springer Publishing Company, Incorporated, 2011.

[28] Eyre, D. J. Unconditionally gradient stable time marching the Cahn-Hilliard equation. *MRS Online Proceedings Library (OPL) 529* (1998).

[29] Feng, X. Fully discrete finite element approximations of the Navier–Stokes–Cahn-Hilliard diffuse interface model for two-phase fluid flows. *SIAM Journal on Numerical Analysis 44*, 3 (2006), 1049–1072.

[30] Feng, X., and Prohl, A. Error analysis of a mixed finite element method for the Cahn-Hilliard equation. *Numerische Mathematik 99*, 1 (2004), 47–84.

[31] Fidorra, M., Garcia, A., Ipsen, J., Härtel, S., and Bagatolli, L. Lipid domains in giant unilamellar vesicles and their correspondence with equilibrium thermodynamic phases: A quantitative fluorescence microscopy imaging approach. *Biochimica et Biophysica Acta (BBA) - Biomembranes 1788*, 10 (2009), 2142 – 2149. Includes Special Section: Cardiolipin.

[32] Funkhouser, C. M., Solis, F. J., and Thornton, K. Dynamics of coarsening in multi-component lipid vesicles with non-uniform mechanical properties. *The Journal of Chemical Physics 140*, 14 (2014), 144908.

[33] Gómez, H., Calo, V. M., Bazilevs, Y., and Hughes, T. J. Isogeometric analysis of the Cahn–Hilliard phase-field model. *Computer Methods in Applied Mechanics and Engineering 197*, 49-50 (2008), 4333–4352.

[34] Gong, Y., Zhao, J., and Wang, Q. An energy stable algorithm for a quasi-incompressible hydrodynamic phase-field model of viscous fluid mixtures with variable densities and viscosities. *Computer Physics Communications 219* (2017), 20–34.

[35] Gong, Y., Zhao, J., Yang, X., and Wang, Q. Fully discrete second-order linear schemes for hydrodynamic phase field models of binary viscous fluid flows with variable densities. *SIAM Journal on Scientific Computing 40*, 1 (2018), B138–B167.

[36] Grande, J., Lehrenfeld, C., and Reusken, A. Analysis of a high-order trace finite element method for PDEs on level set surfaces. *SIAM Journal on Numerical Analysis 56*, 1 (2018), 228–255.

[37] Grigorieff, R. D. Stability of multistep-methods on variable grids. *Numerische Mathematik 42* (1983), 359–377.

[38] Gross, S., and Reusken, A. *Numerical Methods for Two-phase Incompressible Flows*. Springer, Berlin, 2011.

[39] Guillén-González, F., and Tierra, G. Energy-stable and boundedness preserving numerical schemes for the cahn-hilliard equation with degenerate mobility. *Applied Numerical Mathematics 196* (2024), 62–82.

[40] Guo, Z., Lin, P., Lowengrub, J., and Wise, S. Mass conservative and energy stable finite difference methods for the quasi-incompressible Navier–Stokes–Cahn–Hilliard system: Primitive variable and projection-type schemes. *Computer Methods in Applied Mechanics and Engineering 326* (2017), 144–174.

[41] Gurtin, M. E., and Murdoch, A. I. A continuum theory of elastic material surfaces. *Archive for Rational Mechanics and Analysis 57*, 4 (1975), 291–323.

[42] H.-J. Butt, K. Graf, M. K. *The Electric Double Layer*. John Wiley & Sons, Ltd, 2003, ch. 4, pp. 42–56.

[43] Han, D., Brylev, A., Yang, X., and Tan, Z. Numerical analysis of second order, fully discrete energy stable schemes for phase field models of two-phase incompressible flows. *Journal of Scientific Computing 70*, 3 (2017), 965–989.

[44] Heberle, F. A., and Feigenson, G. W. Phase separation in lipid membranes. *Cold Spring Harbor Perspectives in Biology 3*, 4 (2011), a004630.

[45] Heftberger, P., Kollmitzer, B., Rieder, A., Amenitsch, H., and Pabst, G. In situ determination of structure and fluctuations of coexisting fluid membrane domains. *Biophys. J. 108*, 4 (2015), 854–862.

[46] Hoffmann, M., Hersch, N., Gerlach, S., Dreissen, G., Springer, R., Merkel, R., Csiszár, A., and Hoffmann, B. Complex size and surface charge determine nucleic acid transfer by fusogenic liposomes. *International Journal of Molecular Sciences 21*, 6 (2020), 2244.

[47] Hohenberg, P. C., and Halperin, B. I. Theory of dynamic critical phenomena. *Rev. Mod. Phys. 49* (Jul 1977), 435–479.

[48] Huang, F., Shen, J., and Yang, Z. A highly efficient and accurate new scalar auxiliary variable approach for gradient flows. *SIAM Journal on Scientific Computing 42*, 4 (2020), A2514–A2536.

[49] Huang, Q.-A., Jiang, W., Yang, J. Z., and Yuan, C. Upwind-SAV approach for constructing bound-preserving and energy-stable schemes of the Cahn-Hilliard equation with degenerate mobility. *arXiv preprint arXiv:2210.16017* (2022).

[50] Hui, S. W., Langner, M., Zhao, Y.-L., Ross, P., Hurley, E., and Chan, K. The role of helper lipids in cationic liposome-mediated gene transfer. *Biophysical Journal 71*, 2 (1996), 590–599.

[51] Jankuhn, T., Olshanskii, M. A., and Reusken, A. Incompressible fluid problems on embedded surfaces: Modeling and variational formulations. *Interfaces and Free Boundaries 20*, 3 (2018), 353–377.

[52] Jankuhn, T., Olshanskii, M. A., Reusken, A., and Zhiliakov, A. Error analysis of higher order trace finite element methods for the surface Stokes equation. *Journal of Numerical Mathematics 29*, 3 (2021), 245–267.

[53] Juhasz, J., Davis, J. H., and Sharom, F. J. Fluorescent probe partitioning in giant unilamellar vesicles of 'lipid raft' mixtures. *The Biochemical Journal 430*, 3 (September 2010), 415—423.

[54] Kahya, N., Scherfeld, D., Bacia, K., Poolman, B., and Schwille, P. Probing lipid mobility of raft-exhibiting model membranes by fluorescence correlation spectroscopy. *J. Biol. Chem. 278*, 30 (2003), 28109–15.

[55] Karve, S., Bandekar, A., Ali, M. R., and Sofou, S. The pH-dependent association with cancer cells of tunable functionalized lipid vesicles with encapsulated doxorubicin for high cell-kill selectivity. *Biomaterials 31*, 15 (2010), 4409 – 4416.

[56] Kay, D., Styles, V., and Welford, R. Finite element approximation of a Cahn–Hilliard–Navier–Stokes system. *Interfaces and Free Boundaries 10*, 1 (2008), 15–43.

[57] Kolašinac, R., Jaksch, S., Dreissen, G., Braeutigam, A., Merkel, R., and Csiszár, A. Influence of environmental conditions on the fusion of cationic liposomes with living mammalian cells. *Nanomaterials 9*, 7 (2019), 1025.

[58] Kollmitzer, B., Heftberger, P., Rappolt, M., and Pabst, G. Monolayer spontaneous curvature of raft-forming membrane lipids. *Soft Matter 9* (2013), 10877–10884.

[59] Kuzmin, P. I., Akimov, S. A., Chizmadzhev, Y. A., Zimmerberg, J., and Cohen, F. S. Line tension and interaction energies of membrane rafts calculated from lipid splay and tilt. *Biophysical Journal 88*, 2 (2005), 1120–1133.

[60] Landau, L., and Lifshitz, E. *Statistical Physics*. Pergamon Press, Oxford, 1958.

[61] Lederer, P. L., Lehrenfeld, C., and Schöberl, J. Divergence-free tangential finite element methods for incompressible flows on surfaces. *International Journal for Numerical Methods in Engineering 121*, 11 (2020), 2503–2533.

[62] Levental, I., Levental, K., and Heberle, F. Lipid rafts: Controversies resolved, mysteries remain. *Trends Cell Biol. 30*, 5 (2020), 341–353.

[63] Li, S., Lowengrub, J., and Voigt, A. Locomotion, wrinkling, and budding of a multi-component vesicle in viscous fluids. *Communications in Mathematical Sciences 10* (2012), 645–670.

[64] Li, X., Shen, J., and Rui, H. Stability and error analysis of a second-order SAV scheme with block-centered finite differences for gradient flows. *Math. Comp. 88* (2019), 2047–2068.

[65] Liao, H.-l., Ji, B., Wang, L., and Zhang, Z. Mesh-robustness of an energy stable BDF2 scheme with variable steps for the Cahn–Hilliard model. *Journal of Scientific Computing 92*, 2 (2022), 52.

[66] Liao, H.-l., Ji, B., and Zhang, L. An adaptive BDF2 implicit time-stepping method for the phase field crystal model. *IMA Journal of Numerical Analysis 42*, 1 (2022), 649–679.

[67] Liao, H.-L., Song, X., Tang, T., and Zhou, T. Analysis of the second-order BDF scheme with variable steps for the molecular beam epitaxial model without slope selection. *Science China Mathematics 64* (2021), 887–902.

[68] Liao, H.-l., and Zhang, Z. Analysis of adaptive BDF2 scheme for diffusion equations. *Mathematics of Computation 90*, 329 (2021), 1207–1226.

[69] Lingwood, D., and Simons, K. Lipid rafts as a membrane-organizing principle. *Science 327*, 5961 (2010), 46–50.

[70] Lisini, S., Matthes, D., and Savaré, G. Cahn–Hilliard and thin film equations with nonlinear mobility as gradient flows in weighted-Wasserstein metrics. *Journal of Differential Equations 253*, 2 (2012), 814–850.

[71] Liu, C., Frank, F., Thiele, C., Alpak, F. O., Berg, S., Chapman, W., and Riviere, B. An efficient numerical algorithm for solving viscosity contrast Cahn-–Hilliard—Navier-–Stokes system in porous media. *Journal of Computational Physics 400* (2020), 108948.

[72] Liu, C., Zhang, L., Zhu, W., Guo, R., Sun, H., Chen, X., and Deng, N. Barriers and strategies of cationic liposomes for cancer gene therapy. *Molecular Therapy-Methods & Clinical Development 18* (2020), 751–764.

[73] Lowengrub, J., and Truskinovsky, L. Quasi–incompressible Cahn–Hilliard fluids and topological transitions. *Proceedings of the Royal Society of London A: Mathematical, Physical and Engineering Sciences 454*, 1978 (1998), 2617–2654.

[74] Lowengrub, J. S., Rätz, A., and Voigt, A. Phase-field modeling of the dynamics of multicomponent vesicles: Spinodal decomposition, coarsening, budding, and fission. *Physical Review E 79*, 3 (2009), 031926.

[75] Lv, H., Zhang, S., Wang, B., Cui, S., and Yan, J. Toxicity of cationic lipids and cationic polymers in gene delivery. *Journal of Controlled Release 114*, 1 (2006), 100–109.

[76] Nitschke, I., Voigt, A., and Wensch, J. A finite element approach to incompressible two-phase flow on manifolds. *Journal of Fluid Mechanics 708* (2012), 418–438.

[77] Nochetto, R. H., Salgado, A. J., and Tomas, I. A diffuse interface model for two-phase ferrofluid flows. *Computer Methods in Applied Mechanics and Engineering 309* (2016), 497–531.

[78] Olshanskii, M., Palzhanov, Y., and Quaini, A. A scalar auxiliary variable unfitted fem for the surface cahn–hilliard equation. *Journal of Scientific Computing 97*, 3 (2023).

[79] Olshanskii, M., Quaini, A., Reusken, A., and Yushutin, V. A finite element method for the surface stokes problem. *SIAM Journal on Scientific Computing 40*, 4 (2018), A2492–A2518.

[80] Olshanskii, M., Reusken, A., and Schwering, P. An eulerian finite element method for tangential Navier-Stokes equations on evolving surfaces. *Mathematics of Computation* (2023).

[81] Olshanskii, M., Reusken, A., and Zhiliakov, A. Inf-sup stability of the trace P2-P1 Taylor–Hood elements for surface PDEs. *Mathematics of Computation 90*, 330 (2021), 1527–1555.

[82] Olshanskii, M. A. A low order Galerkin finite element method for the Navier–Stokes equations of steady incompressible flow: a stabilization issue and iterative methods. *Computer Methods in Applied Mechanics and Engineering 191*, 47-48 (2002), 5515–5536.

[83] Olshanskii, M. A., and Reusken, A. Trace finite element methods for pdes on surfaces. In *Geometrically Unfitted Finite Element Methods and Applications: Proceedings of the UCL Workshop 2016* (2017), Springer, pp. 211–258.

[84] Olshanskii, M. A., Reusken, A., and Grande, J. A finite element method for elliptic equations on surfaces. *SIAM Journal on Numerical Analysis 47* (2009), 3339–3358.

[85] Olshanskii, M. A., Reusken, A., and Zhiliakov, A. Tangential Navier–Stokes equations on evolving surfaces: Analysis and simulations. *Mathematical Models and Methods in Applied Sciences 32*, 14 (2022), 2817–2852.

[86] Olshanskii, M. A., and Yushutin, V. A penalty finite element method for a fluid system posed on embedded surface. *Journal of Mathematical Fluid Mechanics 21*, 1 (Feb 2019), 14.

[87] Olshanskii, M. A., and Zhiliakov, A. Recycling augmented lagrangian preconditioner in an incompressible fluid solver. *Numerical Linear Algebra with Applications 29*, 2 (2022), e2415.

[88] Palzhanov, Y., Zhiliakov, A., Quaini, A., and Olshanskii, M. A decoupled, stable, and linear fem for a phase-field model of variable density two-phase incompressible surface flow. *Computer Methods in Applied Mechanics and Engineering 387* (2021), 114167.

[89] Reusken, A. Analysis of trace finite element methods for surface partial differential equations. *IMA Journal of Numerical Analysis 35*, 4 (2015), 1568–1590.

[90] Sakuma, Y., Kawakatsu, T., Taniguchi, T., and Imai, M. Viscosity landscape of phase-separated lipid membrane estimated from fluid velocity field. *Biophysical Journal 118*, 7 (2020), 1576–1587.

[91] Sempkowski, M., Zhu, C., Menzenski, M. Z., Kevrekidis, I. G., Bruchertseifer, F., Morgenstern, A., and Sofou, S. Sticky patches on lipid nanoparticles enable the selective targeting and killing of untargetable cancer cells. *Langmuir 32*, 33 (2016), 8329–8338.

[92] Semrau, S., and Schmidt, T. Membrane heterogeneity – from lipid domains to curvature effects. *Soft Matter 5* (2009), 3174–3186.

[93] Sezgin, E., Levental, I., Grzybek, M., Schwarzmann, G., Mueller, V., Honigmann, A., Belov, V. N., Eggeling, C., Ünal Coskun, Simons, K., and Schwille, P. Partitioning, diffusion, and ligand binding of raft lipid analogs in model and cellular plasma membranes. *Biochimica et Biophysica Acta (BBA) - Biomembranes 1818*, 7 (2012), 1777 – 1784.

[94] Shen, J., and Xu, J. Convergence and error analysis for the scalar auxiliary variable (SAV) schemes to gradient flows. *SIAM Journal on Numerical Analysis 56*, 5 (2018), 2895–2912.

[95] Shen, J., Xu, J., and Yang, J. The scalar auxiliary variable (SAV) approach for gradient flows. *Journal of Computational Physics 353* (2018), 407–416.

[96] Shen, J., Xu, J., and Yang, J. A new class of efficient and robust energy stable schemes for gradient flows. *SIAM Review 61*, 3 (2019), 474–506.

[97] Shen, J., and Yang, X. Numerical approximations of Allen-Cahn and Cahn-Hilliard equations. *Discrete & Continuous Dynamical Systems - A 28* (2010), 1669.

[98] Shokrpour Roudbari, M., Şimşek, G., van Brummelen, E. H., and van der Zee, K. G. Diffuse-interface two-phase flow models with different densities: A new quasi-incompressible form and a linear energy-stable method. *Mathematical Models and Methods in Applied Sciences 28*, 04 (2018), 733–770.

[99] Simberg, D., Weisman, S., Talmon, Y., and Barenholz, Y. Dotap (and other cationic lipids): chemistry, biophysics, and transfection. *Critical Reviews™ in Therapeutic Drug Carrier Systems 21*, 4 (2004).

[100] Sohn, J. S., Tseng, Y.-H., Li, S., Voigt, A., and Lowengrub, J. S. Dynamics of multicomponent vesicles in a viscous fluid. *Journal of Computational Physics 229*, 1 (2010), 119–144.

[101] Stanich, C. A., Honerkamp-Smith, A. R., Putzel, G. G., Warth, C. S., Lamprecht, A. K., Mandal, P., Mann, E., Hua, T.-A. D., and Keller, S. L. Coarsening dynamics of domains in lipid membranes. *Biophysical Journal 105*, 2 (2013), 444–454.

[102] Sun, M., Feng, X., and Wang, K. Numerical simulation of binary fluid–surfactant phase field model coupled with geometric curvature on the curved surface. *Computer Methods in Applied Mechanics and Engineering 367* (2020), 113123.

[103] Sun, M., Xiao, X., Feng, X., and Wang, K. Modeling and numerical simulation of surfactant systems with incompressible fluid flows on surfaces. *Computer Methods in Applied Mechanics and Engineering 390* (2022), 114450.

[104] Trementozzi, A. N., Imam, Z. I., Mendicino, M., Hayden, C. C., and Stachowiak, J. C. Liposome-mediated chemotherapeutic delivery is synergistically enhanced by ternary lipid compositions and cationic lipids. *Langmuir 35*, 38 (2019), 12532–12542.

[105] Veatch, S. L., and Keller, S. L. Separation of liquid phases in giant vesicles of ternary mixtures of phospholipids and cholesterol. *Biophysical Journal 85*, 5 (2003), 3074–3083.

[106] Veatch, S. L., Soubias, O., Keller, S. L., and Gawrisch, K. Critical fluctuations in domain-forming lipid mixtures. *Proceedings of the National Academy of Sciences 104*, 45 (2007), 17650–17655.

[107] Š. Bálint, and Dustin, M. Localizing order to boost signaling. *eLife 6* (2017), e25375.

[108] Wang, M., Huang, Q., and Wang, C. A second order accurate scalar auxiliary variable (SAV) numerical method for the square phase field crystal equation. *Journal of Scientific Computing 88*, 2 (2021), 33.

[109] Wang, X., and Du, Q. Modelling and simulations of multi-component lipid membranes and open membranes via diffuse interface approaches. *Journal of Mathematical Biology 56*, 3 (Mar 2008), 347–371.

[110] Wang, Y., Palzhanov, Y., Dang, D. T., Quaini, A., Olshanskii, M., and Majd, S. On fusogenicity of positively charged phased-separated lipid vesicles: experiments and computational simulations. *Biomolecules 13*, 10 (2023), 1473.

[111] Wang, Y., Palzhanov, Y., Quaini, A., Olshanskii, M., and Majd, S. Lipid domain coarsening and fluidity in multicomponent lipid vesicles: A continuum based model and its experimental validation. *Biochimica et Biophysica Acta (BBA) - Biomembranes 1864*, 7 (2022), 183898.

[112] Wesolowska, O., Michalak, K., Maniewska, J., and Hendrich, A. B. Giant unilamellar vesicles - a perfect tool to visualize phase separation and lipid rafts in model systems. *Acta Biochimica Polonica 56* (2009), 33–39.

[113] Yang, J., and Kim, J. A phase-field model and its efficient numerical method for two-phase flows on arbitrarily curved surfaces in 3d space. *Computer Methods in Applied Mechanics and Engineering 372* (2020), 113382.

[114] Yang, J., Mao, S., He, X., Yang, X., and He, Y. A diffuse interface model and semi-implicit energy stable finite element method for two-phase magnetohydrodynamic flows. *Computer Methods in Applied Mechanics and Engineering 356* (2019), 435–464.

[115] Yushutin, V., Quaini, A., Majd, S., and Olshanskii, M. A computational study of lateral phase separation in biological membranes. *International Journal for Numerical Methods in Biomedical Engineering 35*, 3 (2019), e3181.

[116] Yushutin, V., Quaini, A., and Olshanskii, M. Numerical modeling of phase separation on dynamic surfaces. *Journal of Computational Physics 407* (2020), 109126.

[117] Zhiliakov, A., Wang, Y., Quaini, A., Olshanskii, M., and Majd, S. Experimental validation of a phase-field model to predict coarsening dynamics of lipid domains in multicomponent membranes. *Biochimica et Biophysica Acta (BBA)-Biomembranes 1863*, 1 (2021), 183446.

[118] Zhu, G., Chen, H., Li, A., Sun, S., and Yao, J. Fully discrete energy stable scheme for a phase-field moving contact line model with variable densities and viscosities. *Applied Mathematical Modelling 83* (2020), 614–639.

[119] Zhu, J., Chen, L.-Q., Shen, J., and Tikare, V. Coarsening kinetics from a variable-mobility Cahn-Hilliard equation: Application of a semi-implicit Fourier spectral method. *Phys. Rev. E 60* (Oct 1999), 3564–3572.

[120] Zhuang, Q., and Shen, J. Efficient SAV approach for imaginary time gradient flows with applications to one-and multi-component Bose–Einstein condensates. *Journal of Computational Physics 396* (2019), 72–88.